Freie Universität Berlin

Numerical methods based on direct discretizations for uni- and bi-variate population balance systems

Dissertation zur Erlangung des Grades
einer Doktorin der Naturwissenschaften (Dr. rer. nat.)
am Fachbereich Mathematik und Informatik
der Freien Universität Berlin

von

Oana Carina Suciu

Berlin
Mai 2013

Gutachter

Prof. Volker John
Free University of Berlin and Weierstrass Institute
for Applied Analysis and Stochastics

Prof. Endre Suli
University of Oxford
Date of defense: 28.09.2013

To my father

Mathematicians do not study objects, but relations between objects. Thus, they are free to replace some objects by others so long as the relations remain unchanged. Content to them is irrelevant: they are interested in form only.

Henri Poincaré

Abstract.

Population balance systems model the interaction of the surrounding medium and the particles which are described by the particle size distribution (PSD). This way of modeling results in a system of partial differential equations where the incompressible Navier–Stokes equations for the fluid velocity and pressure are coupled to convection-diffusion equations for species concentration and the system temperature, and a transport equation for the PSD. The equation for the PSD may even contain an integral operator that models, e.g., the aggregation of the particles. Whereas the flow field, the concentration of dissolved species, and temperature are defined in a three-dimensional spatial domain, the PSD depends also on the internal *coordinates, which are used to describe additional properties of the particles (e.g.,* diameter, volume*). In particular,* **uni-variate** *and* **bi-variate** *population balance models are based on one- and two-dimensional geometrical characterizations of the individual particles (*diameter, volume, or main axis in the case of anisotropic particles*), resulting in four-dimensional (4D) and five-dimensional (5D) population balance systems. There are several classes of numerical methods for solving population balance systems. With the ongoing rise of computer power, the option of using direct discretizations for simulating those systems becomes more and more interesting since these discretizations do not introduce an additional error by circumventing the solution of the higher-dimensional equation for PSD, like momentum-based methods or operator-splitting schemes. In this thesis, it is shown for uni-variate population balance systems that for an appropriate choice of the unknown model parameters in aggregation kernel good agreements can be achieved between the experimental data and the numerical results computed by the numerical methods. A mixed finite difference/finite volume method is used for discretizing the PSD equation in the case of bi-variate population balance systems. In this case, it is demonstrated that even in the class of direct discrerizations, different numerical methods lead to qualitatively different numerical solutions.*

Zusammenfassung.

Populationsbilanzsysteme modellieren die Wechselwirkung zwischen Teilchen, welche durch ihre Partikelgrößenverteilung beschrieben sind, und ihrem umgebenden Medium. Aus mathematischer Sicht führt das auf ein gekoppeltes System von partiellen Differentialgleichungen. Die inkompressible Navier–Stokes–Gleichungen, welche die Fluidgeschwindigkeit und den Druck beschreiben, sind hier an Konvektions–Diffusions–Gleichungen, welche die Konzentration der Spezies sowie die Temperatur des Systems modellieren und an eine Transportgleichung für die Beschreibung der Partikelgrößenverteilung gekoppelt. Die Gleichung für die Partikelgrößenverteilung kann sogar einen Integraloperator enthalten, der zum Bespiel die Aggregation von Partikeln modelliert. Das Strömungsfeld, die Konzentration der gelösten Spezies und die Temperatur des Systems sind in einem dreidimensionalen Gebiet definiert. Die Partikelgrößenverteilung hängt darüber hinaus von den internen *Koordinaten ab, welche zusätzliche Eigenschaften der Partikel (z. B.* Durchmesser, Volumen*) beschreiben. Insbesondere sind* **univariate** *und* **bivariate** *Populationsbilanzmodelle dadurch gekennzeichet, dass sie eine ein- oder zweidimensionale geometrische Charakterisierung der einzelne Partikel darstellen (*Durchmesser, Volumen der Teilchen oder Hauptachse von anisotropen Teilchen*). Dies resultiert in vierdimensionale (4D) und fünfdimensionale (5D) Populationsbilanzsysteme. Zur numerischen Lösung von solchen Systemen können verschiedene Klassen von Methoden genutzt werden. Mit dem Anstieg der Rechenleistung werden direkte Diskretisierungen für die Simulation zunehmend interessanter. Solche direkten Schemata haben gegenüber Momentenmethoden oder Operator-Splitting-Methoden den Vorteil, dass kein zusätzlicher Fehler durch die Dimensionsreduktion entsteht. Für univariate Populationsbilanzsysteme wird in der Arbeit gezeigt, dass unter Benutzung von geeigneten Modellparametern für den Aggregationskern gute Übereinstimmungen zwischen den numerischen Resultaten und den experimentellen Messungen erzielt werden können. Für die Diskretisierung der Partikelgrößenverteilung für bivariate Populationsbilanzsysteme wird ein gemischtes Finite–Differenzen/Finite–Volumen–Verfahren benutzt. In diesem Fall wird gezeigt, dass sogar direkte Diskretisierungsmethoden zu qualitativ unterschiedlichen Lösungen führen können.*

Acknowledgment.

First of all, I would like to express my deep gratitude to Prof. Dr. Volker John, my research supervisor, for his patient guidance, enthusiastic encouragement, remarkable suggestions, and useful critiques throughout my PhD project.

I also deeply appreciate the help of all my colleagues from the research group Numerical Mathematics and Scientific Computing of Weierstrass Institute for Applied Analysis and Stochastic. Special thanks should be given to Alfonso Caiazzo, André Fiebach, Hartmut Langmach, and Ellen Schmeyer for their valuable and constructive advices during the planning and development of this research work. My grateful thanks are also extended to Gabi Blätermann and to the research group secretary Marion Lawrenz for their enormous support and kindness.

Furthermore, I would like to thank also Prof. Dr. Sundmacher and his working group for the good collaboration as well as for many valuable discussions concerning the field of process engineering. Special thanks should be given to the former PhD student Cristian Borchert.

Also, I would like to thank the Bundesministerium für Bildung und Forschung (BMBF) for the financial support.

Of course, I am overwhelmingly grateful to all my friends for their optimistic encouragements. Especially, I would like to express my deepest gratitude to my extraordinary friends, Claudiu Serban, Claudia Bivolaru, Carmen Iovan, Ligia Iovan, Monika Honsel, Oliver Schirra, and Dirk Voltz for being a consistent mental support during this period. I would like to thank also my friend, Jocelyn Polen, for her immediate help in checking the language of some parts of this thesis.

Finally, I would like to express my deep obligation to my parents, Ionelia Muja and Constantin Suciu, my sister, Denisa Walder, for their love and encouragements over the years and to my nephew, Kevin Walder, for his ever shining smile of kindness and love.

Berlin, May 2013
Oana Carina Suciu.

Contents

List of Figures

List of Tables

Nomenclature

Abbreviations

BWE	*backward Euler method*
BWE–UPW–FDM	*backward Euler upwind finite difference method*
CMS	*control mass system*
CVS	*control volume system*
d.o.f.	*degrees of freedom*
ENO	*essentially non-oscillatory*
	essentially non-oscillatory finite difference method
FDM	*finite difference method*
FEM–FCT	*finite element flux-corrected transport*
FEM	*finite element method*
FFT	*fast Fourier transform*
FVM	*finite volume method*
FWE	*forward Euler method*
FWE–UPW–FDM	*forward Euler upwind finite difference method*
GMRES	*generalized minimal residual*
KDP	*potassium dihydrogen phosphate*
l.h.s	*left hand side*
PBS	*population balance systems*
Pe	*Peclet number*
PSD	*particle size distribution*
Re	*Reynolds number*
r.h.s.	*right hand side*
RK–ENO–FDM	*total variation diminishing explicit Runge–Kutta*
TVD	*total variation diminishing*

Latin letters

b_1	*kinetic order of nucleation due to bi-variate model*
b_2	*kinetic order of nucleation due to bi-variate model*
b	*kinetic order of nucleation due to uni-variate model*
B_{nuc}	*nucleation rate*
c	*concentration*
c_∞	*reference concentration*
C_{br}	*unknown model parameter due to aggregation kernel*
c_{sat}	*equilibrium saturation concentration*
C_{sh}	*unknown model parameter due to aggregation kernel*
c_p	*specific heat capacity*
CV	*volume*
D	*diffusion coefficient*
F	*force*
f_∞	*reference particle size distribution*
$f_{L,\mathrm{seed}}$	*see page 65*
f_{inj}	*see page 65*
f_{in}	*see page 65*
f	*particle size distribution*
G_1	*growth rate due to bi-variate model*
G_2	*growth rate due to bi-variate model*
G	*growth rate (uni-variate model)*
g	*kinetic order of growth due to uni-variate model*
H_{agg}	*term accounting for aggregation*
H_{nuc}	*term accounting for nucleation*
H	*source and sink for transport equation*
κ_{agg}	*aggregation kernel*
k_b	*kinematic parameter for nucleation due to uni-variate model and bi-variate model*
k_{g1}	*kinematic parameter for growth due to bi-variate model*
k_{g2}	*kinematic parameter for growth due to bi-variate model*
k_g	*kinematic parameter for growth due to uni-variate model*
k_V	*form factor due to the particle shape*

L_1	*equivalent width (depth) for anisotropic particle*
$L_{1,\infty}$	*reference width (depth) for anisotropic particle*
$L_{1,\max}$	*upper bound for the particle width (depth)*
$L_{1,\min}$	*lower bound for the particle width (depth)*
L_2	*equivalent length for anisotropic particle*
$L_{2,\infty}$	*reference length for anisotropic particle*
$L_{2,\max}$	*upper bound for the particle length*
$L_{2,\min}$	*lower bound for the particle length*
L	*equivalent diameter for spherical particle*
L_∞	*reference diameter for spherical particle*
l_∞	*reference length*
$L_{\max}$	*upper bound for the particle diameter*
$L_{\min}$	*lower bound for the particle diameter*
$\mathbf{g}$	*body force (gravity, centrifugal and Coriolis)*
$\mathbf{u}_\infty$	*reference velocity*
$\mathbf{u}$	*velocity*
$\mathcal{F}$	*source and sink for the convection-diffusion equations*
$\mathcal{J}_c$	*flux with respect to the quantity c*
$\mathcal{J}_f$	*flux with respect to the quantity f*
$\mathcal{J}$	*flux*
$\mathcal{S}$	*see page 50*
m	*mass*
m_{mol}	*molar mass*
N_p	*degrees of freedom for pressure*
N	*total number of particles*
N_u	*degrees of freedom for velocity*
P_1^{disc}	*see 19*
p_∞	*reference pressure*
p_{col}	*see page 40*
p_{eff}	*see page 40*
p	*pressure*
Q_2	*see page 19*
q_3	*volume fraction*
s	*surface*

t_{end}	*final time*
T_∞	*reference temperature*
t_∞	*reference time*
t_{inj}	*see page 65*
T_{in}	*see page 61*
T_{wall}	*see 61*
T	*temperature*
t	*time*
U_{in}	*see page 57*
V_{inj}	*see page 65*
$V_{\max}$	*upper bound for particle volume*
$V_{\min}$	*lower bound for particle volume*
V_{total}	*total volume of dispersed phase*
V_r	*flow rate*

Greek letters

δ	*the Dirac delta distribution*
Δh_{cryst}	*heat of the solution (enthalpy change of the solution)*
η	*see page 57*
Γ	*boundary*
Γ_{in}	*boundary see page 57*
Γ_{out}	*boundary see page 57*
Γ_{wall}	*boundary see page 57*
λ	*thermal conductivity*
μ	*dynamic viscosity*
ν	*kinematic viscosity*
Ω	*flow domain*
ω_{comp}	*see page 50*
ω_{exact}	*see page 50*
ψ	*basis function of finite element spaces or see page 50*
Ψ	*see page 57*
ρ^d	*crystal (dispersed phase) density*
ρ	*fluid (continuous phase) density*
σ_{gr}	*interphase mass (energy) exchange due to the growth*
σ_{rel}	*relative supersaturation*
θ	*see page 24*
φ	*basis function of finite element spaces or see page 50*
ς	*viscosity constant*
ξ	*see page 57*

Matrix

$\mathbf{A}$	*see page 17*
$\mathbf{B}$	*see page 17*
$\mathbf{B}^T$	*see page 17*
$\mathbf{B}^T$	*see page 17*
$\mathbf{D}$	*see page 27*
$\mathbf{E}$	*see page 27*
$\mathbf{L}$	*see page 27*
$\mathbf{M}_C$	*see page 27*
$\mathbf{M}_L$	*see page 27*

Operators

Δ	*Laplace operator*
$\nabla\cdot$	*divergenceh*
∇	*Nabla operator or gradient*
∂	*partial derivation*

Specification

$(\cdot)_D$	*notification with respect to Dirichlet boundary*
$(\cdot)_{H^1}$	*notification with respect Sobolev spaces of order 1*
$(\cdot)_{H^m}$	*notification with respect Sobolev spaces of order m*
$(\cdot)^h$	*quantity in the discrete space*
$(\cdot)_k$	*quantity at the discrete time*
$(\cdot)_{L^2}$	*notification with respect Lebesque spaces*
$(\cdot)_L$	*notification with respect to internal coordinates*
$(\cdot)_{\mathbf{x}}$	*notification with respect to external coordinates*
$(\cdot)_{\text{agg}}$	*notification with respect to aggregation*
$(\cdot)_{cryst}$	*notification with respect to crystalline phase*
$(\cdot)_{\text{gr}}$	*notification with respect to growth*
$(\cdot)_{\text{inj}}$	*notification with respect to injection*
$(\cdot)_{\text{nuc}}$	*notification with respect to nucleation*
$(\cdot)_N$	*notification with respect to Neumann boundary*
$(\cdot)_o$	*notification with respect to do-nothing boundary*
$(\cdot)_t$	*time derivative*
$(\cdot)_V$	*notification with respect the particle volume*
$(\tilde{\cdot})$	*quantity with dimension*

Vectors

$\mathbf{f}$	*force acting on control volume*
$\mathbf{m}$	*impulse*
$\mathbf{n}$	*unit normal*
$\mathbf{r}$	*residual*
$\mathbf{u}$	*fluid velocity*
$\mathbf{u}_L$	*convective field with respect to internal coordinates*
$\mathbf{u}_\mathbf{x}$	*convective field with respect to external coordinates*
$\mathbf{x}$	*point in continuous space*

Tensors

$\mathbb{D}$	*deformation tensor*
$\mathbb{I}$	*unit tensor*
σ	*stress tensor*
τ	*strain tensor*

Domains and boundaries

CV	*volume (control volume)*
Γ	*boundary of* Ω
Γ_D	*Dirichlet boundary*
Γ_{in}	*inlet boundary*
Γ_{out}	*outlet boundary*
Γ_{wall}	*boundary at the walls*
Γ_N	*Neumann boundary*
Ω	*domain*
Ω_L	*space domain with respect to internal coordinates*
$\Omega_\mathbf{x}$	*space domain with respect to external coordinates*
∂CV	*boundary of* CV
V_L	*particle control volume with respect to internal coordinates*
$V_\mathbf{x}$	*particle control volume with respect to external coordinates*
V	*particle volume*
V'	*particle volume*

Function spaces

$H^1(\Omega)$	*Sobolev spaces*
$H^m(\Omega)$	*Sobolev spaces of order* m
$L^2(\Omega)$	*Lebesque spaces*
Q^h	*see page 17*
Q	*see page 16*
V_0^h	*see page 17*
V_0	*see page 16*
V_D^h	*see page 17*
V_D	*see page 16*

Mathematical notation

$(\cdot\,,\cdot\,)$	*inner product*
$\|\cdot\|$	*norm*
Δ	*infinitesimal size*
$d\mathbf{x}$	*volume element*
ds	*surface element*
dV	*particle volume element*
$\mathbb{R}^n$	*n-dimensional vector space of* $\mathbb{R}$
$\mathbb{R}$	*set of real numbers*
$\mathcal{O}$	*Landau symbol*
$\mathcal{T}$	*triangulation*

1 Introduction

In the most general sense, a population *is a collection of the same species of individuals, e.g., particles, which due to the process of synthesis are connected with each other.*

Population balance modeling has gained a lot of attention in the last few years, since it can be used to describe many particulate processes, e.g., crystallization, comminution, precipitation, polymerization, aerosol, and emulsion processes.

Particulate processes are characterized by the presence of dispersed systems [21]. In these systems, the dispersed phase is surrounded by a continuous one, the so-called dispersion or suspension medium. In general, a dispersed phase may represent solid particles, drops or bubbles. In particular, in the context of crystallization, the dispersed phase is represented by solid particles, i.e., crystal particles.

Crystallization is a separation and purification process which is frequently used in the chemical and pharmaceutical industries. The process starts by a phase change in which the crystalline product is obtained from a solution (suspension), which is made up of two or more species, where one is the solvent (liquid) and the other the solute(s) (solid) [60]. Industrial crystallization can operate continuously or batch-wise. Moreover, depending on the creation of supersaturation, it can be distinguished between the following types of crystallization from the solution: cooling crystallization, evaporative crystallization, drawing-out crystallization, and reaction crystallization. In our applications, we focus on the process of cooling crystallization. An advantage of the continuous over the batch process is that the optimal supersaturation can be easily maintained by a certain flow for a given volume suspension. Therefore, for continuous operations, the spatial separation of different population dynamical phenomena, i.e., nucleation, growth, aggregation, and breakage, is possible. On the other hand, kinetic data can be obtained by batch crystallization, which is less time consuming and less expensive. These data can be applied also to the design and operation of different types of continuous crystallizers [59].

The understanding of such processes has become a key issue for the optimal control of chemical, agrochemical, and pharmaceutical products. Hence, modeling and numerical simulations of population balances have become more and more important in the last few years [33, 64].

Since particles may have different sizes and properties, a population balance aims at investigating averaged properties of the whole population rather than the

behavior of each individual particle. Such averages can be described by particle size distributions (PSD), whose behavior can be modeled by population balance systems*. Moreover, the interaction between the particles and the continuous phase leads to different thermodynamical and mechanical phenomena, e.g., nucleation, growth, aggregation, breakage, and transport of particles [21, 33].*

From a mathematical point of view, population balance systems are modeled considering a flow field transporting the particles. This modeling results in a system of partial differential equations where the Navier–Stokes equations for the fluid velocity and pressure are coupled to convection-diffusion equations for the species concentration and the system temperature, and a transport equation for the PSD as it is illustrated in Fig. 1.1. In the considered applications, the temperature gradient is small enough, the solution is sufficiently dilute, and the size of the particles is also sufficiently small. All these aspects imply that the influence of the temperature, concentration, and particles on the flow field can be neglected.

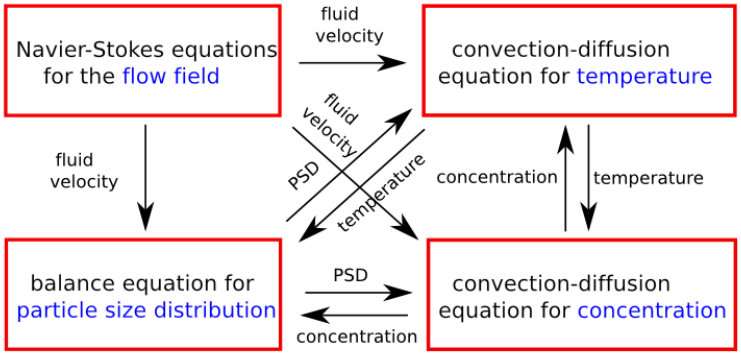

Figure 1.1: Schematic representation of the coupled problem.

Since analytic solutions to these systems are not available, the recourse to numerical methods is a self-evident consequence.

Altogether, a population balance system contains equations which are defined in domains with different dimensions. In fact, the flow field, the concentrations of dissolved species and the temperature are defined in a three-dimensional spatial domain, while the PSD depends also on the internal *coordinates, which are used to describe additional properties of the particles (e.g.,* diameter, volume*).*

In particular, **uni-variate** *and* **bi-variate** *population balance models are based on one- and two-dimensional geometrical characterizations of the individual particles (*diameter, volume, or main axis in the case of anisotropic particles*), resulting in four-dimensional (4D) and five-dimensional (5D) population*

balance systems. If more properties of the particles are utilized to characterize the crystallization processes, the extensions to the multivariate models might yield more reliable models of such processes, improving the accuracy of simulations.

From a computational point of view, the accurate and efficient simulation of such population balance systems poses a great challenge. Since the internal coordinate extends the dimension of the system at least by one, in many applications the assumption of an ideally mixed tank is considered, i.e., the dependency on space is neglected [54, 55, 56]. There are still only few approaches for the simulation of the equation for the PSD in the higher-dimensional domain [24, 44, 45, 71]. Currently, more widely used are several proposals for model simplification, which replace the higher-dimensional equation for the PSD by a system of equations in three dimensions. The most popular approaches in this direction are the quadrature method of moments (QMOM) [58] and the direct quadrature method of moments (DQMOM) [57]. These methods approximate the first moments of the PSD. However, the reconstruction of a PSD from a finite number of its moments is a severely ill-posed problem [14, 36]. Another approach for tackling the high-dimensionality of the population balance systems is based on operator-splitting schemes, i.e., the high-dimensional population balance equation is decoupled into two low-dimensional equations which are discretized separately [18, 19, 20]. Also this class of methods introduces an additional error by circumventing the solution of the higher-dimensional equation for PSD. So, the development of accurate and efficient numerical schemes to solve population balance systems is currently an important topic of research.

This thesis focuses on the treatment of fully coupled problems, e.g., (3D/4D) and (3D/5D), with methods based on direct discretizations. The considered (3D/4D) coupled system is an extension of the work proposed in [67]. In contrast to [67], our application, which models the process of urea synthesis, takes into account the temperature of the system and aggregation phenomena. In addition, the considered (3D/5D) coupled system, which models the process of potassium dihydrogen phosphate crystallization, presents a new contribution to the population balance community. All numerical simulations have been performed with the open-source finite element software MooNMD [38], which had to be extended for the considered application. A number of the numerical methods solving coupled systems of type (3D/4D) were available to be used in MooNMD, e.g., from the applications proposed in [7, 40]. While for the (3D/4D) coupled problem only a few modules of the used algorithms had to be implemented, the algorithms for the (3D/5D) coupled problem have been completely new implemented.

1.1 Outline of the thesis

Chapter 2 introduces the prototype equations which are usually contained in population balance systems, e.g., the Navier–Stokes equations, scalar convection-diffusion equations, and transport equations. General formulations of conservation laws provide the derivation of each individual equation. Since these equations are hard to solve analytically, or sometimes it is impossible, the alternative numerical treatment is an obvious issue. In order to solve these equations numerically, some general aspects are introduced, i.e., dimensionless formulation, incorporation of initial and boundary conditions, variational formulation, time and space discretization. Whereas the numerical methods for solving the Navier–Stokes and scalar convection-diffusion equations are based on finite element methods, less expensive schemes based on finite difference ideas are used for the computation of the PSD equations. In particular, the inf-sup stable Q_2/P_1^{disc} *finite element method (FEM) used for the Navier–Stokes equations, a linear finite element method flux-corrected transport (FEM–FCT) [46] used for scalar convection-diffusion equations, and different finite difference schemes, e.g., forward Euler upwind finite difference method (FWE–UPW–FDM), backward Euler upwind finite difference method (BWE–UPW–FDM), and a total variation diminishing (TVD) Runge–Kutta scheme combined with an essential non-oscillatory method of order three used for the transport equations (RK–ENO–FDM) are presented.*

An important issue for solving population balance systems is the coupling of the equations. In our model, we consider a one-way coupling, which means that the flow field used for the computation of concentration, temperature, and PSD equations is not influenced by these quantities. The back coupling will be neglected here since sufficiently small amount of particles are suspended in a dilute dispersion medium and sufficiently small temperature gradients are present in the system.

Chapter 3 considers a laboratory experiment [6], a synthesis of urea particles for which measurement data are available. The uni-variate population balance system modeling the considered application takes into account the nucleation, the growth, the aggregation, and transport of urea particles. Direct discretizations for simulating the uni-variate population balance system including the distribution of temperature and concentration as well as including aggregation seem to be first time presented. The model of [67] was extended by taking into account a temperature profile and including an aggregation kernel, which is of utmost importance from the point of view of chemical engineering, since the behavior of the particles is driven by aggregation. The used kernel consists of two parts, one describing the aggregation by Brownian motion and the other one describing shear-induced aggregation.

An important aspect for reliable comparisons is the use of accurate numerical methods. Thus, the flow field will be simulated by a higher-order finite element method, the equations for the concentration of dissolved urea and for the temperature are computed by one of the most accurate stabilized finite element methods [46], and the aggregation integrals are computed by a modern approach from [28, 29, 30]. Only the convective part of the equation for the PSD is discretized, for efficiency reasons, with rather simple schemes, based on finite difference ideas. Results with the examined schemes are illustrated in Fig. 1.4. With these methods, parameters for the aggregation kernel could be

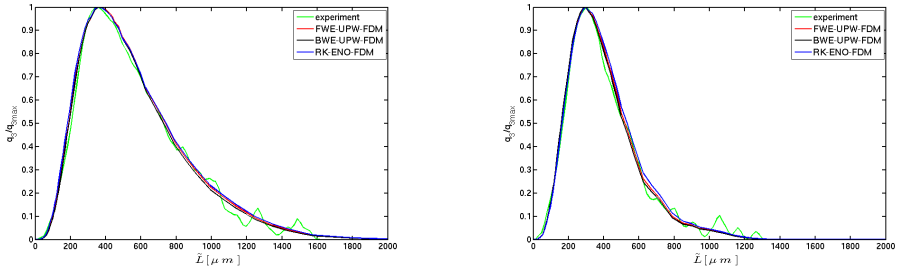

Figure 1.2: Space-time-averaged normalized volume fraction at the outlet for different methods; flow rate $\tilde{V}_r = 30$ ml/min (left); flow rate $\tilde{V}_r = 90$ ml/min (right).

identified for two experimental setups which give results that agree well with the experimental data. Reasons for differences of the optimal parameters between both examples are discussed. Detailed studies of the PSD for different nodes of the grid at the outlet highlight the impact of the individual terms of the aggregation kernel.

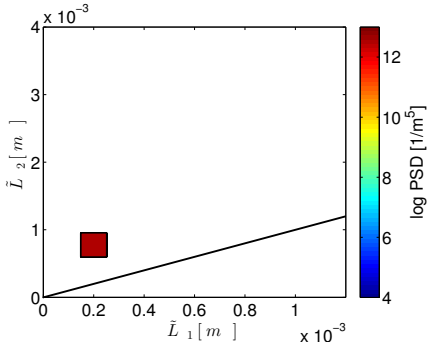

Figure 1.3: Initial distribution for KDP model.

In Chapter 4, the bi-variate modeling of the potassium dihydrogen phosphate crystallization process is derived. A lot of particulate products encountered in pharmaceutical and chemical industries show anisotropic morphologies. Thus, extensions to the multivariate population balance systems yield more reliable models of such processes, improving the accuracy of simulations. However, only particle transport, growth and nucleation will be taken into account, since, to date, there are no predictive models for the aggregation kernels. To our best knowledge, the proposed numerical methods for solving bi-variate population system are new contribution to the field of a population balance modeling. Considering the same experimental setup as in Chapter 3, the five-dimensional domain will be a tensor product of intervals. Measurement data are not available for this example. Therefore, this chapter will highlight the differences in the numerical results in the cases that a very cheap but low order method is used for the discretization of the 5D transport operator versus a more expensive but higher order method. These methods are examined for a given initial distribution, a square pulse, see Fig. 1.3.

The numerical results based on the examined finite differences schemes are illustrated in Fig. 1.4. In these plots, it can be observed that the PSD computed with FWE–UPW–FDM is much stronger smeared with respect to the internal coordinates than the PSD computed with RK–ENO–FDM. A detailed comparison of the results obtained with both schemes will show that some aspects of these results are qualitatively different.

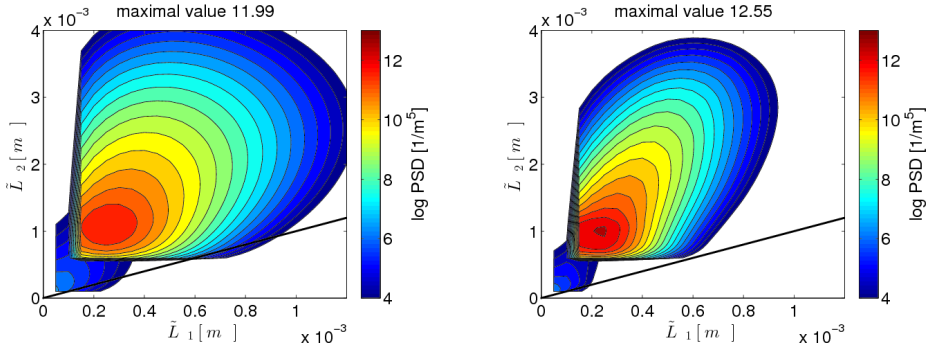

Figure 1.4: (Logarithm of the) PSD at the center of the tube close to the outlet; FWE–UPW–FDM (left) and RK–ENO–FDM (right).

In Chapter 5 the considered approaches will be summarized. This chapter concludes with an outlook to future investigation.

2 Aspects of the numerical simulation of population balance systems

In this chapter, the system of equation modeling population balances is derived. Such systems contain equations which are defined in domain with different dimensions. Whereas Navier–Stokes describing the flow field and the convection-diffusion equations describing the concentration of dissolved species and the temperature are given in three-dimensional spatial domain, the transport equation describing the behavior of the whole population of particles, i.e., particle size distribution, is defined in higher dimensional domain, e.g., four-dimensional and five-dimensional domain. In general, each individual equations accounting for the population balance system is hard or in the most of the cases impossible to be solved analytically. Therefore, numerical methods have to be applied to compute approximations of the solutions. For solving the incompressible Navier–Stokes equations and the scalar convection-diffusion equations methods based on finite element schemes are introduced. Cheaper schemes based on finite difference ideas are considered for the computation of the PSD equations.

Moreover, population balance systems describe the interaction between particles and surrounding medium which are present in dispersed systems. For the considered applications, this fact leads to different thermodynamical and mechanical phenomena, e.g., nucleation, growth, and aggregation.

2.1 The Navier–Stokes equations

From the point of view of continuum mechanics, the motion of isothermal Newtonian fluids, e.g., water, air, oil, etc, can be described by the Navier–Stokes equations.

Unsteady incompressible flows can be described by the Navier–Stokes equations for the velocity and pressure:

$$\begin{aligned} \tilde{\rho}\tilde{\mathbf{u}}_t - \mu\Delta\tilde{\mathbf{u}} + \tilde{\rho}\left((\tilde{\mathbf{u}}\cdot\nabla)\tilde{\mathbf{u}}\right) + \nabla\tilde{p} &= \tilde{\rho}\tilde{\mathbf{g}} \quad \text{in } (0,\tilde{t}_{\text{end}}]\times\tilde{\Omega}, \\ \nabla\cdot\tilde{\mathbf{u}} &= 0 \quad \text{in } (0,\tilde{t}_{\text{end}}]\times\tilde{\Omega}, \end{aligned} \tag{2.1}$$

where

- $\tilde{\Omega}\subset\mathbb{R}^3$ $\left[\mathrm{m}^3\right]$ *is the flow domain,*
- $\tilde{\mathbf{u}}$ $\left[\frac{\mathrm{m}}{\mathrm{s}}\right]$ *is the velocity field,*

- $\tilde{p}$ $\left[\frac{\text{kg}}{\text{m s}^2}\right]$ *is the pressure,*
- $\tilde{\rho}$ $\left[\frac{\text{kg}}{\text{m}^3}\right]$ *is the fluid density,*
- μ $\left[\frac{\text{kg}}{\text{m s}}\right]$ *is the dynamic viscosity of the fluid,*
- $\tilde{\mathbf{g}}$ *is the body force (gravity, centrifugal and Coriolis),*
- $\tilde{t}_{\text{end}}$ [s] *is the final time.*

Problem (2.1) *has to be equipped with an initial condition and with boundary conditions.*

From a mathematical point of view, the Navier–Stokes equations represent a nonlinear partial differential equations, since the third term in the first equation of (2.1), $\tilde{\rho}\,((\tilde{\mathbf{u}}\cdot\nabla)\tilde{\mathbf{u}})$ *is a nonlinear term. The first equation in (2.1) describes the conservation of linear momentum and the second one describes the conservation of the mass. The first and third term in the momentum equation in (2.1) represent a convective transport and the second term a diffusive or viscous transport. The convective term is called the convective acceleration and it is caused by a change in velocity over position.*

A characteristic parameter of the Navier–Stokes equations is the Reynolds number

$$Re = \frac{\tilde{\rho}\cdot u_\infty \cdot l_\infty}{\mu}\,[\cdot]\,,$$

where u_∞ $\left[\frac{\text{m}}{\text{s}}\right]$ *is a characteristic velocity of the flow and* l_∞ [m] *is a characteristic length scale of the problem. Based on the Reynolds number, flows can be classified as follows:*

- *Re small:* $(\tilde{\mathbf{u}},\tilde{p})$ *does not depend on the time, the flow is steady-state,*
- *Re medium: the flow is laminar but time dependent,*
- *Re large: the flow is turbulent.*

The applications considered in this thesis can be described by a steady flow, i.e., velocity and pressure do not change in time. In this case, the stationary Navier–Stokes equations read:

$$\begin{aligned} -\mu\Delta\tilde{\mathbf{u}} + \tilde{\rho}\,((\tilde{\mathbf{u}}\cdot\nabla)\tilde{\mathbf{u}}) + \nabla\tilde{p} &= \tilde{\rho}\tilde{\mathbf{g}} \quad \text{in } \tilde{\Omega}, \\ \nabla\cdot\tilde{\mathbf{u}} &= 0 \quad \text{in } \tilde{\Omega}, \end{aligned} \tag{2.2}$$

equipped with appropriate boundary conditions.

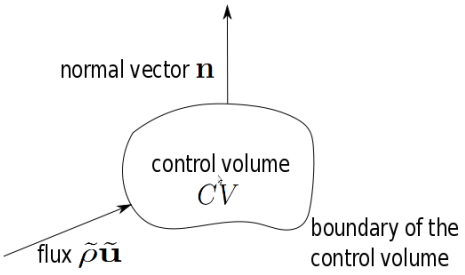

Figure 2.1: Control volume.

2.1.1 The derivation

Below, we shortly introduce the derivation of Navier–Stokes equations, following [17, 32, 50, 76].

The classical way of continuum mechanics for deriving these equations is based on a closed system, the so-called control mass system (CMS), which is defined as an arbitrary quantity of mass of fixed identity. In fluid flows it is difficult to follow the path of a specific particle of fluid. Therefore, it is more convenient to deal with a specific spatial region in the neighborhood of the product of interest, the so-called control volume system (CVS). It is assumed that $\tilde{\mathbf{u}}$, $\tilde{\rho}$, $\tilde{p}$ *are sufficiently smooth functions in the domain* $\tilde{\Omega}$ *and the time interval* $(0, \tilde{t}_{\text{end}}]$.

Let CV *be an arbitrary volume in* $\tilde{\Omega}$ *fixed in space and with a sufficiently smooth surface* $\partial\tilde{\Omega}$. *The volume* CV, *illustrated as in Fig. 2.1, is called control volume. The conservation of mass states that the mass of a closed system will remain constant over time. Thus, mass is:*

$$m(\tilde{t}) = \int_{CV} \tilde{\rho}(\tilde{t}, \tilde{\mathbf{x}}) d\tilde{\mathbf{x}} = const \ [\text{kg}].$$

Further, if mass is conserved in the control volume CV *then the rate of change of mass in* CV *has to be equal to the flux of mass* $\tilde{\rho}\tilde{\mathbf{u}} \left[\frac{\text{kg}}{\text{m}^2\ \text{s}}\right]$ *across the boundary* ∂CV *of* CV

$$\frac{d}{d\tilde{t}} m(\tilde{t}) = \frac{d}{d\tilde{t}} \int_{CV} \tilde{\rho}(\tilde{t}, \tilde{\mathbf{x}}) d\tilde{\mathbf{x}} = \int_{\partial CV} (\tilde{\rho}\tilde{\mathbf{u}})(\tilde{t}, s)\mathbf{n}(s) ds, \tag{2.3}$$

where $\mathbf{n}(s)$ *is the outward pointing unit normal on* $s \in \partial CV$.

Using Gauss' divergence theorem (all function are assumed to be sufficiently smooth), one obtains:

$$\int_{CV} \nabla \cdot (\tilde{\rho}\tilde{\mathbf{u}})(\tilde{t}, \tilde{\mathbf{x}}) d\tilde{\mathbf{x}} = -\int_{\partial CV} (\tilde{\rho}\tilde{\mathbf{u}})(\tilde{t}, s)\mathbf{n}(s) ds.$$

Further, inserting (2.3) into the last equation leads to

$$\int_{CV} \frac{\partial \tilde{\rho}}{\partial \tilde{t}}(\tilde{t}, \tilde{\mathbf{x}}) + \nabla \cdot (\tilde{\rho}\tilde{\mathbf{u}})(\tilde{t}, \tilde{\mathbf{x}}) d\tilde{\mathbf{x}} = 0.$$

Thus,

$$\left(\frac{\partial \tilde{\rho}}{\partial \tilde{t}} + \nabla \cdot (\tilde{\rho}\tilde{\mathbf{u}}) \right)(\tilde{t}, \tilde{\mathbf{x}}) = 0 \ \forall \tilde{t} \in (0, \tilde{t}_{\text{end}}], \ \tilde{\mathbf{x}} \in \tilde{\Omega}, \tag{2.4}$$

since CV was chosen as an arbitrary control volume. Equation (2.4) is the so-called continuity equation.

A fluid is called homogeneous if density does not vary over space and it is called incompressible if density does not vary over time. Thus, for incompressible and homogeneous fluids, one has $\tilde{\rho}(t, \tilde{\mathbf{x}}) =: const = \rho > 0$ *and the last equation becomes*

$$\nabla \cdot \tilde{\mathbf{u}} = 0 \ \forall \tilde{t} \in (0, \tilde{t}_{\text{end}}], \ \tilde{\mathbf{x}} \in \tilde{\Omega},$$

which is the second equation in (2.1).

The conservation of linear momentum states that the rate of change of the linear momentum must be equal to the net force acting on a collection of particles. This aspect describes Newton's second law of motion

$$\mathbf{F} = m \cdot \mathbf{a},$$

where $\mathbf{F}$ $[N]$ *is the net force,* m [kg] *is the mass, and* $\mathbf{a}$ $\left[\frac{\text{m}}{\text{s}^2}\right]$ *is the acceleration.*

The momentum $\mathbf{m}$ *in a control volume CV is given by*

$$\mathbf{m}(\tilde{t}) = \int_{CV} \tilde{\rho}\tilde{\mathbf{u}} d\tilde{\mathbf{x}}.$$

By Newton's second law, the change of momentum is given by the sum of forces acting on the volume, that means

$$\frac{d}{dt}\mathbf{m}(\tilde{t}) = \sum \tilde{\mathbf{f}}.$$

In the given physical situation, there are the following kinds of forces:

- *volume forces (e.g., gravity or other external forces, including sources and sinks), which are given by a volume integral*

$$\int_{CV} \tilde{\rho}\tilde{g} d\tilde{\mathbf{x}},$$

- *surface forces (e.g., pressure, viscous forces, or other internal forces), which are given by a surface integral*

$$\int_{\partial CV} \boldsymbol{\sigma}\mathbf{n} ds,$$

where

$$\boldsymbol{\sigma} = \begin{pmatrix} \sigma_{11} & \sigma_{12} & \sigma_{13} \\ \sigma_{21} & \sigma_{22} & \sigma_{23} \\ \sigma_{31} & \sigma_{32} & \sigma_{33} \end{pmatrix}$$

is the symmetric stress tensor.

Now, one can express Newton's second law as

$$\frac{d}{dt}\mathbf{m}(\tilde{t}) = \int_{CV} \tilde{\rho}\tilde{g} d\tilde{\mathbf{x}} + \int_{\partial CV} \boldsymbol{\sigma}\mathbf{n} ds.$$

Further, one considers a fluid particle at time $\tilde{t}$ *and position* $\tilde{\mathbf{x}} = (\tilde{x}_1, \tilde{x}_2, \tilde{x}_3)^T$ *with the velocity* $\tilde{\mathbf{u}}(\tilde{t}, \tilde{\mathbf{x}}) = (\tilde{u}_1, \tilde{u}_2, \tilde{u}_3)^T$ *and a small time interval* $\Delta\tilde{t}$.

A linear extrapolation of the particle path states the particle has the position $\tilde{\mathbf{x}} + \Delta\tilde{t}\tilde{\mathbf{u}}$ *at the time* $\tilde{t} + \Delta\tilde{t}$. *The acceleration of the particle is*

$$\mathbf{a}(\tilde{t}, \tilde{\mathbf{x}}) = \frac{d\tilde{\mathbf{u}}}{d\tilde{t}}(\tilde{t}, \tilde{\mathbf{x}}) = \lim_{\Delta\tilde{t}\to 0} \frac{\tilde{\mathbf{u}}(\tilde{t} + \Delta\tilde{t}, \tilde{\mathbf{x}} + \Delta\tilde{t}\tilde{\mathbf{u}}(\tilde{t}, \tilde{\mathbf{x}})) - \tilde{\mathbf{u}}(\tilde{t}, \tilde{\mathbf{x}}))}{\Delta\tilde{t}}.$$

By using the linear Taylor series approximation with respect to $\tilde{\mathbf{x}}$ *, it follows that*

$$\begin{aligned} \frac{d\tilde{\mathbf{u}}}{d\tilde{t}}(\tilde{t}, \tilde{\mathbf{x}}) &= \lim_{\Delta\tilde{t}\to 0} \frac{1}{\Delta\tilde{t}} \Big[\tilde{\mathbf{u}}(\tilde{t}, \tilde{\mathbf{x}}) + \frac{\partial\tilde{\mathbf{u}}}{\partial\tilde{x}_1}\tilde{u}_1\Delta\tilde{t} + \frac{\partial\tilde{\mathbf{u}}}{\partial\tilde{x}_2}\tilde{u}_2\Delta\tilde{t} + \frac{\partial\tilde{\mathbf{u}}}{\partial\tilde{x}_3}\tilde{u}_3\Delta\tilde{t} \\ &\quad + \frac{\partial\tilde{\mathbf{u}}}{\partial\tilde{t}}\Delta\tilde{t} + \mathcal{O}((\Delta\tilde{t})^2) + \mathcal{O}((\Delta\tilde{t})^3) + \cdots - \tilde{\mathbf{u}}(\tilde{t}, \tilde{\mathbf{x}}) \Big] \\ &= \lim_{\Delta\tilde{t}\to 0} \Big[\frac{\partial\tilde{\mathbf{u}}}{\partial\tilde{x}_1}\tilde{u}_1 + \frac{\partial\tilde{\mathbf{u}}}{\partial\tilde{x}_2}\tilde{u}_2 + \frac{\partial\tilde{\mathbf{u}}}{\partial\tilde{x}_3}\tilde{u}_3 + \frac{\partial\tilde{\mathbf{u}}}{\partial\tilde{t}} + \cdots \mathcal{O}(\Delta\tilde{t}) \Big], \end{aligned}$$

where $\mathcal{O}$ is the Landau notation which is used to describe the limiting behavior of the function when the argument tends to a particular value. Assuming that $\Delta\tilde{t} \to 0$, this reduces to

$$\frac{d\tilde{\mathbf{u}}}{d\tilde{t}}(\tilde{t}, \tilde{\mathbf{x}}) = \tilde{\mathbf{u}}_t + ((\tilde{\mathbf{u}} \cdot \nabla)\tilde{\mathbf{u}}).$$

In other words, the term $m \cdot \mathbf{a}$ is modeled by the first order approximation in an arbitrary control volume CV

$$\int_{CV} \tilde{\rho}(\tilde{\mathbf{u}}_t + (\tilde{\mathbf{u}} \cdot \nabla)\tilde{\mathbf{u}}) d\tilde{\mathbf{x}}.$$

This term has to be in balance with the net forces acting on CV. Therefore, it follows that

$$\int_{CV} \tilde{\rho}(\tilde{\mathbf{u}}_t + (\tilde{\mathbf{u}} \cdot \nabla)\tilde{\mathbf{u}}) d\tilde{\mathbf{x}} = \int_{CV} \tilde{\rho}\tilde{g} d\tilde{\mathbf{x}} + \int_{\partial CV} \boldsymbol{\sigma}\mathbf{n} ds.$$

Applying Gauss' divergence theorem for

$$-\int_{\partial CV} \boldsymbol{\sigma}\mathbf{n} ds = \int_{CV} \nabla \cdot \boldsymbol{\sigma} d\tilde{\mathbf{x}},$$

one obtains

$$\tilde{\rho}(\tilde{\mathbf{u}}_t + (\tilde{\mathbf{u}} \cdot \nabla)\tilde{\mathbf{u}}) = \tilde{\rho}\tilde{g} - \nabla \cdot \boldsymbol{\sigma}.$$

This is the equation of motion of the velocity field. In the case of viscous fluids, the stress tensor can be decomposed into a pressure part and a viscosity part

$$\boldsymbol{\sigma} = \underbrace{-\tilde{p}\mathbb{I}}_{pressure} + \underbrace{\boldsymbol{\tau}(\nabla\tilde{\mathbf{u}})}_{viscosity},$$

where $\boldsymbol{\tau}$ is the strain tensor and $\mathbb{I}$ is the unit tensor. In the case of Newtonian fluids, $\boldsymbol{\tau}(\nabla\tilde{\mathbf{u}})$ has to fulfill:

- *linearty in $\nabla\tilde{\mathbf{u}}$,*
- *rotationally invariant,*
- *symmetry.*

This leads to the model

$$\boldsymbol{\tau}(\nabla\tilde{\mathbf{u}}) = \varsigma(\nabla \cdot \tilde{\mathbf{u}})\mathbb{I} + 2\mu\mathbb{D}$$

where

$$\mathbb{D} = \frac{\nabla\tilde{\mathbf{u}} + (\nabla\tilde{\mathbf{u}})^T}{2}$$

is the deformation tensor and ς is a viscosity constant. Using the identities:

$$\begin{aligned} \nabla \cdot \nabla\tilde{\mathbf{u}} &= \Delta\tilde{\mathbf{u}}, \\ \nabla \cdot (\nabla\tilde{\mathbf{u}})^T &= \nabla(\nabla \cdot \tilde{\mathbf{u}}), \\ \nabla \cdot [(\nabla \cdot \tilde{\mathbf{u}})\mathbb{I}] &= \nabla(\nabla \cdot \tilde{\mathbf{u}}), \end{aligned}$$

and the relation for incompressible fluids

$$\nabla \cdot \tilde{\mathbf{u}} = 0,$$

the first equation in (2.1) will be obtained.

2.1.2 The dimensionless form

Our numerical simulations are based on the dimensionless form of Navier–Stokes equations, which can be derived introducing the following dimensionless quantities:

$$\mathbf{u} = \frac{\tilde{\mathbf{u}}}{u_\infty},\ p = \frac{\tilde{p}}{p_\infty},$$

$$\mathbf{x} = (x_1, x_2, x_3) = \left(\frac{\tilde{x}_1}{l_\infty}, \frac{\tilde{x}_2}{l_\infty}, \frac{\tilde{x}_3}{l_\infty}\right),\ p_\infty = \tilde{\rho}u_\infty^2,\ \mathbf{g} = \frac{l_\infty}{u_\infty^2}\tilde{\mathbf{g}}.$$

Inserting these relations into (2.2), leads to

$$\rho\left((u_\infty\mathbf{u} \cdot \nabla)\frac{u_\infty}{l_\infty}\mathbf{u}\right) + \frac{p_\infty}{l_\infty}\nabla p - \nu\frac{u_\infty}{l_\infty^2}\Delta\mathbf{u} = \rho\tilde{\mathbf{g}}.$$

By rescaling the dimensionless form of (2.2) the following is obtained:

$$\begin{aligned} -Re^{-1}\Delta\mathbf{u} + (\mathbf{u} \cdot \nabla)\mathbf{u} + \nabla p &= \mathbf{g} \quad \text{in } \Omega, \\ \nabla \cdot \mathbf{u} &= 0 \quad \text{in } \Omega, \end{aligned} \tag{2.5}$$

with

- $Re = \dfrac{l_\infty u_\infty}{\nu}$ *the Reynolds number,*
- $\nu = \dfrac{\mu}{\rho}$ *the kinematic viscosity,*
- Ω *the dimensionless domain.*

Based on dimensional analysis, two steady-state flows are similar if they have the same Reynolds numbers [23].

2.1.3 Boundary conditions

In order to close the Navier–Stokes equations, appropriate initial and boundary conditions need to be applied. Since (2.5) is not time-dependent, only spatial boundary conditions are required. There are several types of boundary conditions which can be prescribed for incompressible flows. Only those boundary conditions are introduced which are used in the considered application.

The Dirichlet boundary condition prescribes the velocity field on a part of the boundary:

$$\mathbf{u}(\mathbf{x}) = \mathbf{u}_D(\mathbf{x}) \text{ at } \Gamma_D \subset \Gamma,$$

where $\Gamma = \partial\Omega$ *is the boundary of* Ω.

The no-slip boundary condition is a particular case of the Dirichlet boundary condition, namely

$$\mathbf{u}_D(\mathbf{x}) = \mathbf{0} \text{ at } \Gamma_D.$$

One can prescribe also the normal stress at a part of the boundary. It takes the form

$$\boldsymbol{\sigma} \cdot \mathbf{n} = \mathbf{u}_N \text{ at } \Gamma_N \subset \Gamma.$$

In particular, the outflow or do-nothing boundary condition, namely

$$\mathbf{u}_N = \mathbf{0} \text{ at } \Gamma_{\text{out}} \subset \Gamma,$$

is used in flow problems where no other boundary conditions are prescribed at the outflow. This condition states that the normal stress vanishes on the boundary part Γ_{out}.

2.1.4 The variational formulation

The stationary Navier–Stokes equations (2.5) will be closed with the following boundary conditions: Dirichlet boundary condition at the inflow, do-nothing boundary condition at the outflow, and no-slip boundary condition for the rest of the boundary, as below

$$\begin{aligned} -Re^{-1}\Delta\mathbf{u} + (\mathbf{u}\cdot\nabla)\mathbf{u} + \nabla p &= \mathbf{g} && \text{in } \Omega, \\ \nabla\cdot\mathbf{u} &= 0 && \text{in } \Omega, \\ \mathbf{u} &= \mathbf{u}_D && \text{on } \Gamma_D, \\ \boldsymbol{\sigma}\mathbf{n} &= \mathbf{0} && \text{on } \Gamma_{\text{out}}, \\ \mathbf{u} &= \mathbf{0} && \text{on } \Gamma \setminus (\Gamma_D \cup \Gamma_{\text{out}}). \end{aligned} \tag{2.6}$$

In order to achieve the variational or weak formulation some suitable function spaces are introduced.

Sobolev spaces of order m are given by

$$H^m(\Omega) = \left\{ u : \int_\Omega \sum_{|\alpha| \leq m} |\partial^\alpha u|^2 d\mathbf{x} < \infty \right\}.$$

They can be endowed with the norm

$$\| \cdot \|_{H^m} = \left(\int_\Omega \sum_{|\alpha| \leq m} |\partial^\alpha u|^2 d\mathbf{x} \right)^{\frac{1}{2}},$$

and the inner product

$$(u, v)_{H^m} = \int_\Omega \sum_{|\alpha| \leq m} |\partial^\alpha u \partial^\alpha v| d\mathbf{x}.$$

In particular, the Lebesgue space $L^2(\Omega)$ is given by

$$L^2(\Omega) = H^0(\Omega) = \{ u : \int_\Omega |u|^2 \mathbf{x} < \infty \},$$

with the corresponding norm and the corresponding inner product

$$\| \cdot \| = \left(\int_\Omega |u|^2 d\mathbf{x} \right)^{\frac{1}{2}},$$

$$(u, v) = \int_\Omega uv d\mathbf{x}.$$

The choice of the function spaces depends on the specific boundary condition imposed for the considered application and they are given by:

$$Q = \{ q : q \in L^2(\Omega) \},$$

$$V_0 = \{ \mathbf{v} : \mathbf{v} \in (H^1(\Omega))^3, \mathbf{v}_{|\Gamma \setminus \Gamma_{\text{out}}} = \mathbf{0} \},$$

$$V_D = \{ \mathbf{v} : \mathbf{v} \in (H^1(\Omega))^3, \mathbf{v}_{|\Gamma_D} = \mathbf{u}_D, \mathbf{v}_{|\Gamma \setminus (\Gamma_D \cup \Gamma_{\text{out}})} = \mathbf{0} \}.$$

For deriving the weak formulation, the equations (2.5) must be multiplied with test functions and integrated on Ω.

Thus, the variational formulation of the problem is to find $(\mathbf{u}, p) \in V_D \times Q$

$$\begin{array}{rcll} \int_\Omega (-Re^{-1}\Delta\mathbf{u} + (\mathbf{u}\cdot\nabla)\mathbf{u} + \nabla p)\cdot\mathbf{v}d\Omega & = & \int_\Omega \mathbf{g}\cdot\mathbf{v}d\mathbf{x}, & \forall \mathbf{v}\in V_0, \\ \int_\Omega (\nabla\cdot\mathbf{u})\cdot q d\mathbf{x} & = & 0 & \forall q \in Q. \end{array} \tag{2.7}$$

Applying integration by parts, (2.7) can be written as:

$$\begin{aligned} \int_\Omega Re^{-1}\nabla\mathbf{u}\cdot\nabla\mathbf{v}d\mathbf{x} \quad &+ \quad \int_\Omega (\mathbf{u}\cdot\nabla)\mathbf{u}\cdot\nabla\mathbf{v}d\mathbf{x} - \int_\Omega p\cdot\nabla\cdot\mathbf{v}d\mathbf{x} \\ &= \int_\Omega \mathbf{g}\cdot\mathbf{v}d\mathbf{x} + \int_\Gamma \mathbf{n}\boldsymbol{\sigma}\cdot\mathbf{v}ds \\ \int_\Omega (\nabla\cdot\mathbf{u})\cdot q d\mathbf{x} \quad &= \quad 0. \end{aligned} \tag{2.8}$$

The second term on the right-hand side in (2.8),

$$\int_\Gamma \mathbf{n}\boldsymbol{\sigma}\cdot\mathbf{v}d\Gamma,$$

vanishes on the boundary due to the choice of function spaces V_D, V_0 *and*

$$\mathbf{n}\boldsymbol{\sigma} = \mathbf{0} \ \textit{at}\ \Gamma_{\text{out}},$$

$$\mathbf{v} = \mathbf{0} \ \textit{at}\ \Gamma \setminus \Gamma_{\text{out}}.$$

Now (2.8) can be written in the form:

Find $\mathbf{u} \in V_D$ *and* $p \in Q$ *such that*

$$\begin{array}{rcll} Re^{-1}(\nabla\mathbf{u},\nabla\mathbf{v}) + ((\mathbf{u}\cdot\nabla)\mathbf{u},\mathbf{v}) - (p,\nabla\cdot\mathbf{v}) & = & (\mathbf{g},\mathbf{v}), & \forall \mathbf{v}\in V_0, \\ (\nabla\cdot\mathbf{u},q) & = & 0 & \forall q \in Q. \end{array} \tag{2.9}$$

2.1.5 The linearization

The problem (2.9) corresponds to a nonlinear algebraic system of equations. Therefore, these equations have to be linearized. The nonlinear system (2.9) is solved iteratively. An iterative procedure consists in:

- *fix an initial guess* $(\mathbf{u}_0, p_0)$*;*
- *while (no convergence) do*
  - *linearization of the nonlinear equations based on previous solution* $(\mathbf{u}_k, p_k) = (\mathbf{u}_{k-1}, p_{k-1})$*;*

– *solve the resulting system of linear equations.*

We are using here a fixed point iteration. For the time-dependent Navier–Stokes equations, better results were obtained with a fixed point iteration in comparison with Newton's method [35]. The fix point linearization consists in treating explicitly the convective velocity:

$$(\mathbf{u}_k \cdot \nabla)\mathbf{u}_k \approx (\mathbf{u}_{k-1} \cdot \nabla)\mathbf{u}_k.$$

Using this linearization in the equation (2.9) leads to the following:

Given $(\mathbf{u}_{k-1}, p_{k-1})$*, compute* $(\mathbf{u}_k, p_k)$ *by*

$$\begin{array}{rcl} Re^{-1}(\nabla\mathbf{u}_k, \nabla\mathbf{v}) + ((\mathbf{u}_{k-1} \cdot \nabla)\mathbf{u}_k, \mathbf{v}) - (p_k, \nabla\mathbf{v}) & = & (\mathbf{g}, \mathbf{v}), \\ (\nabla \cdot \mathbf{u}_k, q) & = & 0, \end{array} \tag{2.10}$$

for all $(\mathbf{v}, q) \in V_0 \times Q$*,* $k = 1, 2, 3 \cdots$*. The linearized form of NSE* (2.10) *yields so-called Oseen equations.*

2.1.6 The space discretization

There are various methods for solving numerically partial differential equations: finite difference methods (FDM), finite element methods (FEM), finite volume methods (FVM), spectral methods, vortex methods, boundary element methods and this is not a complete list. No one method dominates in computational fluid dynamics. Here, the method of choice for solving the Navier–Stokes equations is the finite element method [8, 9, 11, 22, 25]. The Galerkin finite element method consists in replacing infinite dimensional spaces by finite dimensional spaces.

Let V_D^h *be an approximation of* V_D*,* V_0^h *be an approximation of* V_0*, and* Q^h *be an approximation of* Q*. The finite element spaces are based on a triangulation of the domain. Let* T_h *be a triangulation of* Ω *which can consist in the three-dimensional case of tetrahedra or hexahedra.*

The finite element problem reads as follows:

Find $(\mathbf{u}^h, p^h) \in V_D^h \times Q^h$ *such that*

$$\begin{array}{rcl} Re^{-1}(\nabla\mathbf{u}^h, \nabla\mathbf{v}^h) + \big((\mathbf{u}^h \cdot \nabla)\mathbf{u}^h, \mathbf{v}^h\big) - (p^h, \nabla \cdot \mathbf{v}^h) & = & (\mathbf{g}^h, \mathbf{v}^h) \\ (\nabla \cdot \mathbf{u}^h, q^h) & = & 0, \end{array} \tag{2.11}$$

for all $\mathbf{v}^h \in V_0^h$ *and for all* $q^h \in Q^h$*.*

For simplicity of presentation, let $\{\varphi_i^h\}$ *be a basis of* V_0^h *and* $\{\psi_i^h\}$ *be a basis of* Q^h*:*

$$V_0^h = span\left\{ \begin{pmatrix} \varphi_i^h \\ 0 \\ 0 \end{pmatrix}, \begin{pmatrix} 0 \\ \varphi_i^h \\ 0 \end{pmatrix}, \begin{pmatrix} 0 \\ 0 \\ \varphi_i^h \end{pmatrix} \right\}_{i=1}^{N_u},$$

$$Q^h = span\left\{\psi_j^h\right\}_{i=1}^{N_p},$$

where N_u, N_p is the number of unknowns (degrees of freedom) for the velocity and pressure, respectively.

Therefore, the unknown solution has the representation:

$$\mathbf{u}^h = \sum_{j=1}^{3N_u} u_j \varphi_j^h + \mathbf{u}_0, \quad p^h = \sum_{j=1}^{N_p} p_j \psi_j^h, \tag{2.12}$$

with the unknown values $\{u_j\}$, $\{p_j\}$. The function $\mathbf{u}_0$ must be chosen such that $\mathbf{u}^h$ satisfies the essential boundary condition, which means:

$$\mathbf{u}_0 = \mathbf{u}_D \, on \, \Gamma_D, \tag{2.13}$$

$$\mathbf{u}_0 = 0 on \, \Gamma \setminus (\Gamma_D \cup \Gamma_{\text{out}}). \tag{2.14}$$

Inserting (2.12) into (2.11) one obtains:

$$\begin{aligned} (Re^{-1}\nabla \mathbf{u}^h, \nabla \varphi_i^h) &= \sum_{j=1}^{dN_u} u_j (Re^{-1}\nabla \varphi_j^h, \nabla \varphi_i^h) + (Re^{-1}\nabla \mathbf{u}_0, \nabla \varphi_i^h), \\ ((\tilde{\mathbf{u}}^h \cdot \nabla)\mathbf{u}^h, \varphi_i^h) &= \sum_{j=1}^{dN_u} u_j ((\tilde{\mathbf{u}}^h \cdot \nabla)\varphi_j^h, \varphi_i^h) + ((\tilde{\mathbf{u}}^h \cdot \nabla)\mathbf{u}_0, \varphi_i^h), \\ (p^h, \nabla \cdot \psi_i^h) &= \sum_{j=1}^{N_p} p_j (\psi_j, \nabla \cdot \varphi_i^h), \end{aligned} \tag{2.15}$$

where $\tilde{\mathbf{u}}^h$ is the current approximation of the velocity, see Sec. 2.1.5. The system (2.10) is a finite dimensional linear system of equations. The following matrices and vectors are defined:

$$\begin{aligned} \mathbf{A} = (a_{ij}) &= (Re^{-1}\nabla u_j^h, \nabla \varphi_j^h) + (\tilde{\mathbf{u}}^h \cdot \nabla)\varphi_j^h, \varphi_i^h), \\ \mathbf{B}^T = (b_{ji}) &= (\psi_j^h, \nabla \cdot \varphi_i^h), \\ \mathbf{B} = (b_{ij}) &= (\nabla \cdot \varphi_i^h), \psi_j^h), \\ \mathbf{u} &= (u_1, ..., u_{dN_u})^T, \end{aligned}$$

$$\begin{aligned} p &= (p_1, ..., p_{N_p})^T, \\ \mathbf{g} &= ((\mathbf{g}^h, \varphi_i^h) - (Re^{-1}\nabla \mathbf{u}_0, \nabla \varphi_i^h) - ((\tilde{\mathbf{u}}^h \cdot \nabla)\mathbf{u}_0, \varphi_i^h)). \end{aligned}$$

This leads to the following form of the linear system, which is called saddle point form,

$$\begin{pmatrix} \mathbf{A} & \mathbf{B}^T \\ \mathbf{B} & 0 \end{pmatrix} \begin{pmatrix} \mathbf{u} \\ p \end{pmatrix} = \begin{pmatrix} \mathbf{g} \\ 0 \end{pmatrix}. \tag{2.16}$$

The dimension of the system depends on the dimension of V_0^h and Q^h with

$$dimension = 3 \cdot dim(V_0^h) + dim(Q^h).$$

The choice of the pair spaces is very important, since this choice has to ensure the uniqueness of the solution of the system. The system has a unique solution if and only if V_0^h and Q^h fulfill the following inf-sup condition (known as Babuška–Brezzi condition) [9, 22]:

There exists a constant $\kappa > 0$ (independent of triangulation) such that

$$\inf_{q^h \in Q^h} \sup_{\mathbf{u}^h \in V_0^h} \frac{(\nabla \cdot \mathbf{u}^h, q^h)}{||\nabla \mathbf{u}^h|| ||q^h||} > \kappa. \tag{2.17}$$

Concrete pairs of spaces fulfilling this condition are introduced in Sec. 2.1.7.

One considers $\hat{K}$ as closed reference cell. The reference transformation from $\hat{K}$ onto a mesh cell K is denoted by F_K.

We denote by $Q_k(\hat{K})$ and $P_k(\hat{K})$ the following sets of polynomials on $\hat{K}$: and the global finite element spaces by

$$\begin{aligned} Q_k(\hat{K}) &:= \{\hat{q} = \sum_{i,j,l=0}^{k} a_{ijl} \hat{x}^i \hat{y}^j \hat{z}^l\}, \\ P_k(\hat{K}) &:= \{\hat{p} = \sum_{i,j,l=0}^{i+j+l \leqslant k} b_{ijl} \hat{x}^i \hat{y}^j \hat{z}^l\}. \end{aligned}$$

The space on the arbitrary mesh cell K is given by:

$$\begin{aligned} Q_k(K) &:= \{q = \hat{q} \circ F_K^{-1} \colon \hat{q} \in Q_k(\hat{K})\}, \\ P_k(K) &:= \{p = \hat{p} \circ F_K^{-1} \colon \hat{p} \in P_k(\hat{K})\}, \end{aligned}$$

and the global finite element spaces by

$$\begin{aligned} Q_k &:= \{v \in H^1(\Omega)\colon v|_K \in Q_k(K)\}, k \geqslant 1, \\ Q_0 &:= \{v \in L^2(\Omega)\colon v|_K \in Q_0(K)\}, \\ P_k^{disc} &:= \{v \in L^2(\Omega)\colon v|_K \in P_k(K)\}, k \geqslant 1. \end{aligned}$$

2.1.7 Numerical methods

There are a lot of proposals for stable pairs of finite element spaces, e.g., [13, 66]. We will use here an inf-sup stable pair of finite element spaces with discontinuous pressure, Q_2/P_1^{disc}, which is a popular choice [25]. In comparison with the inf-sup stable pair Q_2/P_1, the discontinuous pressure in Q_2/P_1^{disc} ensures a better local mass conservation. The efficiency of the numerical simulations depends on the solver which is chosen to solve the saddle point problem (2.16). Due to the finite element discretization, (2.16) possesses a sparse structure in the system matrices. Iterative solvers are often used for solving systems with large sparse system matrices. We use a solver based on coupled multigrid methods. The flexible GMRES (generalized minimal residual) method proposed by [70] with multiple discretization multigrid preconditioner has been proved to be an efficient solver for the forthcoming saddle point problem [34, 37] and the choice of inf-sup stable pair Q_2/P_1^{disc} of finite element spaces.

2.2 Scalar convection-diffusion equations

From a physical point of view, phenomena where species or energy (or other quantities) are transported inside a physical system, due to diffusion and convection can be modeled with convection-diffusion equations. From a mathematical point of view, these equations are partial differential equations and they can be derived in a straightforward way from the continuity equation. The time-dependent scalar convection-diffusion equation has the form:

$$\tilde{c}_t - \tilde{D}\Delta\tilde{c} + \tilde{\mathbf{u}} \cdot \nabla\tilde{c} = \tilde{\mathcal{F}} \text{ in } (0, \tilde{t}_{\text{end}}] \times \tilde{\Omega}, \tag{2.18}$$

where

- $\tilde{\Omega} \subset \mathbb{R}^3$ $[\text{m}^3]$ *is a bounded domain,*
- $\tilde{c}$ *denotes the unknown as for example temperature* $[K]$ *or concentration* $\left[\dfrac{\text{mol}}{\text{m}^3}\right]$,

- $\tilde{D}\ \left[\dfrac{\mathrm{m}^2}{\mathrm{s}}\right]$ *is the diffusion coefficient,*
- $\tilde{\mathbf{u}}\ \left[\dfrac{\mathrm{m}}{\mathrm{s}}\right]$ *is the convection field (velocity field) assumed to be divergence-free* $(\nabla \cdot \tilde{\mathbf{u}} = 0)$*,*
- $\tilde{\mathcal{F}}$ *describes the sources* $\left[\dfrac{K}{\mathrm{s}}\right]$ *or* $\left[\dfrac{\mathrm{mol}}{\mathrm{s\ m}^3}\right]$ *,*
- $\tilde{t}_{\mathrm{end}}$ [s] *is the final time.*

As the Re number for Navier–Stokes equation, so the Péclet number is a characteristic parameter for the convection-diffusion equations.

The Pe number is defined by

$$Pe = \frac{l_\infty \cdot u_\infty}{\tilde{D}}\,[\cdot]\,,$$

where l_∞ [m] *is a characteristic length scale of the problem and* $u_\infty\ \left[\dfrac{\mathrm{m}}{\mathrm{s}}\right]$ *is a characteristic scale of the convection field (velocity).*

Based on the Pe number, which represents the ratio of convective effects over diffusive effects, three regimes can be distinguished:

- $Pe \leqslant 1$ *the equation is diffusion-dominated,*
- $1 < Pe \leqslant 10$ *convection and diffusion are both important,*
- $Pe > 10$ *the equation is convection-dominated.*

2.2.1 The derivation

The general principle of the conservation laws states that the rate of change of a scalar quantity $\tilde{c}$ *in a control volume* CV*, as illustrated in Fig. 2.2, plus the flux of the quantity through the boundary of* CV *is equal to the rate of production or destruction of the quantity [76].*

This can be written as:

$$\frac{\partial}{\partial \tilde{t}} \int_{CV} \tilde{c}(\tilde{t}, \tilde{\mathbf{x}}) d\tilde{\mathbf{x}} + \int_{\partial CV} \mathcal{J}_{\tilde{c}}(\tilde{t}, \tilde{\mathbf{x}}) \cdot \mathbf{n}(s) ds = \int_{CV} \tilde{\mathcal{F}}(\tilde{t}, \tilde{\mathbf{x}}) d\tilde{\mathbf{x}}, \tag{2.19}$$

where $\mathcal{J}_{\tilde{c}}$ *is the total flux and* $\tilde{\mathcal{F}}$ *is a net volumetric source or sink of the quantity* $\tilde{c}$*.*

Using Gauss' divergence theorem for an arbitrary volume $CV \subset \tilde{\Omega}$*, one obtains:*

$$\int_{CV} \nabla \cdot \mathcal{J}_{\tilde{c}}(\tilde{t}, \tilde{\mathbf{x}}) d\tilde{\mathbf{x}} = \int_{\partial CV} \mathcal{J}_{\tilde{c}}(\tilde{t}, \tilde{\mathbf{x}}) \mathbf{n}(s) ds, \tag{2.20}$$

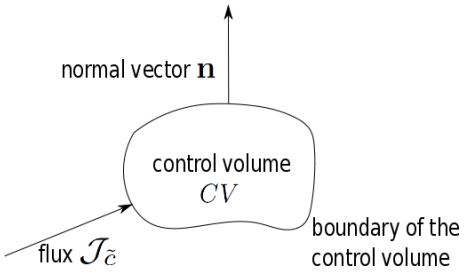

Figure 2.2: Control volume.

where $\mathbf{n}$ *is the outward pointing unit normal on* $s \in \partial CV$*. Inserting (2.20) in (2.19), and since* CV *was chosen as an arbitrary volume in* $\tilde{\Omega}$*, results in*

$$(\tilde{c}_t + \nabla \cdot \mathcal{J}_{\tilde{c}})(\tilde{t}, \tilde{\mathbf{x}}) = \tilde{\mathcal{F}}(\tilde{t}, \tilde{\mathbf{x}}) \ \forall \tilde{t} \in (0, \tilde{t}_{\text{end}}), \ \forall \tilde{\mathbf{x}} \in V. \tag{2.21}$$

There are two kinds of contributions in generating fluxes: a contribution due to the molecular agitation, which can be present even when the fluid stagnates and a contribution due to the convective transport of the fluid [32]. The diffusive contribution is usually described using the phenomenological Fick's first law, which assumes that the flux of the diffusing material in any part of the system is proportional to the local gradient

$$\mathcal{J}_{\tilde{c}}(\tilde{t}, \tilde{\mathbf{x}}) = -\tilde{D} \cdot \nabla \tilde{c}(\tilde{t}, \tilde{\mathbf{x}}).$$

When there is convection or flow, the convective flux is always present. It represents the amount of quantity $\tilde{c}$ *transported by the flow and it has the form:*

$$\mathcal{J}_{\tilde{c}}(\tilde{t}, \tilde{\mathbf{x}}) = \tilde{\mathbf{u}}\tilde{c}(\tilde{t}, \tilde{\mathbf{x}}).$$

Combining these two terms, the total flux becomes

$$\mathcal{J}_{\tilde{c}}(\tilde{t}, \tilde{\mathbf{x}}) = -\tilde{D} \cdot \nabla \tilde{c}(\tilde{t}, \tilde{\mathbf{x}}) + \tilde{\mathbf{u}}\tilde{c}(\tilde{t}, \tilde{\mathbf{x}}).$$

Substituting this expression into (2.21), one obtains

$$\tilde{c}_{\tilde{t}} + \nabla \cdot (-\tilde{D} \cdot \nabla \tilde{c} + \tilde{\mathbf{u}}\tilde{c}) = \tilde{\mathcal{F}}. \tag{2.22}$$

Applying the product rule in (2.22),

$$\nabla \cdot (-\tilde{D} \cdot \nabla \tilde{c} + \tilde{\mathbf{u}}\tilde{c}) = -\tilde{D}\Delta \tilde{c} + \nabla \cdot \tilde{\mathbf{u}}\tilde{c} + \tilde{\mathbf{u}} \cdot \nabla \tilde{c}$$

and using the fact that for incompressible fluids $\nabla \cdot \tilde{\mathbf{u}} = \mathbf{0}$*, one gets the equation (2.18).*

Considering the mass or energy balance for dispersed systems, the right-hand side in (2.18) may account for interchange mass (energy) transfer between the disperse and continuous phase due to thermodynamical phenomena, e.g nucleation or growth of the particles [64]

$$\tilde{\mathcal{F}} = -\rho^d \int_{\tilde{V}} \tilde{f}(\tilde{\mathbf{x}}, \tilde{L}, \tilde{t}) \tilde{G} \dot{\tilde{V}} d\tilde{V}, \tag{2.23}$$

with

- ρ^d *density of dispersed phase,*
- $\tilde{V}$ *volume of the particle,*
- $\tilde{f}(\tilde{\mathbf{x}}, \tilde{L}, \tilde{t})$ *particle size distribution,*
- $\tilde{G}$ *growth rate.*

2.2.2 The dimensionless form

The dimensionless form of the equation (2.18) is derived in the same way as the dimensionless form of the Navier–Stokes equations. Further, for the dimensionless convection-diffusion equation, the following dimensionless quantities are introduced:

$$c = \frac{\tilde{c}}{c_\infty},\ \mathbf{u} = \frac{\tilde{\mathbf{u}}}{u_\infty},\ t = \frac{\tilde{t}}{t_\infty}, \mathbf{x} = (x_1, x_2, x_3) = \left(\frac{\tilde{x_1}}{l_\infty}, \frac{\tilde{x_2}}{l_\infty}, \frac{\tilde{x_3}}{l_\infty} \right),\ t_\infty = \frac{l_\infty}{u_\infty}.$$

Inserting these quantities into (2.18)

$$\frac{c_\infty}{t_\infty} \frac{\partial c}{\partial t} - \tilde{D} \frac{c_\infty}{l_\infty^2} \Delta c + \frac{u_\infty c_\infty}{l_\infty} \mathbf{u} \cdot \nabla c \quad = \quad \tilde{\mathcal{F}}, \tag{2.24}$$

leads to a dimensionless convection-diffusion equation:

$$\frac{\partial c}{\partial t} - \frac{\tilde{D}}{l_\infty u_\infty} \Delta c + \mathbf{u} \cdot \nabla c = \mathcal{F} \text{ in } (0, t_{\text{end}}] \times \Omega,$$

where $\mathcal{F} := \dfrac{l_\infty}{c_\infty u_\infty} \tilde{\mathcal{F}}$ *and* $D := \dfrac{\tilde{D}}{l_\infty u_\infty}$.

2.2.3 Numerical methods

In the considered application, this type of equation was closed with appropriate initial and boundary conditions. Thus, the linear scalar convection-diffusion equation takes the form:

$$\begin{aligned} \frac{\partial c}{\partial t} - D\Delta c + \mathbf{u}\cdot\nabla c &= \mathcal{F} \text{ in } (0,t_{\text{end}}]\times\Omega, \\ D\nabla c\cdot\mathbf{n} &= 0 \text{ on } [0,t_{\text{end}}]\times\Gamma_N, \\ c &= c_D \text{ on } [0,t_{\text{end}}]\times\Gamma_D, \\ c(0,\cdot) &= c_0 \text{ in } \Omega. \end{aligned} \tag{2.25}$$

As the boundary condition, we have considered the Neumann boundary condition on Γ_N, the Dirichlet boundary condition on Γ_D ($\Gamma = \Gamma_N \cup \Gamma_D$, $\Gamma_N \cap \Gamma_D = \emptyset$), and as the initial condition c_0 in Ω. For the equation (2.25) the convection field might be time-dependent.

Apart from the spatial discretization, a temporal discretization is also needed. We are using here as time discretization a one-step Θ-scheme. Therefore, the first equation in (2.25) at the discrete time t_k takes the following form

$$\begin{aligned} & c_k + \theta_1\Delta t_k(-D\Delta c_k + \mathbf{u}_k\cdot\nabla c_k) \\ &= c_{k-1} - \theta_2\Delta t_k(-D\Delta c_{k-1} + \mathbf{u}_{k-1}\cdot\nabla c_{k-1}) \\ &\quad +\theta_3\Delta t_k\mathcal{F}_{k-1} + \theta_4\Delta t_k\mathcal{F}_k, \end{aligned} \tag{2.26}$$

with $\Delta t_k = t_k - t_{k-1}$, and the parameters θ_1, θ_2, θ_3, θ_4. The forward and backward Euler scheme and the Crank–Nicolson scheme are obtained by appropriate choices of these parameters:

- *forward Euler scheme $\theta_1 = \theta_4 = 0$, $\theta_2 = \theta_3 = 1$,*
- *backward Euler scheme $\theta_1 = \theta_4 = 1$, $\theta_2 = \theta_3 = 0$,*
- *Crank–Nicolson scheme $\theta_1 = \theta_2 = \theta_3 = \theta_4 = \frac{1}{2}$.*

Here, we use the Crank–Nicolson scheme for the time discretization [12].

Analogously to Navier–Stokes equations, in order to apply the Galerkin finite element method, the variational formulation formulation of (2.26) is derived.

The multiplication of (2.26) by a test function v and applying the integration by parts over the domain Ω leads to:

Find $c_k \in V_D$ such that

$$\begin{aligned}(c_k, v) + 0.5\Delta t_k((D\nabla u_k, \nabla v) + (\mathbf{u}_k \cdot \nabla c_k, v)) \\ = \quad (c_{k-1}, v) - 0.5\Delta t_k((D\nabla u_{k-1}, \nabla v) + (\mathbf{u}_{k-1} \cdot \nabla c_{k-1}, v)) \\ +0.5\Delta t_k(\mathcal{F}_{k-1}, v) + 0.5\Delta t_k(\mathcal{F}_k, v)\end{aligned} \tag{2.27}$$

for all $v \in V_0$, where

$$V_0 = \{c : c \in (H^1(\Omega))^3, c_{|\Gamma_D} = 0\},$$
$$V_D = \{c : c \in (H^1(\Omega))^3, c_{|\Gamma_D} = c_D\}.$$

For the simplicity of the representation it is assumed that c_D does not depend on time, so that the space V_D does not change in time.

In the usual way, the Galerkin finite element formulation is obtained by approximating the infinite dimensional spaces V_D and V_0 with finite element spaces V_D^h and V_0^h. So, the problem reads:

Find $c_k^h \in V_D^h$ such that

$$\begin{aligned}(c_k^h, v^h) + 0.5\Delta t_k((D\nabla c_k^h, \nabla v^h) + (\mathbf{u}_k \cdot \nabla u_k^h, v^h)) \\ = \quad (c_{k-1}^h, v^h) - 0.5\Delta t_k((D\nabla c_{k-1}^h, \nabla v^h) + (\mathbf{u}_{k-1}^h \cdot \nabla c_{k-1}^h, v^h)) \\ +0.5\Delta t_k(\mathcal{F}_{k-1}^h, v^h) + 0.5\Delta t_k(\mathcal{F}_k^h, v^h)\end{aligned} \tag{2.28}$$

for all $v^h \in V_0^h$.

In the case of convection- or reaction-dominated problems, the Galerkin finite element formulation is not stable [68]. The solution of (2.28) shows spurious oscillations in the whole domain. Comprehensive numerical studies of finite element methods for time-dependent convection-diffusion equations can be found in [39, 41, 42]. In these studies, a linear finite element flux-corrected transport (FEM–FCT) scheme turned out to combine good accuracy and high efficiency. We are using the linear FEM–FCT for solving the scalar convection-diffusion equations in three-dimensional domain. A short description of the method is given below.

The FEM–FCT methods were originally developed for transport equations [46, 47, 48, 49], i.e., for a particular case of (2.18) with $D = \mathcal{F} = 0$. In contrast to most other stabilized finite element methods, this method works on an algebraic level and does not modify the bilinear form which defines the finite

element method. This method begins with the algebraic equation corresponding to the Galerkin finite element method:

$$(\mathbf{M}_C + 0.5\Delta t\mathbf{E})c_k = (\mathbf{M}_C - 0.5\Delta t\mathbf{E})c_{k-1} + 0.5\Delta t\mathcal{F}_{k-1} + 0.5\Delta t\mathcal{F}_k, \quad (2.29)$$

where

- $(\mathbf{M}_C)_{ij} = (\varphi_j, \varphi_i)$ *is the consistent mass matrix and* $\{\varphi_i\}$ *is a basis of the finite element space,*
- $(\mathbf{E}_k)_{ij} = (e_{ij})$ *is the stiffness matrix containing the sum of diffusion, convection and reaction,*
- $\mathcal{F}_k$ *is the right-hand side at time* t_k*.*

An essential and first goal of the FEM–FCT schemes is the positivity-preserving of the solution of (2.25). Let $D = \mathcal{F} = 0$*,* $\Gamma_D = \Gamma$*, and* $c_D = 0$ *which results in:*

$$c_0(\mathbf{x}) \geq 0,\ \forall \mathbf{x} \in \Omega \ \Rightarrow\ c(t, \mathbf{x}) \geq 0,\ \forall \mathbf{x} \in \Omega,\ \forall t \geq 0.$$

This property guarantees that the temperature or the concentration remains non-negative. The numerical solution of (2.29) might be corrupted by spurious oscillations or numerical instabilities.

If the maximum principle holds for the continuous equation (2.25), then this principle has to be inherited from the discrete equation. This is given if the system matrix of the discrete equation is an M–matrix. In other words, the FEM–FCT starts by modifying the equation (2.29) such that a stable but low order scheme is represented. For this, it is defined:

$$\mathbf{L} := \mathbf{E} + \mathbf{D},$$

with

$$\mathbf{D} := (d_{ij}),\ d_{ij} = -\max\{0, e_{ij}, e_{ji}\}\ for\ i \neq j,\ d_{ii} = -\sum_{j=1, j\neq i}^{N} d_{ij},$$

$$\mathbf{M}_L := diag(m_i),\ m_i = \sum_{j=1}^{N} m_{ij},$$

where N *is the number of degrees of freedom and* M_L *is called the lumped mass matrix. It holds that*

- *the row and column sums of* $\mathbf{D}$ *are zero,*

- **L** *does not posses positive off-diagonal entries.*

Thus, the low order scheme reads:

$$(\mathbf{M}_L + 0.5\Delta t\mathbf{L})c_k = (\mathbf{M}_L - 0.5\Delta t\mathbf{L})c_{k-1} + 0.5\Delta t\mathcal{F}_{k-1} + 0.5\Delta t\mathcal{F}_k. \quad (2.30)$$

The second aim of the FEM–FCT is to modify the right-hand side of (2.30) in such a way that diffusion is removed where it is not needed but spurious oscillations are still suppressed

$$\begin{aligned}(\mathbf{M}_L + 0.5\Delta t\mathbf{L})c_k &= (\mathbf{M}_L - 0.5\Delta t\mathbf{L})c_{k-1} + 0.5\Delta t\mathcal{F}_{k-1} + 0.5\Delta t\mathcal{F}_k \\ &\quad +\mathcal{F}^*(c_k, c_{k-1}),\end{aligned} \quad (2.31)$$

where the ansatz for the vector $\mathcal{F}^*(c_k, c_{k-1})$ uses the residual of (2.30) and (2.31)

$$\begin{aligned}r &= (\mathbf{M}_L + 0.5\Delta t\mathbf{L} - (\mathbf{M}_C + 0.5\Delta t\mathbf{E}))c_k \\ &\quad -(\mathbf{M}_L - 0.5\Delta t\mathbf{L} - (\mathbf{M}_C - 0.5\Delta t\mathbf{E}))c_{k-1} \\ &= (\mathbf{M}_L - \mathbf{M}_C)(c_k - c_{k-1}) + \Delta t_k\mathbf{D}(0.5c_k - 0.5c_{k-1}).\end{aligned} \quad (2.32)$$

The residual vector has to be weighted adequately, therefore, for the definition of the weights, the residual is decomposed into fluxes r_{ij}, $i, j = 1, \cdots, N$, in the following way

$$\begin{aligned}r_i &= \sum_{j=1}^{N} r_{ij} \\ &= \sum_{j=1}^{N}[m_{ij}(c_{k,i} - c_{k,j}) - m_{ij}(c_{k-1,i} - c_{k-1,j}) \\ &\quad -0.5\Delta t_k d_{ij}(c_{k,i} - c_{k,j}) - 0.5\Delta t_k d_{ij}(c_{k-1,i} - c_{k-1,j})].\end{aligned}$$

Thus,

$$\begin{aligned}r_{ij} &= m_{ij}(c_{k,i} - c_{k-1,i}) - m_{ij}(c_{k,j} - c_{k-1,j}) \\ &\quad -0.5\Delta t_k d_{ij}(c_{k,i} + c_{k-1,i}) - 0.5\Delta t_k d_{ij}(c_{k,j} - c_{k-1,j}).\end{aligned} \quad (2.33)$$

The ansatz for the correction term becomes

$$\mathcal{F}_i^*(c_k, c_{k-1}) = \sum_{j=1}^{N} \alpha_{ij} r_{ij},$$

with the weights $\alpha_{ij} \in [0,1]$ *and* $i = 1, \cdots, N$.

In the case that the weights are dependent on the residual vector $\mathcal{F}^*(c_k, c_{k-1})$, *one gets the nonlinear case of the FEM–FCT scheme [47, 48]. On the other hand, if all weights are equal to* 1, *the Galerkin finite element method is recovered. A linear FEM–FCT method is used here. The motivation of choosing this approach is based on the results of [39, 41, 42], which showed a good ratio of accuracy and efficiency. The linear FEM–FCT method [46] has as a starting point the following idea.*

In the equation (2.33), c_k *will be replaced by an approximation which can be computed with an explicit scheme. For this, an intermediate value will be defined as follows:*

$$c_{k-1/2} := \frac{c_k + c_{k-1}}{2}.$$

Thus, one obtains:

$$\begin{aligned} r_{ij} &= 2m_{ij}(c_{k-1/2,i} - c_{k-1,i}) - 2m_{ij}(c_{k-1/2,j} - c_{k-1,j}) \\ &- \Delta t_k d_{ij}(c_{k-1/2,i} - c_{k-1/2,j}). \end{aligned} \tag{2.34}$$

An approximation of $c_{k-1/2}$ *can be obtained with a forward Euler scheme applied to the equation corresponding to the low order scheme (2.30), with the time step* $\Delta t_k/2$. *It follows:*

$$\bar{c} = c_{k-1} - 0.5\Delta t_k M_L^{-1}(Lc_{k-1} - \mathcal{F}_{k-1}).$$

Inserting this approximation into (2.34) the numerical fluxes of the linear FEM–FCT method are given as:

$$r_{ij} = \Delta t_k[m_{ij}(c_{k-1/2,i} - c_{k-1/2,j}) - d_{ij}(\bar{c}_i - \bar{c}_j)],$$

where

$$\begin{aligned} c_{k-1/2,i} : &= (\mathbf{M}_L^{-1}(\mathcal{F}_{k-1} - \mathbf{L}c_{k-1}))_i, \\ \bar{c}_i : &= c_{k-1} + 0.5\Delta c_{k-1/2,i}. \end{aligned}$$

Regarding the computation of the weights [41], Zalesak's algorithm was used [77]. The motivation of choosing this algorithm was discussed in [47]. A short description of the algorithm is given here:

- *Compute the sums of the negative/non-negative antidiffusive fluxes in the node i*

$$P_i^+ = \sum_{j=1, j\neq i}^{N} \max\{0, r_{ij}\},$$

$$P_i^- = \sum_{j=1, j\neq i}^{N} \min\{0, r_{ij}\}.$$

- *Compute the distance to a local extremum of the auxiliary solution* $\tilde{c}$

$$Q_i^+ = \max\left\{0, \max_{j=1,\cdots,N, j\neq i}(\bar{c}_j - \bar{c}_i)\right\},$$

$$Q_i^- = \min\left\{0, \min_{j=1,\cdots,N, j\neq i}(\bar{c}_j - \bar{c}_i)\right\}.$$

- *Compute the nodal correction factors*

$$R_i^+ = \min\left\{1, \frac{m_i Q_i^+}{P_i^+}\right\},$$

$$R_i^- = \min\left\{1, \frac{m_i Q_i^-}{P_i^-}\right\}.$$

- *Compute the weights*

$$\alpha_{ij} = \begin{cases} \min\{R_i^+, R_j^-\} & , r_{ij} > 0, \\ \min\{R_i^-, R_j^+\} & , r_{ij} < 0. \end{cases}$$

The auxiliary solution $\tilde{c}$ *is used to guarantee the fulfillment of the maximum principle [46]. Since* $\tilde{c}$ *is computed with an explicit method, a CFL–like condition for FEM–FCT scheme has to be satisfied. This condition is [46, 47]*

$$\Delta t_k < 2 \min_i \frac{m_i}{l_{ii}}.$$

2.3 Higher dimensional integro-partial differential equation

Higher dimensional integro-partial differential equations are used for modeling a variety of particulate systems as well as various stochastic phenomena in science and engineering. These processes are characterized by the presence of a dispersed phase system [21]. The dispersed phase is surrounded by the

continuous phase	dispersed phase	example
gas	liquid	aerosol
gas	solid	spray granulation
liquid	gas	absorption
liquid	liquid	extraction
liquid	solid	crystallization

Table 2.1: Classification of the dispersed two-phase systems.

continuous one and forms the so-called population of particles. A schematic classification of dispersed two-phase systems is given in Table 2.1.

Moreover, each particle interacts with the surrounding continuous phase by exchanging heat, mass, and momentum which leads to different population phenomena occurring in the dispersed phase system. These phenomena can be classified into two groups. On the one hand, there are the phenomena due to the heat and mass transfer between the continuous and dispersed phase (e.g., nucleation, growth); on the other hand, there are the phenomena due to the fluid dynamic processes and momentum transfer between the two phases (e.g., breakage, aggregation). The equations describing these type of systems belong to the class of transport equations, with the special feature that they describe the evolution of a particle size distribution (PSD) in high-dimensional spaces. They are known among in the engineering community as population balance equations.

The mathematical modeling of population balance equations requires not only the external coordinates*, describing the characteristics of the continuous phase, but also the the so-called* internal coordinates*, representing the characteristics of the dispersed phase [33]. External coordinates indicate the physical location of the particle,*

$$\tilde{\mathbf{x}} = (\tilde{x}_1, \tilde{x}_2, \tilde{x}_3),$$

and internal coordinates indicate the internal characteristic of the particle (e.g., diameter, volume*),*

$$\tilde{L} = (\tilde{L}_1, \cdots, \tilde{L}_n).$$

Further, the internal coordinates could refer to the particles' dimensions along the characteristic axes, and with it, a prototype of this kind of equations is given by:

$$\tilde{f}_t + \tilde{\mathbf{u}}_{\tilde{L}} \cdot \nabla_{\tilde{L}} \tilde{f} + \tilde{\mathbf{u}}_{\tilde{\mathbf{x}}} \cdot \nabla_{\tilde{\mathbf{x}}} \tilde{f} = \tilde{H} \ \textit{in}\ (0, \tilde{t}_{\text{end}}] \times \tilde{\Omega}_{\tilde{\mathbf{x}}} \times \tilde{\Omega}_{\tilde{L}}, \tag{2.35}$$

where

- $\tilde{\Omega}_{\tilde{\mathbf{x}}} \times \tilde{\Omega}_{\tilde{L}} \subset \mathbb{R}^3 \times \mathbb{R}^n \ \left[\mathrm{m}^3 \cdot \mathrm{m}^n\right]$ *is the product domain of external and internal coordinates with* $n \in \{1, 2\}$,
- $\tilde{f} \ \left[\dfrac{1}{\mathrm{m}^3 \ \mathrm{m}^n}\right]$ *is the particles size distribution,*
- $\tilde{\mathbf{u}}_{\tilde{L}} \ \left[\dfrac{\mathrm{m}}{\mathrm{s}}\right]$ *is the convective field with respect to internal coordinates,*
- $\tilde{\mathbf{u}}_{\tilde{\mathbf{x}}} \ \left[\dfrac{\mathrm{m}}{\mathrm{s}}\right]$ *is the convective field with respect to external coordinates,*
- $\tilde{H} \ \left[\dfrac{1}{\mathrm{s} \ \mathrm{m}^3 \ \mathrm{m}^n}\right]$ *is the source term,*
- $\tilde{t}_{\mathrm{end}} \ [\mathrm{s}]$ *is the final time.*

2.3.1 The derivation

From a mathematical point of view, the dispersed phase is represented with the help of a number density function, denoted by $\tilde{f}$*, which describes the expected number of particles that are located in a certain domain of the particle state space,* $\tilde{\Omega}_{\tilde{\mathbf{x}}} \times \tilde{\Omega}_{\tilde{L}}$*, and a certain time* $\tilde{t}$ *[63].*
Let $(\tilde{\mathbf{x}}, \tilde{L})$ *be a set of external and internal coordinates in* $\tilde{\Omega}_{\tilde{\mathbf{x}}} \times \tilde{\Omega}_{\tilde{L}}$*. Both span the space particle state space, so that any particle can be represented uniquely by a point in this space. Therefore,* $\tilde{f}$ *depends on the external coordinates, internal coordinates and time* $\tilde{t}$

$$\tilde{f} = \tilde{f}(\tilde{t}, \tilde{\mathbf{x}}, \tilde{L}).$$

The number density function $\tilde{f}$ *is assumed to be sufficiently smooth to allow differentiation with respect to any of its arguments as many time as may become necessary. The total number of the particles in the entire system at the time* $\tilde{t}$ *is given by [63]*

$$N(t) = \int_{\tilde{\Omega}_{\tilde{\mathbf{x}}}} \int_{\tilde{\Omega}_{\tilde{L}}} \tilde{f}(\tilde{t}, \tilde{\mathbf{x}}, \tilde{L}) dV_{\tilde{\mathbf{x}}} dV_{\tilde{L}}, \tag{2.36}$$

where $dV_{\tilde{\mathbf{x}}}$ *and* $dV_{\tilde{L}}$ *are infinitesimal volume measures in the space of external and internal coordinates,* $\tilde{\Omega}_{\tilde{\mathbf{x}}} \times \tilde{\Omega}_{\tilde{L}}$*.*

We will consider only such systems, in which the particles change their state deterministically. A particle space continuum was introduced in [62] that pervades the particle state space. It is assumed that the particles are embedded in this continuum. Further, only such systems will be taken into account where

the continuum phase coincides with the fluid phase, in other words, there is no relative motion between the particles and the continuous phase.

The general form of the population balance equation can be derived in the same way as for convection-diffusion equations. Applying the general principle of the conservation [76], it follows,

$$\frac{d}{d\tilde{t}}\int_{CV}\tilde{f}dCV+\int_{\partial CV}\mathcal{J}_{\tilde{f}}\cdot\mathbf{n}ds=\int_{CV}\tilde{H}dCV, \tag{2.37}$$

which states that the rate of change of the scalar quantity $\tilde{f}$ in a control volume CV plus the flux of the quantity $\mathcal{J}_{\tilde{f}}$ through the boundary of CV is equal to the rate of change of production or destruction of the quantity.

Let $CV=V_{\tilde{\mathbf{x}}}\times V_{\tilde{L}}$ be an arbitrary fixed control volume in the particle state space $\tilde{\Omega}_{\tilde{\mathbf{x}}}\times\tilde{\Omega}_{\tilde{L}}$. Thus, the equation (2.37) takes the form:

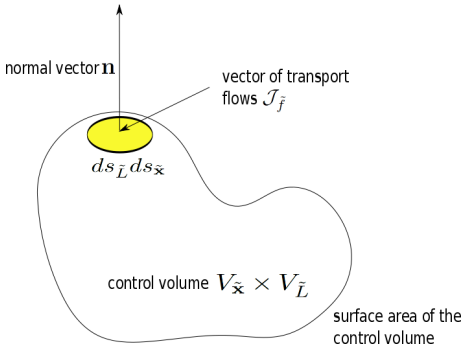

Figure 2.3: Control volume.

$$\frac{d}{d\tilde{t}}\int_{V_{\tilde{\mathbf{x}}}}\int_{V_{\tilde{L}}}\tilde{f}(\tilde{\mathbf{x}},\tilde{L},\tilde{t})dV_{\tilde{L}}dV_{\tilde{\mathbf{x}}}+\int_{\partial V_{\tilde{\mathbf{x}}}}\int_{\partial V_{\tilde{L}}}\mathcal{J}_{\tilde{f}}(\tilde{\mathbf{x}},\tilde{L},\tilde{t})\cdot\mathbf{n}ds_{\tilde{L}}ds_{\tilde{\mathbf{x}}}=\int_{V_{\tilde{\mathbf{x}}}}\int_{V_{\tilde{L}}}\tilde{H}dV_{\tilde{L}}dV_{\tilde{\mathbf{x}}}.$$

Using Gauss' divergence theorem for an arbitrary volume CV, one obtains:

$$\int_{\partial V_{\tilde{\mathbf{x}}}}\int_{\partial V_{\tilde{L}}}\mathcal{J}_{\tilde{f}}(\tilde{\mathbf{x}},\tilde{L},\tilde{t})\cdot\mathbf{n}ds_{\tilde{L}}ds_{\tilde{\mathbf{x}}}=\int_{V_{\tilde{\mathbf{x}}}}\int_{V_{\tilde{L}}}\nabla_{\tilde{\mathbf{x}},\tilde{L}}\cdot\mathcal{J}_{\tilde{f}}(\tilde{\mathbf{x}},\tilde{L},\tilde{t})d\tilde{L}d\tilde{\mathbf{x}}.$$

Since the choice of V is arbitrary, this equation results in

$$\tilde{f}_{\tilde{t}}(\tilde{\mathbf{x}},\tilde{L},\tilde{t})+\nabla_{\tilde{\mathbf{x}},\tilde{L}}\cdot\mathcal{J}_{\tilde{f}}(\tilde{\mathbf{x}},\tilde{L},\tilde{t})=\tilde{H}, \tag{2.38}$$

where $\nabla_{\tilde{\mathbf{x}},\tilde{L}}$ denotes the gradient with respect to the external and internal coordinates.

For the following formulation of a general population balance [21], the transport of the total flux $\nabla_{\tilde{\mathbf{x}},\tilde{L}} \cdot \mathcal{J}_{\tilde{f}}(\tilde{\mathbf{x}},\tilde{L},\tilde{t})$ is split into a transport flux with respect to the external coordinates $\nabla_{\tilde{\mathbf{x}}} \cdot \mathcal{J}_{\tilde{f},\tilde{\mathbf{x}}}(\tilde{\mathbf{x}},\tilde{L},\tilde{t})$ and one with respect to internal coordinates $\nabla_{\tilde{L}} \cdot \mathcal{J}_{\tilde{f},\tilde{L}}(\tilde{\mathbf{x}},\tilde{L},\tilde{t})$. It follows:

$$\tilde{f}_{\tilde{t}}(\tilde{\mathbf{x}},\tilde{L},\tilde{t}) + \nabla_{\tilde{\mathbf{x}}} \cdot \mathcal{J}_{\tilde{f},\tilde{\mathbf{x}}}(\tilde{\mathbf{x}},\tilde{L},\tilde{t}) + \nabla_{\tilde{L}} \cdot \mathcal{J}_{\tilde{f},\tilde{L}}(\tilde{\mathbf{x}},\tilde{L},\tilde{t}) = \tilde{H},$$

with

$$\nabla_{\tilde{\mathbf{x}}} = \nabla = \begin{pmatrix} \dfrac{\partial}{\partial \tilde{x}_1} \\ \dfrac{\partial}{\partial \tilde{x}_2} \\ \dfrac{\partial}{\partial \tilde{x}_3} \end{pmatrix}, \nabla_{\tilde{L}} = \begin{pmatrix} \dfrac{\partial}{\partial \tilde{\tilde{L}}_1} \\ \cdots \\ \dfrac{\partial}{\partial \tilde{\tilde{L}}_n} \end{pmatrix}.$$

Furthermore, the transport flux, similar to the flux of non-dispersed phase, can be divided into a diffusive $\mathcal{J}_{\tilde{f}}^{D}$ and a convective $\tilde{\mathbf{u}}\tilde{f}$ part:

- $\mathcal{J}_{\tilde{f},\tilde{\mathbf{x}}} = \mathcal{J}_{\tilde{f},\tilde{\mathbf{x}}}^{D} + \tilde{\mathbf{u}}_{\tilde{\mathbf{x}}}\tilde{f}$,
- $\mathcal{J}_{\tilde{f},\tilde{L}} = \mathcal{J}_{\tilde{f},\tilde{L}}^{D} + \tilde{\mathbf{u}}_{\tilde{L}}\tilde{f}$.

The diffusive part of the transport flux in the physical space $\mathcal{J}_{\tilde{f},\tilde{\mathbf{x}}}^{D}$ accounts for the thermal or Brownian motion of the particles. Assuming that there is no interaction between the particles, the diffusive part $\mathcal{J}_{\tilde{\mathbf{x}}}^{D}$ can be described with Fick's first law

$$\mathcal{J}_{\tilde{f},\tilde{\mathbf{x}}}^{D} = -D \cdot \nabla_{\tilde{\mathbf{x}}}\tilde{f}.$$

The convective part of the transport flux in the physical space $\tilde{\mathbf{u}}_{\tilde{\mathbf{x}}}\tilde{f}$ describes the deterministic moving of the particles resulting from the forces of flowing continuum exercised on the particles.

Based on the assumption that the particles are embedded in the continuum, the velocity $\tilde{\mathbf{u}}_{\tilde{\mathbf{x}}}$ can be approximated by the velocity $\tilde{\mathbf{u}}$ of the surrounding continuous phase:

$$\tilde{\mathbf{u}}_{\tilde{\mathbf{x}}} \approx \tilde{\mathbf{u}}. \tag{2.39}$$

The diffusive part of the transport flux in the property space $\tilde{\mathbf{u}}_{\tilde{L},\tilde{\mathbf{x}}}$ accounts for the stochastic variation of the growth rate describing the deterministic average. A so-called growth rate dispersion introduced by [65] is used to describe the fact that the particles of the same size grow at different rates. This effect is modeled

with Fick's first law, in the same way as for the diffusive part in the physical space $\mathcal{J}^D_{\tilde{\mathbf{x}}}$

$$\mathcal{J}^D_{\tilde{f},\tilde{L}} = -D \cdot \nabla_{\tilde{L}} \tilde{f}.$$

For the considered application an exact information about the diffusion part is not known. It is only known that the diffusion is very small and the convection is much larger than that. Because of this aspect, the diffusive parts of the particles transported through the physical and property space are neglected.

The convective part of the transport flux property space $\tilde{\mathbf{u}}_{\tilde{L}} \tilde{f}$ *describes the rate of change of particle properties. Assuming* $\tilde{L}$ *is a characteristic length of the particle, e.g., diameter, then the corresponding velocity* $\tilde{\mathbf{u}}_{\tilde{L}}$ *is the growth rate of the particles.*

The starting point for the derivation of velocity in the property space is the energy and material exchange between the continuous and dispersed phase. In the models of the considered experiments, the growth rate does not depend on the length of the particles here. Thus, one gets

$$\tilde{\mathbf{u}}_{\tilde{L}}(\tilde{L}, \tilde{\mathbf{x}}, \tilde{\mathbf{y}}) = \frac{d\tilde{L}}{d\tilde{t}} = \tilde{G}(\tilde{\mathbf{y}}), \tag{2.40}$$

where the vector $\tilde{\mathbf{y}} = \tilde{\mathbf{y}}(\tilde{\mathbf{x}}, \tilde{t})$ *describes the state of the continuous phase, e.g., temperature, concentration. Moreover, assuming* $\tilde{L} = (\tilde{L}_1, \tilde{L}_2)$ *the characteristic dimensions of the anizotropic particles, e.g., length and width, then the corresponding growth rate of the particles with respect to the main axis is given as:*

$$\begin{pmatrix} \tilde{G}_1(\tilde{\mathbf{y}}) \\ \tilde{G}_2(\tilde{\mathbf{y}}) \end{pmatrix} = \begin{pmatrix} \tilde{\mathbf{u}}_{\tilde{L}_1}(\tilde{L}_1, \tilde{\mathbf{x}}, \tilde{\mathbf{y}}) \\ \tilde{\mathbf{u}}_{\tilde{L}_2}(\tilde{L}_2, \tilde{\mathbf{x}}, \tilde{\mathbf{y}}) \end{pmatrix}$$

where

$$\tilde{\mathbf{u}}_{\tilde{L}_1}(\tilde{L}_1, \tilde{\mathbf{x}}, \tilde{\mathbf{y}}) = \frac{d\tilde{L}_1}{d\tilde{t}} = \tilde{G}_1(\tilde{\mathbf{y}}), \tag{2.41}$$

$$\tilde{\mathbf{u}}_{\tilde{L}_2}(\tilde{L}_2, \tilde{\mathbf{x}}, \tilde{\mathbf{y}}) = \frac{d\tilde{L}_2}{d\tilde{t}} = \tilde{G}_2(\tilde{\mathbf{y}}). \tag{2.42}$$

Then the equation (2.38) becomes

$$\tilde{f}_{\tilde{t}} + \nabla_{\tilde{L}} \cdot (\tilde{\mathbf{u}}_{\tilde{L}} \tilde{f}) + \nabla_{\tilde{\mathbf{x}}} \cdot (\tilde{\mathbf{u}}_{\tilde{\mathbf{x}}} \tilde{f}) = \tilde{H}. \tag{2.43}$$

Using (2.39), (2.40), the fact that for incompressible fluids $\nabla_{\tilde{\mathbf{x}}} \cdot \tilde{\mathbf{u}} = 0$ *and the product rule for*

$$\begin{aligned} \nabla_{\tilde{\mathbf{x}}} \cdot (\tilde{\mathbf{u}}_{\tilde{\mathbf{x}}} \tilde{f}) &= (\tilde{\mathbf{u}}_{\tilde{\mathbf{x}}} \cdot \nabla_{\tilde{\mathbf{x}}}) \tilde{f} + \tilde{f} (\nabla_{\tilde{\mathbf{x}}} \cdot \tilde{\mathbf{u}}_{\tilde{\mathbf{x}}}) \\ &= \tilde{\mathbf{u}} \cdot \nabla \tilde{f} \end{aligned}$$

and

$$\begin{aligned} \nabla_{\tilde{L}} \cdot (\tilde{\mathbf{u}}_{\tilde{L}} \tilde{f}) &= \nabla_{\tilde{L}} \cdot (\tilde{G}(\tilde{\mathbf{y}}) \tilde{f}) \\ &= (\tilde{G}(\tilde{\mathbf{y}}) \cdot \nabla_{\tilde{L}}) \tilde{f} + \tilde{f} (\nabla_{\tilde{L}} \cdot \tilde{G}(\tilde{\mathbf{y}})) \\ &= \tilde{G}(\tilde{\mathbf{y}}) \cdot \nabla_{\tilde{L}} \tilde{f}. \end{aligned}$$

equation (2.43) results in:

- *uni-variate population balance*

$$\tilde{f}_{\tilde{t}} + \tilde{G}(\tilde{\mathbf{y}}) \frac{\partial \tilde{f}}{\partial \tilde{L}} + \tilde{\mathbf{u}}_{\tilde{\mathbf{x}}} \cdot \nabla_{\tilde{\mathbf{x}}} \tilde{f} = \tilde{H}, \tag{2.44}$$

- *bi-variate population balance*

$$\tilde{f}_{\tilde{t}} + \tilde{G}_1(\tilde{\mathbf{y}}) \frac{\partial \tilde{f}}{\partial \tilde{L}_1} + \tilde{G}_2(\tilde{\mathbf{y}}) \frac{\partial \tilde{f}}{\partial \tilde{L}_2} + \tilde{\mathbf{u}}_{\tilde{\mathbf{x}}} \cdot \nabla_{\tilde{\mathbf{x}}} \tilde{f} = \tilde{H}. \tag{2.45}$$

The right-hand side term $\tilde{H}$ *of (2.44) and (2.45) accounts for different physical phenomena, e.g nucleation, aggregation and breakage. As shown in [1], it is known that breakage occurs for turbulent flow whereas aggregation takes place in less turbulent regions. Here, the experiments which are the basis of the simulations lead to steady-state flows. Therefore, it is not necessary to include the breakage phenomena.*

In the case of uni-variate modeling, $\tilde{H}$ *describes only the aggregation since the considered experiment of urea synthesis is aggregation-driven [6]*

$$\tilde{H} = \tilde{H}_{+,\mathrm{agg}} + \tilde{H}_{-,\mathrm{agg}}.$$

In the bi-variate modeling the crystallization of potassium dihydrogen phosphate, $\tilde{H}$ *accounts only for nucleation since up to now there are no available aggregation kernels in the literature*

$$\tilde{H} = \tilde{H}_{\mathrm{nuc}}.$$

2.3.2 Population dynamical phenomena

Considering a dispersed two-phase system, the so-called population of particles is embedded in the continuous phase. The interaction between the two phases is done by exchanging heat, mass and momentum. This leads to different population dynamical phenomena occurring in the dispersed phase system. For deriving population balance equations, one has to take into account these phenomena which can be divided into two groups:

- *phenomena due to the heat and mass transfer between continuous and dispersed phase, e.g., nucleation, growth of the particles, see Sec. 2.3.3 and Sec. 2.3.4*
- *phenomena due to the fluid dynamic processes and momentum transfer between the two phases, e.g., aggregation and breakage, see Sec. 2.3.5 (breakage will be neglected here).*

2.3.3 Nucleation

The formation of new particles is called nucleation. This phenomena can occur by several mechanisms: homogeneous, heterogeneous, and secondary nucleation [60, 64]. Secondary nucleation accounts for producing of nuclei in the vicinity of crystals present in a supersaturated system. In the considered applications, only the secondary nucleation is taken into account.

In the context of the population balance equation, nucleation can be modeled using a source term [21, 33] or via an appropriate specification of the boundary condition [10, 64].

Modeling nucleation via a source term. *From a mathematical point of view, on the one hand, the formation of new particles can be described with a birth rate, $\tilde{B}_{\mathrm{nuc}}(\tilde{L}, y(\tilde{\mathbf{x}}, \tilde{t}))[1/(\mathrm{m}^3\mathrm{s})]$, which depends on the state of the continuous phase, e.g., temperature, concentration. The birth rate accounts for the number of particles that are formed per unit time and per volume element of the geometric space. On the other hand, the newly formed particles can take different values in the internal coordinate, so the size of newly generated nuclei can be described by a probability density distribution which satisfies*

$$\int_{\tilde{V}} \tilde{f}_{\mathrm{nuc}}(\tilde{L}) d\tilde{V} = 1. \tag{2.46}$$

For the particular case, for which the particles are assumed to nucleate at the same size considering bi-variate population balances, e.g., $(\tilde{L}_{1,\mathrm{nuc}}, \tilde{L}_{2,\mathrm{nuc}})$, the

Dirac delta distribution, $\delta\left(\tilde{L}-(\tilde{L}_{1,\mathrm{nuc}},\tilde{L}_{2,\mathrm{nuc}})\right)\,[1/(\mathrm{m}^2)]$*, can be considered instead of the probability density distribution:*

$$\delta\left(\tilde{L}-(\tilde{L}_{1,\mathrm{nuc}},\tilde{L}_{2,\mathrm{nuc}})\right)=\begin{cases}\infty, & \text{if } \tilde{L}=(\tilde{L}_{1,\mathrm{nuc}},\tilde{L}_{2,\mathrm{nuc}}),\\ 0, & \text{else},\end{cases} \tag{2.47}$$

with

$$\int_{\tilde{V}}\delta\left(\tilde{L}-(\tilde{L}_{1,\mathrm{nuc}},\tilde{L}_{\mathrm{nuc}})\right)dV=\int_{V}\delta\left(\tilde{L}_1-\tilde{L}_{1,\mathrm{nuc}}\right)\delta\left(\tilde{L}_2-\tilde{L}_{2,\mathrm{nuc}}\right)d\tilde{V}=1. \tag{2.48}$$

Then, the source term in the population balance equation is modeled by

$$\tilde{H}_{\mathrm{nuc}}(\tilde{L},\tilde{t})=\tilde{B}_{\mathrm{nuc}}\delta\left(\tilde{L}_1-\tilde{L}_{1,\mathrm{nuc}}\right)\delta\left(\tilde{L}_2-\tilde{L}_{2,\mathrm{nuc}}\right). \tag{2.49}$$

Modeling nucleation via a boundary condition. *Neglecting the size distribution of generated nuclei, one can also assume, for uni-variate population balances, a source at the smallest boundary of the particle size domain* $\tilde{L}=\tilde{L}_{\mathrm{nuc}}$ *given as [10]*

$$\tilde{f}(\tilde{t},\tilde{\mathbf{x}},\tilde{L})=\begin{cases}\dfrac{\tilde{B}_{\mathrm{nuc}}}{\tilde{G}}, & \text{if } \tilde{L}=\tilde{L}_{\mathrm{nuc}},\\ 0, & \text{else},\end{cases} \tag{2.50}$$

which states that there is a dynamic equilibrium of particles formed at the smallest boundary at a nucleation rate B_{nuc} *and the growth of these particles with the linear growth rate* $\tilde{G}$ $[m/s]$*, see Sec. 2.3.4.*

For bi-variate population balances, the modeling using a boundary condition does not satisfy the dimension units for particle size distributions.

From the kinetic theory [60, 64] it is known that frequently used expressions for the nucleation rate are given in terms of supersaturation and total volume of the crystalline phase as follows

$$\tilde{B}_{\mathrm{nuc}}=k_b\sigma_{\mathrm{rel}}^{b}\tilde{V}_{\mathrm{cryst}}, \tag{2.51}$$

where

- k_b $\left[1/(\mathrm{m}^3\mathrm{s})\right]$ *is the kinematic parameter for nucleation correlated with the experimental data,*
- b $[\cdot]$ *is the kinetics order of nucleation,*
- σ_{rel} $[\cdot]$ *is the relative supersaturation,*
- $\tilde{V}_{\mathrm{cryst}}$ $\left[\mathrm{m}^3\right]$ *is the total volume of the crystalline phase.*

The relative supersaturation is given by

$$\sigma_{\mathrm{rel}} = \frac{\tilde{c} - \tilde{c}_{\mathrm{sat}}}{\tilde{c}_{\mathrm{sat}}}, \tag{2.52}$$

where

- c *is the solution's concentration,*
- c_{sat} *is the equilibrium saturation concentration in dependency on temperature.*

The total volume of the crystalline phase is equivalent to the third order moment of the density distribution $\tilde{f}(\tilde{t}, \tilde{\mathbf{x}}, \tilde{L})$ *and is given by*

$$\tilde{V}_{\mathrm{cryst}} = \int_{\tilde{V}} \tilde{f}(\tilde{t}, \tilde{\mathbf{x}}, \tilde{L}) \tilde{V} d\tilde{V}, \tag{2.53}$$

with

- $\tilde{V}$ *as the volume of the particles.*

2.3.4 Growth

After nucleation had taken place, the nuclei formed began to grow into particles of a larger size. This process is called particle growth and, similarly to nucleation, is strongly based on thermodynamic considerations. Very often crystals of different sizes have the same shape. If this is the case, the crystal size may be represented by one characteristic linear dimension. Then, the linear growth rate $\tilde{G}$ *of the particle is defined as the rate of change of a characteristic size* $\tilde{L}$ *of the particle given as in (2.40) with respect to spherical particles and as in (2.41) and (2.42) with respect to needle-shape particles. Simplified and frequently used expressions for the growth rate are given in terms of supersaturation [64]*

$$\tilde{G} = k_g \sigma_{rel}^g, \tag{2.54}$$

with

- σ_{rel} $[\cdot]$ *as the relative supersaturation, see (2.52),*
- k_g $[\mathrm{m/s}]$ *as a kinematic parameter of growth correlated to the experimental data,*
- g $[\cdot]$ *as a kinetic order of growth.*

2.3.5 Aggregation

In the aggregation process, particles collide with each other and form a new larger particle. Further, it is important to differentiate between aggregation and agglomeration processes. While agglomeration describes the formation of permanent particle clusters, aggregation is the formation of possibly temporary ones.

For deriving the aggregation term, the volume $\tilde{V}$ of particles is considered. Further, only binary aggregation is assumed, since the probability that three or more particles collide in a time interval $(\tilde{t}, \tilde{t} + d\tilde{t})$ is negligible small compared with the probability that two particles collide. From a mathematical point of view, aggregation is described by a source and sink term. The source term describes the amount of particles of volume $\tilde{V}$ which are created by the aggregation of two particles with volume $\tilde{V}'$ and $\tilde{V} - \tilde{V}'$, $\tilde{V}' \in (0, \tilde{V})$, see Fig. 2.4. This

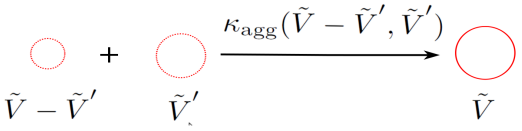

Figure 2.4: Aggregation: source term.

process is modeled by

$$\tilde{H}_{+,\mathrm{agg}}(\tilde{V}) = \frac{1}{2} \int_0^{\tilde{V}} \kappa_{\mathrm{agg}}(\tilde{V} - \tilde{V}', \tilde{V}') \tilde{f}_V(\tilde{V} - \tilde{V}') \tilde{f}_V(\tilde{V}') \, d\tilde{V}'. \tag{2.55}$$

The factor $1/2$ arises since there are two realizations of this event: the first particle has volume $\tilde{V}'$, the second has volume $\tilde{V} - \tilde{V}'$, and vice versa. The sink term describes the amount of particles of volume $\tilde{V}$ that vanish because they are consumed by aggregations with other particles of volume $\tilde{V}' \in (0, \tilde{V}^{\max})$, see Fig. 2.5.

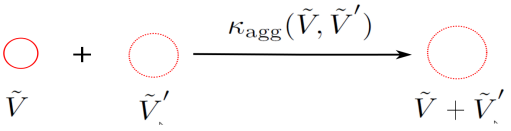

Figure 2.5: Aggregation: sink term.

$$\tilde{H}_{-,\mathrm{agg}}(\tilde{V}) = -\int_0^{\tilde{V}^{\max}} \kappa_{\mathrm{agg}}(\tilde{V},\tilde{V}')\tilde{f}_V(\tilde{V})\tilde{f}_V(\tilde{V}')\; d\tilde{V}' \tag{2.56}$$

$$= -\tilde{f}_V(\tilde{V})\int_0^{\tilde{V}^{\max}} \kappa_{\mathrm{agg}}(\tilde{V},\tilde{V}')\tilde{f}_V(\tilde{V}')\; d\tilde{V}'. \tag{2.57}$$

The sum of $\tilde{H}_{+,\mathrm{agg}}(\tilde{V})$ and $\tilde{H}_{-,\mathrm{agg}}(\tilde{V})$ gives the change of particles of volume $\tilde{V}$ due to the aggregation. In the literature can be found different kernels which are based on the mechanism by which particles collide and stick together. In the considered application it is used the aggregation kernel given in [74]. This kernel is the product of two factors

$$\kappa_{\mathrm{agg}}(\tilde{V},\tilde{V}') = p_{\mathrm{col}}(\tilde{V},\tilde{V}')p_{\mathrm{eff}}(\tilde{V},\tilde{V}') \quad \left[\frac{\mathrm{m}^3}{\mathrm{s}}\right]. \tag{2.58}$$

The first factor gives the probability of the collision of particles with volume $\tilde{V}$ and $\tilde{V}'$. The efficiency of the collisions, i.e., the amount of collisions which actually lead to aggregations, is described by the second factor. Due to the lack of models, this factor is chosen to be constant. This constant can be included into scaling factors for the individual terms of the following kernel, see [2, 52],

$$\begin{aligned}\kappa_{\mathrm{agg}}(\tilde{V},\tilde{V}') &= C_{\mathrm{br}}\frac{2k_BT}{3\mu}\left(\sqrt[3]{\tilde{V}}+\sqrt[3]{\tilde{V}'}\right)\left(\frac{1}{\sqrt[3]{\tilde{V}}}+\frac{1}{\sqrt[3]{\tilde{V}'}}\right)\\ &\quad + \frac{C_{\mathrm{sh}}}{k_V}\sqrt{2\nabla\mathbf{u}:\nabla\mathbf{u}}\left(\sqrt[3]{\tilde{V}}+\sqrt[3]{\tilde{V}'}\right)^3,\end{aligned} \tag{2.59}$$

where

- *k_V is a particle form factor,*
- *$k_B = 1,3806504\ 10^{-23}$ [J/K] is the Boltzmann constant,*
- *$C_{\mathrm{br}}, C_{\mathrm{sh}}$ are constants that have to be calibrated on the basis of the experimental data.*

These factors include also the collision efficiency $p_{\mathrm{eff}}(V-V',V')$.

The first term in (2.59) is Brownian-motion-generated. It is important for small particles since in this case the last factor becomes large. The second term is shear-induced [74] and it becomes important if both particles are large.

2.3.6 The dimensionless form

The dimensionless form of the equation is derived in the same way as the dimensionless form of Navier–Stokes and convection-diffusion equations. Besides the dimensionless quantities introduced in the Sec. 2.1.2 and Sec. 2.2.2, additional quantities are required:

$$f = \frac{\tilde{f}}{f_\infty},\ L = \frac{\tilde{L}}{L_\infty}.$$

Inserting these quantities into (2.44) one gets for the uni-variate case

$$\frac{f_\infty}{t_\infty}\frac{\partial f}{\partial t} + \tilde{G}\frac{f_\infty}{L_\infty}\frac{\partial f}{\partial L} + \frac{f_\infty u_\infty}{l_\infty}\mathbf{u}\cdot\nabla_x f \quad = \quad \tilde{H}, \tag{2.60}$$

or

$$\frac{\partial f}{\partial t} + G\frac{\partial f}{\partial L} + \mathbf{u}\cdot\nabla_x f \quad = \quad H, \tag{2.61}$$

where, $G := \dfrac{l_\infty}{u_\infty L_\infty}\tilde{G}$ *and* $H := \dfrac{l_\infty}{u_\infty f_\infty}\tilde{H}$.

Furthermore, using the additional quantities

$$L_1 = \frac{\tilde{L_1}}{L_{1,\infty}}, L_2 = \frac{\tilde{L_2}}{L_{2,\infty}}$$

in (2.45) one gets for the bi-variate case

$$\frac{f_\infty}{t_\infty}\frac{\partial f}{\partial t} + \tilde{G}_1\frac{f_\infty}{L_{1,\infty}}\frac{\partial f}{\partial L_1} + G_2\frac{f_\infty}{L_{2,\infty}}\frac{\partial f}{\partial L_2} + \frac{f_\infty u_\infty}{l_\infty}\mathbf{u}\cdot\nabla_x f \quad = \quad \tilde{H} \tag{2.62}$$

or

$$\frac{\partial f}{\partial t} + G_1\frac{\partial f}{\partial L_1} + G_2\frac{\partial f}{\partial L_2} + \mathbf{u}\cdot\nabla_x f \quad = \quad H, \tag{2.63}$$

where, $G_1 := \dfrac{l_\infty}{u_\infty L_{1,\infty}}\tilde{G}_1$, $G_2 := \dfrac{l_\infty}{u_\infty L_{2,\infty}}\tilde{G}_1$ *and* $H := \dfrac{l_\infty}{u_\infty f_\infty}\tilde{H}$.

2.3.7 Numerical methods

In order to solve these equations, initial and boundary conditions are prescribed for (2.61) and (2.62) result in

$$\begin{aligned} \frac{\partial f}{\partial t} + G\frac{\partial f}{\partial L} + \mathbf{u}\cdot\nabla_x f &= H_{+,\mathrm{agg}} + H_{-,\mathrm{agg}}, \\ f &= f_D \text{ on } [0, t_{\mathrm{end}}]\times\Gamma_D, \end{aligned} \tag{2.64}$$

$$f(0,\cdot) \quad = \quad f_0 \ \textit{in}\ \Omega \times (L_{\min}, L_{\max}),$$

and

$$\begin{aligned} \frac{\partial f}{\partial t} + G_1 \frac{\partial f}{\partial L_1} + G_2 \frac{\partial f}{\partial L_2} + \mathbf{u} \cdot \nabla_x f &= H_{\text{nuc}}, \\ f &= f_D \ \textit{on}\ [0, t_{\text{end}}] \times \Gamma_D, \\ f(0,\cdot) &= f_0 \\ \textit{in}\ \Omega \times (L_{1,\min}, L_{1,\max}) &\times (L_{2,\min}, L_{2,\max}). \end{aligned} \tag{2.65}$$

The transport equation of type (2.64) or (2.65) are given in four- and five-dimensional domain. Therefore, their solution is expected to be more expensive than the solution of convection-diffusion equations, e.g., (2.24). In [40], several schemes were explored for solving (2.64). It was found that for laminar flow fields, simple and inexpensive schemes yielded similar results for quantities of interest compared with more accurate and expensive schemes. In particular, finite element schemes are rather expensive because of the costs for assembling the matrices (the number of quadrature points scales exponentially with the dimension), see [7]. Furthermore, numerical studies in [39] based on higher order finite difference schemes gave comparatively results to methods based on finite element discretizations. In the considered applications the flow domain Ω is taken as a hexahedral tube, and with it, the four- and five-dimensional domain will be a tensor-product domain. Such a domain enables easily the application of finite difference methods. Based on the available experience, the following methods were applied for the discretization of (2.64) and (2.65):

- *forward Euler upwind finite difference method (FWE–UPW–FDM),*
- *backward Euler upwind finite difference method (BWE–UPW–FDM),*
- *total variation diminishing (TVD) explicit Runge–Kutta essentially non-oscillatory finite difference method (RK–ENO–FDM).*

In particular, the application of finite difference schemes to (2.65) becomes impossible due to the Dirac delta distribution included on the right-hand side (2.49), since for finite difference methods, the right-hand side must be a continuous function. In order to combat this inconvenient, a hybrid discretization was considered that used for the left-hand side in of (2.65) finite difference methods and for the right-hand side a finite volume method. Since the integral of the Dirac delta distribution is well-defined, the Dirac delta distribution can be discretized with finite volume methods. The hybrid discretization leads to a condition on the mesh for the internal coordinates that allows to adjust the scaling of the finite difference method for the left-hand side and the finite volume method for the right-hand side.

Beside that, an efficient algorithm was used for evaluating the aggregation integrals. A short presentation of these methods by the means of (2.61) is given in the following:

FWE–UPW–FDM *The forward Euler method is an explicit method, which is given at the time t_k by*

$$f_k^h = f_{k-1}^h - \Delta t_k F(t_{k-1}, f_{k-1}^h), \tag{2.66}$$

with

$$\Delta t_k = t_k - t_{k-1},$$

and

$$F(t, f) = G\frac{\partial f}{\partial L} + \mathbf{u} \cdot \nabla f - H. \tag{2.67}$$

Thus, it follows

$$f_k^h = f_{k-1}^h - \Delta t_k \left(\mathbf{u}_k^h \cdot \nabla f_{k-1}^h + G_k^h \frac{\partial f_{k-1}^h}{\partial L} - h_k^h \right), \tag{2.68}$$

where

- $\mathbf{u}_k^h$ *approximates* $\mathbf{u}$,
- G_k^h *approximates* G,
- H_k^h *approximates* H,

which are already computed variables at the time t_k.

The convective terms on the right-hand side of (2.68) are discretized by an upwind scheme [51]. The upwind scheme approximates the convective term with respect to the external coordinates in (x_i, L), assuming the 1-dimensional case, by

$$u_k^h \cdot \nabla f_{k-1}^h(x_i, L) \approx \begin{cases} u_k^h \dfrac{f_{k-1}^h(x_i, L) - f_{k-1}^h(x_{i-1}, L)}{x_i - x_{i-1}} & u_k^h \geqslant 0, \\ u_k^h \dfrac{f_{k-1}^h(x_{i+1}, L) - f_{k-1}^h(x_i, L)}{x_{i+1} - x_i} & u_k^h < 0, \end{cases} \tag{2.69}$$

and with respect to internal coordinate in $(\mathbf{x}, L_i)$

$$G_k^h \frac{\partial f_{k-1}^h}{\partial L}(\mathbf{x}, L_i) \approx \begin{cases} G_k^h \dfrac{f_{k-1}^h(\mathbf{x}, L_i) - f_{k-1}^h(\mathbf{x}, L_{i-1})}{L_i - L_{i-1}} & \text{if } G_k^h \geqslant 0, \\ G_k^h \dfrac{f_{k-1}^h(\mathbf{x}, L_{i+1}) - f_{k-1}^h(\mathbf{x}, L_i)}{L_{i+1} - L_i} & \text{if } G_k^h < 0. \end{cases} \tag{2.70}$$

where

- u_k^h *is the i-th component of the convection vector* $\mathbf{u}_k^h$,
- (x_{i-1}, L) *and* (x_{i+1}, L) *are the neighbor nodes of* (x_i, L) *with respect to the i-th component of external coordinate,*
- $(\mathbf{x}, L_{i-1})$ *and* $(\mathbf{x}, L_{i+1})$ *are the neighbor nodes of* $(\mathbf{x}, L_i)$ *with respect to the internal coordinate.*

It can be seen from (2.69) that the computation of f_k^h *using the forward Euler upwind finite difference scheme does not require the solution of the linear system of equations.*

RK–ENO–FDM *An optimal third order explicit total variation diminishing Runge–Kutta method [73] using (2.67) takes the form*

$$f_k^h = f_{k-1}^h - \Delta t_k \left(\frac{\kappa_1}{6} + \frac{\kappa_2}{6} + \frac{4\kappa_3}{6} \right), \tag{2.71}$$

where

$$\begin{aligned} \kappa_1 &= F(t_{k-1}, f_{k-1}^h), \\ \kappa_2 &= F(t_{k-1} + \Delta t_k, f_{k-1}^h + \Delta t_k \kappa_1), \\ \kappa_3 &= F\left(t_{k-1} + \frac{\Delta t_k}{2}, f_{k-1}^h + \frac{\Delta t_k}{4}\kappa_1 + \frac{\Delta t_k}{4}\kappa_2 \right). \end{aligned}$$

Further, the terms of the right-hand side of the equation (2.71) will be approximated by a more sophisticated procedure than the simple upwinding finite difference method, namely an essentially non-oscillatory (ENO) finite difference scheme of third order [72]. To obtain a higher order approximation than with a simple upwinding scheme, second and third order information on the numerical solution are used.

Denote by

- $P_1^1(L)$ *the polynomial that interpolates the function* f_{k-1}^h *at the nodes* $\{L_{i-1}, L_i, L_{i+1}\}$,

- $P_2^1(L)$ *the polynomial that interpolates the function* f_{k-1}^h *at the nodes* $\{L_{i-2}, L_{i-1}, L_i\}$,
- $P_j(L)$ *the polynomial that interpolates the function* f_{k-1}^h *at the nodes* $\{L_{i+1-j}, L_{i+2-j}, L_{i+3-j}, L_{i+4-j}\}$ *where* $j = 1, \cdots, 4$.

Define

$$\begin{aligned} a_1^1 &:= (P_1^1)_L(L_i) = f_{k-1}^h[L_{i-1}, L_i, L_{i+1}], \\ a_2^1 &:= (P_2^1)_L(L_i) = f_{k-1}^h[L_{i-2}, L_{i-1}, L_i], \\ a_1 &:= (P_1)_L(L_i) = f_{k-1}^h[L_i, L_{i+1}, L_{i+2}, L_{i+3}], \\ a_2 &:= (P_2)_L(L_i) = f_{k-1}^h[L_{i-1}, L_i, L_{i+1}, L_{i+2}], \\ a_3 &:= (P_3)_L(L_i) = f_{k-1}^h[L_{i-2}, L_{i-1}, L_i, L_{i+1}], \\ a_4 &:= (P_4)_L(L_i) = f_{k-1}^h[L_{i-3}, L_{i-2}, L_{i-1}, L_i], \end{aligned}$$

where $f_{k-1}^h[\cdot]$ *denotes divided differences.*

The basic idea of ENO interpolation consists in using the smoother approximation, where smoothness is measured by the absolute value of the second and third order divided differences. Then

$$\frac{\partial f_{k-1}^h}{\partial L}(\mathbf{x}, L_i) \approx \text{appropriate } a_j.$$

- *for the case of* $G_k^h \geqslant 0$, *the algorithm reads as follows:*

```
if      |f[L_{i-1}, L_i, L_{i+1}]| < |f[L_{i-2}, L_{i-1}, L_i]|
        if      |[L_{i-2}, L_{i-1}, L_i, L_{i+1}]| < |f[L_{i-1}, L_i, L_{i+1}, L_{i+2}]|
                choose a_3
        else
                choose a_2
        else
else
        if      |[L_{i-3}, L_{i-2}, L_{i-1}, L_i]| < |[L_{i-2}, L_{i-1}, L_i, L_{i+1}]|
                choose a_4
        else
                choose a_3
        end
end
```

- *for the case* $G_k^h < 0$, *the algorithm reads as follows:*

```
if      |f[L_{i-1}, L_i, L_{i+1}]| < |f[L_{i-2}, L_{i-1}, L_i]|
        if      |f[L_{i-2}, L_{i-1}, L_i, L_{i+1}]| < |f[L_{i-2}, L_{i-1}, L_i]|
                choose a_3
        else
                choose a_2
        else
else
        if      |f[L_{i-2}, L_{i-1}, L_i]| < |f[L_i, L_{i+1}, L_{i+2}, L_{i+3}]|
                choose a_2
        else
                choose a_1
        end
end
```

BWE–UPW–FDM *The backward Euler is an implicit method, which applied to (2.61) by using (2.67), leads to*

$$f_k^h + \Delta t_k \left(\mathbf{u}_k^h \cdot \nabla f_k^h + G_k^h \frac{\partial f_k^h}{\partial L} - H_k^h \right) = f_{k-1}^h. \tag{2.72}$$

Then, e.g., the discretization of the convective term with respect to internal coordinate in $(\mathbf{x}, L_i)$ in (2.72) is done with an upwind approach similar to (2.70)

$$G_k^h \frac{\partial f_k^h}{\partial L}(\mathbf{x}, L_i) \approx \begin{cases} G_k^h \dfrac{f_k^h(\mathbf{x}, L_i) - f_k^h(\mathbf{x}, L_{i-1})}{L_i - L_{i-1}} & \text{if } G_k^h \geqslant 0, \\ G_k^h \dfrac{f_k^h(\mathbf{x}, L_{i+1}) - f_k^h(\mathbf{x}, L_i)}{L_{i+1} - L_i} & \text{if } G_k^h < 0. \end{cases} \tag{2.73}$$

This leads to off-diagonal entries in the system matrix. The backward Euler upwind finite difference requires the solution of a linear system of equations in each discrete time which was solved with GMRES with SSOR (symmetric successive over relaxation) preconditioner [40].

Hybrid discretization for the bi-variate transport equation *The finite difference discretization is impossible to be applied in (2.65), since the right-hand side (2.49), is not a continuous function. An alternative approach is presented that use for the left-hand side in (2.65) finite difference methods and for the right-hand side a finite volume method. The Dirac delta distribution in (2.49) can be discretized with finite volume method, since the integral of the Dirac delta distribution is well-defined. In the derivation of this approach, a condi-*

tion on the mesh for the internal coordinates is derived that allows to adjust the scaling of the finite difference method for the left-hand side and the finite volume method for the right-hand side.

The domain spanned by the internal coordinates, Ω_L*, is a rectangle*

$$\Omega_L = [L_{1,\min}, L_{1,\max}] \times [L_{2,\min}, L_{2,\max}]$$

decomposed by cells

$$K_{i,j} = \left[L_{1,i-1/2}, L_{1,i+1/2}\right] \times \left[L_{2,j-1/2}, L_{2,j+1/2}\right], 1 \leqslant i \leqslant N_{L_1}, 1 \leqslant j \leqslant N_{L_2},$$

$$L_{1,\min} = L_{1,1/2} \leqslant L_{1,3/2} \leqslant \cdots \leqslant L_{1,N_{L_1}+1/2} = L_{1,\max},$$

$$L_{2,\min} = L_{2,1/2} \leqslant L_{2,3/2} \leqslant \cdots \leqslant L_{2,N_{L_2}+1/2} = L_{2,\max}.$$

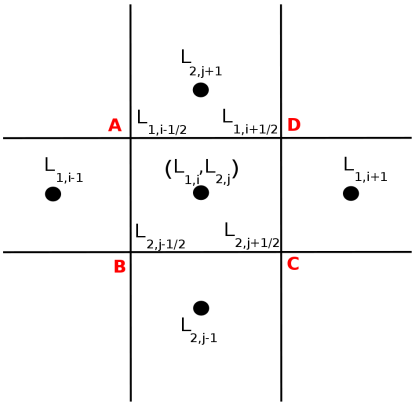

Figure 2.6: Cell $K_{i,j}$.

The centers of the cells are given by

$$(L_{1,i}, L_{2,j}),$$

where

$$L_{1,i} = \frac{L_{1,i-1/2} + L_{1,i+1/2}}{2}, L_{2,j} = \frac{L_{2,j-1/2} + L_{2,j+1/2}}{2}.$$

The mesh sizes are denoted by

$$\Delta L_{1,i} = L_{1,i+1/2} - L_{1,i-1/2}, i = 1, 2, \cdots N_{L_1},$$

$$\Delta L_{2,j} = L_{2,j+1/2} - L_{2,j-1/2}, j = 1, 2, \cdots N_{L_2}.$$

The finite volume formulation of (2.65) with respect to the internal coordinates for the particular cell $K_{i,j}$ reads [32]

$$\int_{K_{i,j}} G \cdot \nabla_L f d\Omega_L = \int_{K_{i,j}} H_{\text{nuc}} d\Omega_L, \tag{2.74}$$

with

$$G = \begin{pmatrix} G_1 \\ G_2 \end{pmatrix}, \Delta_L f = \begin{pmatrix} \frac{\partial f}{\partial L_1} \\ \frac{\partial f}{\partial L_2} \end{pmatrix}, H_{\text{nuc}} = B_{\text{nuc}} \delta(L_1 - L_{1,\text{nuc}}) \delta(L_2 - L_{2,\text{nuc}}).$$

Applying Gauss' divergence theorem to (2.74) and using the fact that

$$\nabla_L \cdot G = 0,$$

one obtains

$$\begin{aligned} \int_{\Gamma_{K_{i,j}}} (G \cdot \mathbf{n}_{K_{i,j}}) f \cdot d\Gamma_L &= B_{\text{nuc}} \int_{K_{i,j}} \delta(L_1 - L_{1,\text{nuc}}) \delta((L_2 - L_{2,\text{nuc}}) d\Omega_L \\ &= \begin{cases} 1 & \text{if } (L_{1,\text{nuc}}, L_{1,\text{nuc}}) \in K_{i,j}, \\ 0 & \text{else,} \end{cases} \end{aligned} \tag{2.75}$$

where the $\mathbf{n}_{K_{i,j}}$ is the unit normal vector to $\Gamma_{K_{i,j}}$ at $(L_{1,i}, L_{2,i})$, outward to $K_{i,j}$. Further, the left-hand side in (2.75) is discretized by

$$\int_{\Gamma_{K_{i,j}}} (G \cdot \mathbf{n}_{K_{i,j}}) f d\Gamma_L \approx \sum_{\Gamma_{K_{i,j}}} (G \cdot \mathbf{n}_{K_{i,j}}) f \tag{2.76}$$

with

$$\begin{aligned} \sum_{\Gamma_{K_{i,j}}} (G \cdot \mathbf{n}_{K_{i,j}}) f &= G_1^h \mathbf{n}_{AB} f^h_{i-1/2,j} |AB| + G_2^h \mathbf{n}_{BC} f^h_{i,j-1/2} |BC| \\ &\quad + G_1^h \mathbf{n}_{CD} f^h_{i+1/2,j} |CD| + G_2^h \mathbf{n}_{BC} f^h_{i,j+1/2} |DA| \\ &= G_1^h \Delta L_{2,j} \left(f^h_{i+1/2,j} - f^h_{i-1/2,j} \right) \\ &\quad + G_2^h \Delta L_{1,i} \left(f^h_{i,j+1/2} - f^h_{i,j-1/2} \right). \end{aligned} \tag{2.77}$$

The finite volume discretization of (2.74) becomes

$$G_1^h \Delta L_{2,j} \left(f^h_{i+1/2,j} - f^h_{i-1/2,j} \right) + G_2^h \Delta L_{1,i} \left(f^h_{i,j+1/2} - f^h_{i,j-1/2} \right) = B_{\text{nuc}}. \tag{2.78}$$

Multiplying (2.78) by $\dfrac{1}{\Delta L_{1,i}\Delta L_{2,j}}$*, one gets*

$$G_1^h \frac{\left(f^h_{i+1/2,j} - f^h_{i-1/2,j}\right)}{\Delta L_{1,i}} + G_2^h \frac{\left(f^h_{i,j+1/2} - f^h_{i,j-1/2}\right)}{\Delta L_{2,j}} = \frac{B_{\text{nuc}}}{\Delta L_{1,i}\Delta L_{2,j}}, \quad (2.79)$$

which is the representation of the central finite volume discretization. This type of discretization, in the case that convection dominates, could lead to oscillations in the solutions. Therefore, other types of finite volume discretization are investigated, e.g., upwind finite volume discretization or an essential non-oscillatory finite volume discretization. The evaluation of $f^h_{i-1/2,j}$*,* $f^h_{i+1/2,j}$*,* $f^h_{i,j+1/2,j}$*, and* $f^h_{i,j+1/2,j}$ *depends on the selected finite volume schemes.*

In particular, applying upwind finite volume discretization, the equation (2.79) changes to

$$G_1^h \frac{\left(f^h_{i,j} - f^h_{i-1,j}\right)}{\Delta L_{1,i}} + G_2^h \frac{\left(f^h_{i,j,j} - f^h_{i,j,j}\right)}{\Delta L_{2,j}} = \frac{B_{\text{nuc}}}{\Delta L_{1,i}\Delta L_{2,j}}, \quad (2.80)$$

for $G_1^h \geq 0$ *and* $G_2^h \geq 0$*. On the other hand, the left-hand side in (2.80) coincides with the upwind finite difference discretization of the left hand side in (2.74).*

In [72] was pointed out that for problems in more then one dimension, finite difference schemes should be preferred to finite volume methods. It turns out that in order to adjust the finite difference method in (2.74), the finite volume term on the right-hand side of (2.75) has to be multiplied by the scaling factor

$$\frac{1}{\Delta L_{1,i}\Delta L_{2,j}}.$$

Algorithm for evaluating the aggregation integrals *The aggregation integrals are computed by a modern approach from [28, 29, 30]. The grid for the PSD is discretized with respect to the volume of the particles and refined towards the smallest ones. For the algorithm, it is essential that this local refinement is not arbitrary, but that the locally refined grid can be decomposed into uniform grids at each level as it is illustrated in Fig. 2.7.*

The ansatz space $\mathcal{S}$ *for the PSD was chosen to consist of piecewise linear functions.*

Note that both terms in the considered aggregation kernel have separable structure, i.e., the aggregation kernel can be written in the form

$$\kappa_{\text{agg}}(V, V') = \sum_{i=1}^{k} a_i(V) b_i(V').$$

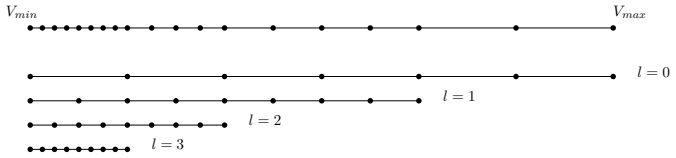

Figure 2.7: Decomposition of the locally refined grid for the PSD.

Then, the integral term becomes

$$H_{\text{agg}}(V) = H_{+,\text{agg}}(V) + H_{-,\text{agg}}(V) = \tag{2.81}$$

$$= \frac{1}{2}\int_0^V \kappa_{\text{agg}}(V - V', V') f_V(V - V') f_V(V')\ dV' \tag{2.82}$$

$$-f_V(V)\int_0^\infty \kappa_{\text{agg}}(V, V') f_V(V')\ dV' \tag{2.83}$$

$$= \sum_{i=1}^{k}\left[\frac{1}{2}\int_0^V a_i(V - V') b_i(V') f_V(V - V') f_V(V') dV' \right. \tag{2.84}$$

$$\left. -f_V(V) a_i(V)\int_0^\infty b_i(V') f_V(V')\ dV'\right]. \tag{2.85}$$

The evaluation of the sink term is not difficult since only one-dimensional integrals have to be computed.

The source term in this formulation is the sum of convolutions $\varphi_i * \psi_i$, where $\varphi_i = a_i f$ and $\psi_i = b_i f$. The functions $a_i(V)$ and $b_i(V)$ were approximated by piecewise constants on the same grid as $f_V(V)$. Legendre polynomials were used as an orthonormal basis of $\mathcal{S}$. Thanks to some known facts about Legendre polynomials, the convolution can be computed with the complexity $\mathcal{O}(n \log n)$, where n is the number of grid points. In essence, it turns out that some discrete convolutions have to be computed, which can be easily performed using the fast Fourier transform ($\mathcal{FFT}$) [61].

The exact convolution $\omega_{\text{exact}} = \sum_{i=1}^{k} \varphi_i * \psi_i$ does not belong to the ansatz space $\mathcal{S}$. In the simulations, the L^2 projection ω_{comp} of ω_{exact} into the ansatz space was used. An issue in using an approximation of ω_{exact} might be mass conservation. However, since $\omega_{\text{exact}} - \omega_{\text{comp}}$ is L^2 orthogonal to all piecewise linear functions, one obtains for all intervals $[V_i, V_{i+1}]$

$$mass_i(\omega_{\text{exact}}) = \int_{V_i}^{V_{i+1}} V' \omega_{\text{exact}}(V')\ dV'$$

$$= \int_{V_i}^{V_{i+1}} V' \omega_{\text{comp}}(V')\, dV' = mass_i(\omega_{\text{comp}}),$$

i.e., the mass (volume) is locally preserved. The only change in total mass that might occur comes from the fact that the support of the convolution is larger than the support of the convoluted functions. In the case of aggregation, only non-negative contributions will be neglected by not considering the complete support of the convolution such that the mass will always decrease. This might be crucial for long-time simulations. To avoid the decrease of mass, a correction to the aggregation term is computed as follows

$$H_{\text{agg}}(V) := H_{\text{agg}}(V) - mass(H_{\text{agg}}(V)) \frac{2}{V_{\max}^2 - V_{\min}^2},$$

where $V_{\min}$ *and* $V_{\max}$ *are the smallest and largest volume of the particles, respectively. Then, although the local mass conservation is violated, the total mass of the computed aggregation term is zero, which is in accordance with the modeling of this term.*

A different correction would be the L^2 *projection of* $H(V)$ *into the space of mass-conserved functions* $\{B(V) \ : \ \int_{V_{\min}}^{V_{\max}} V' B(V')\, dV' = 0\}$*, which has the form*

$$H_{\text{agg}}(V) := H_{\text{agg}}(V) - mass(H_{\text{agg}}(V)) \frac{3V}{V_{\max}^3 - V_{\min}^3}.$$

Due to the factor V *in the correction part, mainly the values* $H(V)$ *for large volumes will be affected. For the aggregation term, these values will increase to compensate the loss of mass due to cutting the support of the convolution. It could be observed that this might result in unnaturally large values for the aggregation term and then for the PSD, in the last interval for the internal coordinate. The same happened with the strategy proposed in [29], which applies a correction only in the last interval. Hence, these approaches are not recommended.*

2.4 Coupling

Population balance systems are modeled considering a flow field transporting the particles. This results in a system of partial differential equations where the Navier–Stokes equations for the fluid velocity and pressure are coupled to convection-diffusion equations for the species concentration and the system temperature and a transport equation for the particle size distribution as it is illustrated in Fig. 2.8. In order to solve such systems, one has to tackle a coupled problem. A general definition and classification of coupled problems

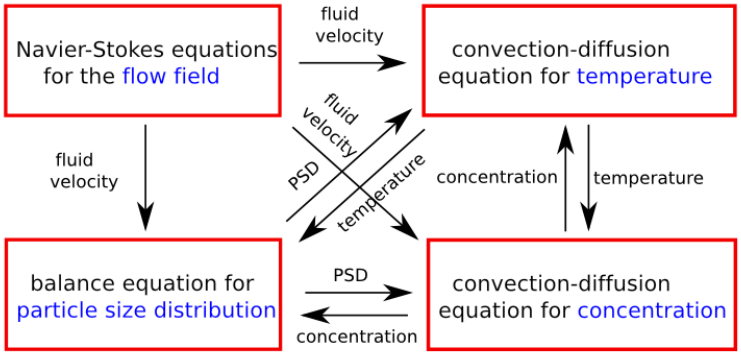

Figure 2.8: Coupled problem.

can be found in [78, 79] There are different ways to handle such problems [15, 16, 78, 79].

One possibility refers to a monolithical approach [3] or so-called direct method [69]. In this method all variables of the coupled problem are solved simultaneous.

Other possibilities are partitioned methods, also known as iterative methods. In this case each equation will be solved for its connection variable by treating the rest of the variables as known and iterating through the rest of the equations until the solution of the coupled system is achieved.

Whereas monolithcal approaches are difficult and expensive to use in the case of non-linear coupled problems, an advantage of the partitioned methods consists in the possibility of solving each equation of the system with an adequate numerical method. However, stability and convergence for partitioned methods possess a great challenge [15, 16].

The method of choice for our coupling approach is based on iterative methods. The coupling approach consists in solving three steps.

Firstly, the steady-state Navier–Stokes equations are computed separately, since the flow field for velocity $\mathbf{u}$ *and pressure* p *does not require any information from temperature* (T)*, concentration* (c) *and PSD* (f) *equations, in other words, whereas a one-way is realized a back-coupling can be neglected. In order to be solved, the steady-state Navier–Stokes equations of type (2.6) have to be linearized with a fixed point iteration (see Sec. 2.1.5) and discretized with an inf-sup stable pair of finite element spaces (see Sec. 2.1.6), at which the choice of the inf-sup stable pair* Q_2/P_1^{disc} *is discussed in Sec. 2.1.7.*

Secondly, fully developed temperature and concentration fields are computed by using the precomputed flow field arising from solving the steady-state Navier–Stokes equations. The system for temperature and concentration is solved by a

fixed point iteration. Both equations described by (2.25) are time-dependent and strongly convection-dominated. Therefore, apart from the spatial discretization a discretization in time is also required. The (2.25) for concentration and temperature were discretized in time with a Crank–Nicolson scheme and in space with Q_1 finite element. Due to the convection-dominated issue a stabilized finite element has to be applied. For this, a linear FEM–FCT method is used (see Sec. 2.2.3).

Thirdly, the fully coupled system consisting of the equations for temperature, concentration, and PSD are solved using the precomputed flow field, initial temperature, and concentration distribution. The nonlinear coupled system is solved iteratively with a fixed point iteration wherein one iteration consists in three sub-steps:

- *solve the equation for temperature with an current available approximation of the concentration and PSD;*
- *solve the equation for concentration with an approximation of the temperature computed in the first sub-step;*
- *solve the equation for PSD with an approximation of the temperature and concentration computed in the first two sub-steps.*

The iteration for solving the coupled system was stopped if the sum of the Euclidian norms of the residual vectors for concentration and temperature was below a prescribed tolerance.

2.5 Software MooNMD and aspects of the implementation

All the numerical simulations were performed with the program package MooNMD, Mathematics and object oriented Numerics in MagDeburg*, developed by former members of the numeric group at the Institut für Analysis und Numerik from Otto–von–Guericke–Universität Magdeburg. MooNMD is a freeware code written in C++ programming language. Generally, it may be used for solving partial differential equations in two- or three-dimensional domains [38]. The main advantage of MooNMD consists in the fact that the code can be adapted and upgraded for different problem settings, which is especially important for solving coupled systems, e.g., (3D/4D) and (3D/5D).*

In MooNMD, a number of numerical methods were disposable to be applied for solving coupled systems of type (3D/4D), e.g., from the applications proposed in [7, 40]. The considered uni-variate population balance system is an extension of the work proposed in [40]. In addition to [40], the nonlinear iteration for our coupled problem includes an equation for the system temperature.

Moreover, aggregation phenomena are also taken into account. In particular, for the evaluation of the aggregation integral was used an efficient method proposed in [43]. Whereas for the considered uni-variate population balance system, (3D/4D) coupled problem, only a few modules of the used algorithms have been implemented, the algorithms solving the considered bi-variate population balance system, (3D/5D) coupled problem, have been completely new implemented.

3 Simulation of uni-variate population balance systems

This chapter considers the simulation of urea synthesis, which is described by uni-variate population balance model. Our main focus is the numerical reproduction of the experimental data from from a laboratory experiment [6]. A numerical scheme for the discretization of the uni-variate population balance system of urea synthesis was proposed in [31]. In addition to [31], other two numerical methods are studied and compared with the experimental data.

3.1 The experimental setup

The laboratory experiments are completely described in [6]. Further, the experimental setup will be sketched as follows.

The solution (suspension) is made up of ethanol (solvent) and urea (solute), which, due to the cooling process, start to crystallize. This process is depicted in Fig. 3.1.

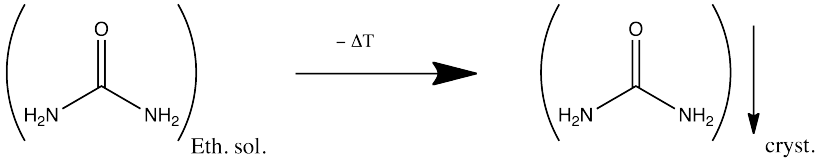

Figure 3.1: Cooling crystallization of urea synthesis.

The crystallization process takes place in continuous tubular reactors designed as plug flow reactors, as illustrated in Fig. 3.2.

On one hand, the strongest advantage of a continuous crystallization tube consists in the flexibility for controlling temperature, supersaturation and on the other hand, the possibility of spatial separation of different population dynamical phenomena, i.e., nucleation, growth, aggregation, breakage. Depending on the specific context, these phenomena might be desired or undesired, and they can be, in practice, controlled by chemical means, such as altering the solvent.

However, the considered application of urea synthesis is driven by aggregation. The task of the experiments is the quantification of aggregation within a tube and for this a flow-through microscope is employed.

The main components of the experiment are:

1 *vessel with crystal slurry (saturated solution with crystals),*

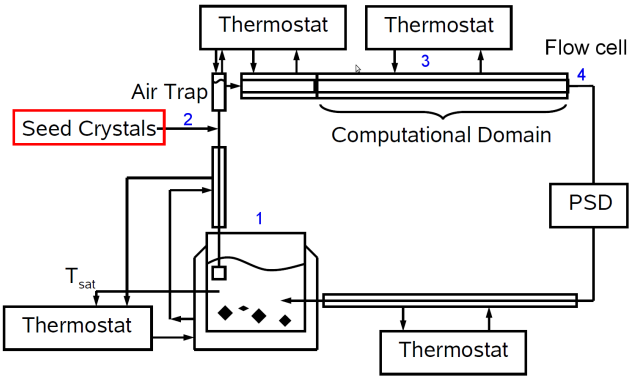

Figure 3.2: Schematic representation of the crystallizer.

2 seed crystal intake,

3 aggregation tube,

4 flow cell microscope with imaging sensor.

The proceeding of the experiment is as follows. The well-stirred vessel is filled with equilibrating crystal suspension which is kept at a constant temperature. Clear solution of ethanol is continuously withdrawn from the suspension through a frit and pumped into a tube, through the microscope flow cell and then back to the suspension vessel. At the start up only a clear solution is pumped through the system with a defined flow rate. Then, in a specific time interval, seed crystals are injected directly into the tube. The crystal population travels with the solution along the tube until it is photographed using a microscope with a flow-through cell, see Sec. 3.3.1.

Whereas nucleation, growth, and aggregation of the particles are taken into account, breakage phenomena will be neglected here.

3.2 The model

The studied urea population is modeled by a system of equations describing the flow field (velocity, pressure), the energy balance (temperature), the mass balance (concentration) and the particle size distribution.

3.2.1 Modeling the flow field

The experimental setups led to steady-state flow fields. Thus, the flow field is described by the incompressible Navier–Stokes equations, see Sec. 2.1,

$$\begin{aligned} -\mu\Delta\tilde{\mathbf{u}} + \rho\left((\tilde{\mathbf{u}}\cdot\nabla)\tilde{\mathbf{u}}\right) + \nabla\tilde{p} &= \tilde{\rho}\tilde{\mathbf{g}} \quad \textit{in } \tilde{\Omega}, \\ \nabla\cdot\tilde{\mathbf{u}} &= 0 \quad \textit{in } \tilde{\Omega}, \end{aligned} \tag{3.1}$$

with the following model parameter:

- $\tilde{\Omega} = (0, 210) \times (0, 1) \times (0, 1)$ $\left[\mathrm{cm}^3\right]$,
- $\rho = 789$ $\left[\mathrm{kg/m}^3\right]$ *the density of ethanol at* 298 K,
- $\mu = 1.074 \cdot 10^{-3}$ $[\mathrm{kg/(m\ s)}]$ *the dynamic viscosity of ethanol at* 298 K,
- $\tilde{\mathbf{g}} = 9.8$ $[\mathrm{m/s}^2]$ *the gravitational acceleration.*

In the experiments, the suspension is sufficiently diluted, the size of the particles is sufficiently small, and the temperature gradient is also small enough that the influence of all these aspects on the flow field can be neglected. Hence, the flow field can be modeled independently of the temperature field, concentration field, and particle size distribution.

The boundary is given by

$$\tilde{\Gamma} = \tilde{\Gamma}_{\mathrm{in}} \cup \tilde{\Gamma}_{\mathrm{out}} \cup \tilde{\Gamma}_{\mathrm{wall}}, \tag{3.2}$$

with

- $\tilde{\Gamma}_{\mathrm{in}} = \{0\ \mathrm{cm}\} \times (\frac{1}{3}\ \mathrm{cm}, \frac{2}{3}\ \mathrm{cm}) \times (\frac{1}{3}\ \mathrm{cm}, \frac{2}{3}\ \mathrm{cm})$ *as the inlet boundary,*
- $\tilde{\Gamma}_{\mathrm{out}} = \{210\ \mathrm{cm}\} \times (0\ \mathrm{cm}, 1\ \mathrm{cm}) \times (0\ \mathrm{cm}, 1\ \mathrm{cm})$ *as the outlet boundary,*
- $\tilde{\Gamma}_{\mathrm{wall}} = \Gamma \setminus (\Gamma_{\mathrm{in}} \cup \Gamma_{\mathrm{out}})$ *as the boundary at the walls.*

The unit outer normal vector on the boundary is denoted by $\mathbf{n}_{\tilde{\Gamma}}$.

The exact conditions at the inlet $\tilde{\Gamma}_{\mathrm{in}}$ *are not known, only the flow rates at the inlet. A simple approach would be the application of plug flows (constant velocities) at the inlet that matches the given flow rates. But this approach leads to jumps in the boundary condition. For this reason, in order to impose boundary data with enhanced regularity, an inlet boundary condition of the form*

$$\tilde{\mathbf{u}}(\tilde{\mathbf{x}}) = U_{\mathrm{in}}(\Psi(\xi(\tilde{\mathbf{x}}), \eta(\tilde{\mathbf{x}})), 0, 0)^T, \quad \tilde{\mathbf{x}} \in \tilde{\Gamma}_{\mathrm{in}}, \tag{3.3}$$

has been considered, where the profile $\Psi(\xi, \eta)$ *of this condition is the solution of the 2D Poisson equation*

$$-\Delta\Psi = 1 \ \textit{in } \tilde{\Gamma}_{\mathrm{in}}, \quad \Psi = 0 \ \textit{on } \partial\tilde{\Gamma}_{\mathrm{in}}. \tag{3.4}$$

The parameter U_{in} was chosen to match the experimental inflow rates, see Sec. 3.3.1. The boundary condition on the outlet $\tilde{\Gamma}_{\text{out}}$ is the standard do-nothing condition,

$$(\mu\nabla(\tilde{\mathbf{u}}) - \tilde{p}\mathbb{I}) \cdot \tilde{\mathbf{n}}_{\tilde{\Gamma}} = \mathbf{0}, \quad \tilde{\mathbf{x}} \in \tilde{\Gamma}_{\text{out}}, \tag{3.5}$$

*that is often used in numerical simulations, see 2.1.3. A boundary condition at the outlet is not known from the experiments. In particular it is unclear how good this boundary condition corresponds to (3.5). For this reason, the length of the computational domain was chosen to be larger than the experimental domain (*210 *cm instead of* 200 *cm) such that a possible slight incorrectness of the outflow boundary condition (3.5) has no influence on the computational results in the region that corresponds to the outlet of the experimental domain. At all other boundaries (the walls), the no-slip condition*

$$\tilde{\mathbf{u}}(\tilde{\mathbf{x}}) = \mathbf{0}, \quad \tilde{\mathbf{x}} \in \tilde{\Gamma}_{\text{wall}}, \tag{3.6}$$

was applied.

Using the corresponding dimensionless quantities in (3.1) and including the right-hand side into the pressure results in

$$\begin{aligned} -\frac{\nu}{l_\infty u_\infty}\Delta\mathbf{u} + (\mathbf{u}\cdot\nabla)\mathbf{u} + \nabla p &= \mathbf{0} \quad \text{in } \Omega, \\ \nabla\cdot\mathbf{u} &= 0 \quad \text{in } \Omega, \end{aligned} \tag{3.7}$$

with

- $\nu = \mu/\rho = 1.361 \cdot 10^{-6}\ [m^2/s]$ *as the kinematic viscosity of ethanol,*
- Ω *as the dimensionless domain.*

Furthermore, the dimensionless boundary conditions are

$$\begin{cases} \mathbf{u}(\mathbf{x}) = \dfrac{U_{\text{in}}}{u_\infty}(\Psi(\xi,\eta),0,0)^T, & \mathbf{x} \in \Gamma_{\text{in}}, \\ \left(Re^{-1}\nabla(\mathbf{u}) - p\mathbb{I}\right)\cdot\mathbf{n}_\Gamma = \mathbf{0}, & \mathbf{x} \in \Gamma_{\text{out}}, \\ \mathbf{u}(\mathbf{x}) = \mathbf{0}, & \mathbf{x} \in \Gamma_{\text{wall}}. \end{cases} \tag{3.8}$$

3.2.2 Modeling the mass balance

The mass balance of the system is modeled by

$$\begin{aligned} &\frac{\partial\tilde{c}}{\partial\tilde{t}} - D\Delta\tilde{c} + \tilde{\mathbf{u}}\cdot\nabla\tilde{c} = \\ &\quad - \frac{3\rho^d k_V \tilde{G}(\tilde{c},\tilde{T})}{m_{\text{mol}}} \int_{\tilde{L}_{\min}}^{\tilde{L}_{\max}} \tilde{L}^2 \tilde{f}\ d\tilde{L} \end{aligned}$$

$$- \quad -\frac{\rho^d k_V \tilde{L}_{\min}^3 B_{\text{nuc}}}{m_{\text{mol}}} \ \textit{in} \ (0, \tilde{t}_{\text{end}}) \times \tilde{\Omega}. \tag{3.9}$$

with

- $D = 1.35 \cdot 10^{-9} \ \left[\text{m}^2/\text{s}\right]$ *as the diffusion coefficient of urea in ethanol,*
- $\rho^d = 1323 \ \left[\text{kg}/\text{m}^3\right]$ *as the density of urea (dispersed phase),*
- $k_V = \pi/6 \ [\cdot]$ *as the scaling factor from diameters to volume (where it is assumed that all particles are balls), given below in (3.12),*
- $m_{\text{mol}} = 60.06 \cdot 10^{-3}$ [kg/mol] *as the molar mass of urea,*
- $B_{\text{nuc}} = 10^5 \ [1/(\text{m}^3 \ \text{s})]$ *as a constant nucleation rate,*
- $\tilde{L}_{\min} = 2.5 \cdot 10^{-6}$ [m] *and* $\tilde{L}_{\max} = 5000 \cdot 10^{-6}$ [m].

Whereas the decrease of dissolved urea due to the growth of particles is modeled by the first term on the right-hand side of (3.9), the consumption of dissolved urea due to the nucleation of particles is taken into account as the last term on the right-hand side.

Equation (3.9) has to be equipped with initial and boundary conditions. The boundary condition is given by

$$\begin{cases} \tilde{c}(\tilde{t}, \tilde{\mathbf{x}}) &= \tilde{c}_{\text{sat}}(\tilde{T}_{\text{in}}), & \tilde{\mathbf{x}} \in \tilde{\Gamma}_{\text{in}}, \\ D\dfrac{\partial \tilde{c}}{\partial \tilde{\mathbf{n}}_{\tilde{\Gamma}}} &= 0, & \tilde{\mathbf{x}} \in \tilde{\Gamma}_{\text{out}} \cup \tilde{\Gamma}_{\text{wall}}, \end{cases}$$

with the saturation concentration

$$\tilde{c}_{\text{sat}}(\tilde{T}) = \frac{35.364 + 1.305(\tilde{T} - 273.15)}{m_{\text{mol}}} \ \left[\frac{\text{mol}}{\text{m}^3}\right]. \tag{3.10}$$

With these boundary conditions, the equation (3.9) without the coupling terms to the PSD is solved until a steady state is reached. This steady state is used as initial condition

$$\tilde{c}(0, \tilde{\mathbf{x}}) = \tilde{c}_{\text{steady}}(\tilde{\mathbf{x}}). \tag{3.11}$$

The growth rate is given by

$$\tilde{G}(\tilde{c}, \tilde{T}) = \begin{cases} k_g \left(\dfrac{\tilde{c} - \tilde{c}_{\text{sat}}(\tilde{T})}{\tilde{c}_{\text{sat}}(\tilde{T})} \right)^g, & \textit{if } \tilde{c} > \tilde{c}_{\text{sat}}(\tilde{T}), \\ 0, & \textit{else}, \end{cases} \tag{3.12}$$

where

- $k_g = 10^{-7}$ [m/s] *is the growth rate constant*
- $g = 0.5$ [·] *is the growth rate power.*

Using the corresponding dimensionless quantities in (3.9) and proceeding as in Sec. 2.2.2 the dimensionless mass balance becomes

$$\begin{aligned} \frac{\partial c}{\partial t} &- \frac{D}{l_\infty u_\infty}\Delta c + \mathbf{u}\cdot\nabla c = \\ &- \frac{3\rho^d k_V G(c,T) L_\infty^3 f_\infty l_\infty}{c_\infty u_\infty m_{\text{mol}}} \int_{\frac{L_{\min}}{L_\infty}}^{\frac{L_{\max}}{L_\infty}} L^2 f \; dL \\ &- \frac{\rho^d k_V L_{\min}^3 B_{\text{nuc}} l_\infty L_\infty^3}{c_\infty u_\infty m_{\text{mol}}} \; \textit{in } (0, t_{\text{end}}) \times \Omega \end{aligned} \tag{3.13}$$

with

- *the growth rate*

$$G(c,T) = \begin{cases} k_g \left(\dfrac{c - c_{\text{sat}}(T)}{c_{\text{sat}}(T)} \right)^g, & \textit{if } c > c_{\text{sat}}(T), \\ 0, & \textit{else}, \end{cases} \tag{3.14}$$

- *dimensionless saturation concentration*

$$c_{\text{sat}}(T) = \frac{\tilde{c}_{\text{sat}}(T_\infty T)}{c_\infty}.$$

The dimensionless initial and boundary conditions become

$$c(0,\mathbf{x}) = \frac{\tilde{c}_{\text{steady}}(l_\infty \mathbf{x})}{c_\infty}, \tag{3.15}$$

$$\begin{cases} c(t,\mathbf{x}) &= \dfrac{\tilde{c}_{\text{sat}}(\tilde{T}_{\text{in}}}{c_\infty}, & \mathbf{x} \in \Gamma_{\text{in}}, \\ D\dfrac{\partial c}{\partial \mathbf{n}_\Gamma} &= 0, & \mathbf{x} \in \Gamma_{\text{out}} \cup \Gamma_{\text{wall}}. \end{cases} \tag{3.16}$$

3.2.3 Modeling the energy balance

The energy balance is modeled by

$$\begin{aligned} \rho c_p \frac{\partial \tilde{T}}{\partial \tilde{t}} &- \lambda \Delta \tilde{T} + \rho c_p \tilde{\mathbf{u}} \cdot \nabla \tilde{T} = \\ &- 3\Delta h_{\text{cryst}} \rho^d k_V \tilde{G}(\tilde{c}, \tilde{T}) \int_{\tilde{L}_{\min}}^{\tilde{L}_{\max}} \tilde{L}^2 \tilde{f} \; d\tilde{L} \end{aligned} \tag{3.17}$$

$$- \quad \Delta h_{\text{cryst}} \rho^d k_V \tilde{L}_{\min}^3 B_{\text{nuc}} \ \textit{in} \ (0, \tilde{t}_e) \times \tilde{\Omega},$$

where

- $c_p = 2441.3$ [J/(kg K)] *is the specific heat capacity of ethanol,*
- $\lambda = 0.167$ [J/(K m s)] *is the thermal conductivity of ethanol,*
- $\Delta h_{\text{cryst}} = 2.1645 \ \cdot 10^5$[J/kg] *is the heat of solution (enthalpy change of solution).*

Whereas the decrease of temperature with respect to the growth of particles is modeled by the first term on the right-hand side of (3.17), the consumption of temperature with respect to the nucleation of particles is taken into account as the last term on the right-hand side.

The boundary conditions are known from the experiments

$$\begin{cases} \tilde{T}(\tilde{t}, \tilde{\mathbf{x}}) &= \tilde{T}_{\text{in}}, & \tilde{\mathbf{x}} \in \tilde{\Gamma}_{\text{in}}, \\ \lambda \dfrac{\partial \tilde{T}}{\partial \tilde{\mathbf{n}}_{\tilde{\Gamma}}} &= 0, & \tilde{\mathbf{x}} \in \tilde{\Gamma}_{\text{out}}, \\ \tilde{T}(\tilde{t}, \tilde{\mathbf{x}}) &= \tilde{T}_{\text{wall}}, & \tilde{\mathbf{x}} \in \tilde{\Gamma}_{\text{wall}}, \end{cases} \tag{3.18}$$

with

- $\tilde{T}_{\text{in}} = 301.15$ $[K]$,
- $\tilde{T}_{\text{wall}} = 291.15$ $[K]$.

Hence, the suspension is cooled at the wall.

As an initial condition, a fully developed temperature field, based on the solution of a steady-state equation without the coupling terms to the PSD, was chosen:

$$\tilde{T}(0, \tilde{\mathbf{x}}) = \tilde{T}_{\text{steady}}(l_\infty \mathbf{x}). \tag{3.19}$$

Further, the dimensionless form of the energy balance is given by

$$\begin{aligned} \frac{\partial T}{\partial t} \quad - \quad & \frac{\lambda}{l_\infty u_\infty \rho c_p} \Delta T + \mathbf{u} \cdot \nabla T = \\ - \quad & \frac{3 \Delta h_{\text{cryst}} \rho^d k_V G(c,T) L_\infty^3 f_\infty l_\infty}{\rho c_p u_\infty T_\infty} \int_{\frac{L_{\min}}{L_\infty}}^{\frac{L_{\max}}{L_\infty}} L^2 f \ dL \\ - \quad & \frac{\Delta h_{\text{cryst}} \rho^d k_V L_{\min}^3 B_{\text{nuc}} l_\infty L_\infty^3}{\rho c_p u_\infty T_\infty} \quad \textit{in} \ (0, t_e) \times \Omega. \end{aligned} \tag{3.20}$$

The dimensionless initial and boundary conditions are:

$$T(0, \mathbf{x}) = \frac{\tilde{T}_{\text{steady}}(\tilde{\mathbf{x}})}{T_\infty}, \tag{3.21}$$

$$\begin{cases} T_{\text{in}}(\mathbf{x}) &= \dfrac{\tilde{T}_{\text{in}}}{T_\infty}, & \mathbf{x} \in \Gamma_{\text{in}}, \\ \dfrac{\lambda}{l_\infty u_\infty \rho c_p} \dfrac{\partial T}{\partial \mathbf{n}_\Gamma} &= 0, & \mathbf{x} \in \Gamma_{\text{out}}, \\ T_{\text{wall}}(\mathbf{x}) &= \dfrac{\tilde{T}_{\text{wall}}}{T_\infty}, & \mathbf{x} \in \Gamma_{\text{wall}}. \end{cases} \tag{3.22}$$

3.2.4 Modeling the population balance

Population balances can be described in different coordinate systems, e.g., with respect to the volume or diameter of the particles.

Assuming the cube- or spherical-shaped idealization of the particles, the behavior of the particle size distribution with respect to the diameter of the particle is modeled by

$$\begin{aligned} \frac{\partial \tilde{f}}{\partial \tilde{t}} \quad + \quad & \tilde{G}(\tilde{c}, \tilde{T}) \frac{\partial \tilde{f}}{\partial \tilde{L}} + \tilde{\mathbf{u}} \cdot \nabla \tilde{f} = \\ & \tilde{H}_{+,\text{agg}} + \tilde{H}_{-,\text{agg}} \quad \textit{in } (0, \tilde{t}_e) \times \tilde{\Omega} \times (\tilde{L}_{\min}, \tilde{L}_{\max}), \end{aligned} \tag{3.23}$$

where

- $\tilde{f}$ *is the PSD with respect to the diameter* $\left[\dfrac{1}{\text{m}^4}\right]$,
- $\tilde{G}$ *is the growth rate expressed as the rate of change of particle length* $\left[\dfrac{\text{m}}{\text{s}}\right]$,
- $\tilde{H}_{+,\text{agg}}$ *is the source of the aggregation model and* $\tilde{H}_{-,\text{agg}}$ *its sink with respect to the diameter* $\left[\dfrac{1}{\text{m}^4\text{s}}\right]$.

For modeling the aggregation, the volume of the urea particles is considered. Therefore, it follows that on one hand the considered population balance refers to the particle diameter and on the other hand to the particle volume. The transformation from one coordinate system to the other becomes necessary.

Let $\tilde{f}_V \left[\frac{1}{\text{m}^6}\right]$ *be the PSD with respect to the volume. The number of the particles with respect to the volume is the same as the number of particles with respect to the diameter. This can be expressed by*

$$\int_{\tilde{V}_{\min}}^{\tilde{V}_{\max}} \tilde{f}_V(\tilde{V}) d\tilde{V} = \int_{\tilde{L}_{\min}}^{\tilde{L}_{\max}} \tilde{f}(\tilde{L}) d\tilde{L}. \tag{3.24}$$

Further, it is assumed that the particle volume is proportional to the cube of the diameter as follows:

$$\tilde{V} = k_V \tilde{L}^3, \tag{3.25}$$

with $k_V > 0$, i.e., all particles are assumed to be of the same shape (balls, cubes). Then, the number of the particles with respect to the volume using (3.25) is given by

$$\int_{\tilde{V}_{\min}}^{\tilde{V}_{\max}} \tilde{f}_V(\tilde{V}) d\tilde{V} = \int_{\tilde{L}_{\min}}^{\tilde{L}_{\max}} \tilde{f}_V(k_V \tilde{L}^3) 3 k_V \tilde{L}^2 d\tilde{L}. \tag{3.26}$$

The comparison of the expressions (3.24) and (3.26) leads to the following transformation relationship:

$$\tilde{f}_V(\tilde{V}) = \tilde{f}_V(k_V \tilde{L}^3) = \frac{\tilde{f}(\tilde{L})}{3 k_V \tilde{L}^2}. \tag{3.27}$$

Then, the change with respect to the diameter for the right-hand side in (3.23) is obtained by

$$\tilde{H}_{+,\mathrm{agg}} + \tilde{H}_{-,\mathrm{agg}} = 3 k_V \tilde{L}^2 \left(\tilde{H}_{+,\mathrm{agg}}(\tilde{V}) + \tilde{H}_{-,\mathrm{agg}}(\tilde{V}) \right). \tag{3.28}$$

The initial condition is given by

$$\tilde{f}(0, \tilde{\mathbf{x}}, \tilde{L}) = 0 \quad \textit{in } \tilde{\Omega} \times (\tilde{L}_{\min}, \tilde{L}_{\max}), \tag{3.29}$$

i.e., there are no particles in the flow domain.

Boundary conditions are necessary at the closure of the inflow boundaries

$$\tilde{f}(\tilde{t}, \tilde{\mathbf{x}}, \tilde{L}) = \begin{cases} \tilde{f}_{\mathrm{in}}(\tilde{t}, \tilde{\mathbf{x}}, \tilde{L}), & \tilde{\mathbf{x}} \in \tilde{\Gamma}_{\mathrm{in}} \\ \dfrac{B_{\mathrm{nuc}}}{\tilde{G}(\tilde{c}, \tilde{T})}, & \textit{at } \tilde{L} = \tilde{L}_{\min}, \textit{ if } \tilde{G}(\tilde{c}, \tilde{T}) > 0, \end{cases} \tag{3.30}$$

where $\tilde{f}_{\mathrm{in}}$ is given by experimental data, see Sec. 3.3.1.

Using the corresponding dimensionless quantities in (3.23) and proceeding as in Sec. 2.3.6 the dimensionless population balance equation becomes

$$\begin{aligned} \frac{\partial f}{\partial t} \quad &+ \quad G(c,T) \frac{l_\infty}{u_\infty L_\infty} \frac{\partial f}{\partial L} + \mathbf{u} \cdot \nabla_x f \\ &= \quad \frac{l_\infty}{u_\infty f_\infty} (\tilde{H}_{+,\mathrm{agg}} + \tilde{H}_{-,\mathrm{agg}}) \quad \textit{in } (0, t_e) \times \Omega \times \left(\frac{L_{\min}}{L_\infty}, \frac{L_{\max}}{L_\infty} \right) \\ &= \quad \frac{3 k_V L_\infty^2 L^2 l_\infty}{u_\infty f_\infty} (H_{+,\mathrm{agg}}(V) + H_{-,\mathrm{agg}}(V)) \quad \textit{in } (0, t_e) \times \Omega \times \left(\frac{V_{\min}}{V_\infty}, \frac{V_{\max}}{V_\infty} \right). \end{aligned}$$

with

$$\tilde{H}_{+,\mathrm{agg}}(V) = \frac{1}{2}\int_{\frac{V_{\min}}{V_\infty}}^{\frac{V}{V_\infty}} \kappa_{\mathrm{agg}}(V_\infty V - V_\infty V', V_\infty V') \\ f_V(V_\infty V - V_\infty V') f_V(V_\infty V') dV',$$

$$\tilde{H}_{-,\mathrm{agg}}(V) = -\int_{\frac{V_{\min}}{V_\infty}}^{\frac{V_{\max}}{V_\infty}} \kappa_{\mathrm{agg}}(V_\infty V, V_\infty V') f_V(V_\infty V') dV'.$$

The dimensionless initial and boundary conditions of this equation are

$$f(0, \mathbf{x}, L) = 0 \quad \textit{in } \Omega \times \left(\frac{L_{\min}}{L_\infty}, \frac{L_{\max}}{L_\infty}\right), \tag{3.31}$$

$$f(t, \mathbf{x}, L) = \begin{cases} \dfrac{\tilde{f}_{\mathrm{in}}(t_\infty t, l_\infty \mathbf{x}, L_\infty L)}{f_\infty}, & \mathbf{x} \in \Gamma_{\mathrm{in}}, \\ \dfrac{B_{\mathrm{nuc}}}{f_\infty G(c,T)}, & \textit{at } L = \dfrac{L_{\min}}{L_\infty}, \ \textit{if } G(c,T) > 0. \end{cases} \tag{3.32}$$

In the numerical simulations, the following reference values were used:

- $f_\infty = 10^{13}\ \frac{1}{\mathrm{m}^4}$,
- $l_\infty = 0.01\ \mathrm{m}$,
- $u_\infty = 0.01\ \frac{\mathrm{m}}{\mathrm{s}}$,
- $T_\infty = 1\ \mathrm{K}$,
- $c_\infty = 1000\ \frac{\mathrm{mol}}{\mathrm{m}^3}$,
- $L_\infty = 5 \cdot 10^{-3}\ \mathrm{m}$,
- $V_\infty = L_\infty^3\ \mathrm{m}^3$.

3.3 Setup of the simulations

3.3.1 The incorporation of the experimental data

Data for space-time-averaged normalized volume fractions are provided, which were obtained by measurements using a microscope with a flow-through cell.

In the experiments, the flow rate at the inlet $\tilde{V}_r$ [ml/min] $= \tilde{V}_r/60$ [cm^3/s] *was prescribed. This data has to be matched by the flow rate of the used boundary condition at the inlet (3.3)*

$$\tilde{U}_{\text{in}} \int_{\Gamma_{\text{in}}} (\Psi(\xi,\eta),0,0)^T \; d\xi d\eta \; \left[\frac{\text{cm}^3}{\text{s}}\right].$$

It follows that

$$\tilde{U}_{\text{in}} = \frac{\tilde{V}_r}{60 \int_{\tilde{\Gamma}_{\text{in}}} (\Psi(\xi,\eta),0,0)^T \; d\xi d\eta},$$

where the integral in the nominator can be approximated by numerical quadrature.

The boundary conditions for the temperature are provided from the experiments as given in (3.18). Also the inlet condition of the concentration is controlled as given in (3.10).

Concerning the inlet condition of the PSD, particles were injected into the channel only in the time interval $[0, \tilde{t}_{\text{inj}}]$ s *with* $\tilde{t}_{\text{inj}} = 5$ s. *From the experiments, a space-time-averaged inlet condition is provided, such that a boundary condition of the form*

$$\tilde{f}_{\text{in}}(\tilde{t}, \tilde{\mathbf{x}}, \tilde{L}) = \begin{cases} \tilde{f}_{\text{inj}}(\tilde{L}) & \text{for } \tilde{t} \in [0, \tilde{t}_{\text{inj}}] \; s, \; \tilde{\mathbf{x}} \in \Gamma_{\text{in}}, \\ 0 & \text{else,} \end{cases}$$

can be applied. The particles were contained in a solution with volume $\tilde{V}_{\text{inj}}$ [m^3], *which was injected into the domain in* $[0, \tilde{t}_{\text{inj}}]$, *i.e.,*

$$\tilde{V}_{\text{inj}} = \int_0^{\tilde{t}_{\text{inj}}} \tilde{V}_r \; d\tilde{t} = \frac{\tilde{t}_{\text{inj}} \tilde{V}_r}{60 \cdot 10^6} \; [\text{m}^3].$$

It follows that the total number of particles which were injected is given by

$$\int_{\tilde{V}_{\text{inj}}} \int_{\tilde{L}_{\min}}^{\tilde{L}_{\max}} \tilde{f}_{\text{inj}}(\tilde{L}) \; d\tilde{L} \; d\tilde{\mathbf{x}} = \tilde{V}_{\text{inj}} \int_{\tilde{L}_{\min}}^{\tilde{L}_{\max}} \tilde{f}_{\text{inj}}(\tilde{L}) \; d\tilde{L} = \int_{\tilde{L}_{\min}}^{\tilde{L}_{\max}} \frac{\tilde{t}_{\text{inj}} \tilde{V}_r}{6 \cdot 10^7} \tilde{f}_{\text{inj}}(\tilde{L}) \; d\tilde{L}. \tag{3.33}$$

The experiments provide the distribution of the number of particles per diameter $\tilde{f}_{\tilde{L},\text{seed}}(\tilde{L})$ [1/m] *in* $\tilde{V}_{\text{inj}}$. *This number was identical in all experiments, see Fig. 3.3 for a presentation of this curve. Integration of* $f_{L,\text{seed}}(L)$ *gives the total number of particles. To obtain the same total number of particles as given in (3.33)*

$$\tilde{f}_{\tilde{L},\text{seed}}(\tilde{L}) = \frac{t_{\text{inj}} V_r}{6 \cdot 10^7} \tilde{f}_{\text{inj}}(\tilde{L}) \quad \Longrightarrow \quad \tilde{f}_{\text{inj}}(\tilde{L}) = \frac{6 \cdot 10^7}{\tilde{t}_{\text{inj}} \tilde{V}_r} \tilde{f}_{\tilde{L},\text{seed}}(\tilde{L}) \quad \tilde{L} \in \left[\tilde{L}_{\min}, \tilde{L}_{\max}\right],$$

should hold. This expression gives the required value for the boundary condition of the PSD at the inlet of the domain.

The experiments provide space-time-averaged evaluations of the volume fraction of the PSD. Let $\mathbf{x} \in \Omega$*, then the volume fraction is defined by*

$$q_3(\tilde{t}, \tilde{\mathbf{x}}, L) = \frac{\tilde{L}^3 \tilde{f}(\tilde{t}, \tilde{\mathbf{x}}, \tilde{L})}{\int_{\tilde{L}_{\min}}^{\tilde{L}_{\max}} \tilde{L}^3 \tilde{f}(\tilde{t}, \tilde{\mathbf{x}}, \tilde{L})\, d\tilde{L}}.$$

The normalized volume fraction of the inlet condition for the PSD is given in Fig. 3.3. Similarly derived profiles are provided at the outlet of the experimental domain ($x = 200$ cm*) for different flow rates. These profiles will be used in the comparison with the numerical results.*

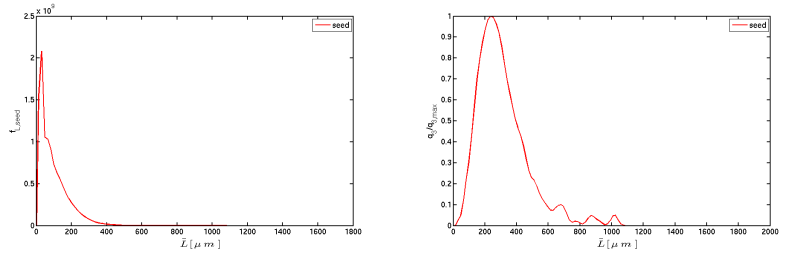

Figure 3.3: $\tilde{f}_{\tilde{L},\text{seed}}(\tilde{L})$ at the inlet (left) and the normalized volume fraction of the PSD at the inlet (right).

Experimental data were available for two setups which differed in the flow rate at the inlet. Both setups will be considered in the numerical studies. An important goal was the calibration of the unknown model parameters in the aggregation kernel (2.59) in such a way that a good agreement to the experimental data was obtained. This data consists of a space-time-averaged normalized volume fraction at the outlet. The second important aspect of the numerical studies was the investigation of the PSD at different points at the outlet. It will be shown that, e.g., the PSD in the center of the channel possesses a considerably different form compared with the PSDs in points which are closer to the walls. The third goal was the comparison of some numerical methods.

3.3.2 Computational domain

The flow domain is very long compared with its thickness and there is a preferred direction of the flow. This enables the use of an a priori adapted grid with anisotropic grid cells of $132 \times 12 \times 12$*, see Fig. 3.4. The aspect ratio (ratio of largest edge and smallest edge) of the mesh cells is small at the inlet to resolve*

the recirculation zone. It becomes larger towards the outlet. At the end of the flow domain, the mesh cells have an aspect ratio of 30.

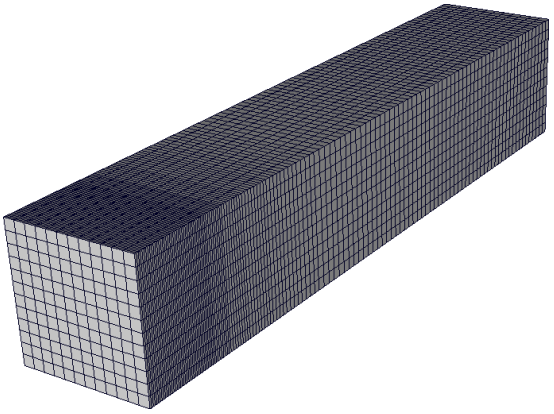

Figure 3.4: The computational grid, flow domain not to scale (scaled up by factor 40 in x_3- and x_3-direction).

In particular small particles were injected into the fluid, see Fig. 3.3. For this reason, the grid for the internal coordinate is locally refined for small diameters. As explained in Sec. 2.3.7, the computation of the aggregation integrals is based on a grid with respect to the mass of the particles which has to possess certain properties. This issue was taken into account in the construction of the grid with respect to the diameter, see Fig. 3.5 for both grids. The computational grid used for the mass is made of 94 piecewise equidistant nodes.

The corresponding numbers of the degree of freedom for the simulations are given in Tab. 3.1.

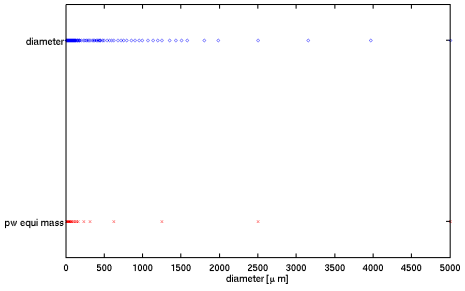

Figure 3.5: The grid with respect to the internal coordinate, diameter (top) and mass (bottom).

Simulation quantity	Number of d.o.f.
velocity	496 875
pressure	76 032
temperature	22 477
concentration	22 477
PSD	2 112 838

Table 3.1: D.o.f for simulating of the urea synthesis.

3.4 Numerical results

3.4.1 Experiment with flow rate 30ml/min

First, an experiment was studied that was conducted with a flow rate of $\tilde{V}_r = 30$ ml/min. *The Reynolds number based on the integral mean velocity at the inlet* $U = 4.5$ cm/s, *the diameter of the channel* 1 cm *and the kinematic viscosity of ethanol* $\nu = \mu/\rho = 1.3612\ 10^{-6}$ m^2/s *is given by* $Re \approx 331$. *The stationary flow field at the inlet of the channel is shown in Fig. 3.6.*

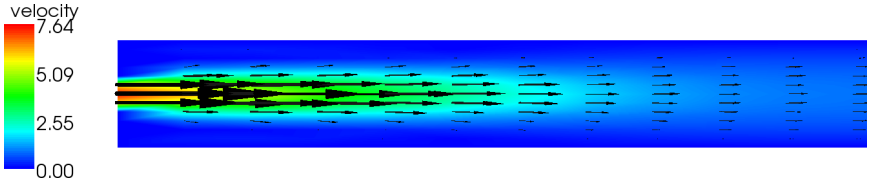

Figure 3.6: Experiment with flow rate $\tilde{V}_r = 30$ ml/min; cut of the stationary velocity field at the inlet of the channel.

Based on the residence time of the particles, the data at the outlet of the experimental domain at $\tilde{x}_1 = 200$ cm *were studied in the interval* $[200, 300]$ s. *For each grid point at the outlet, the PSD was added and then a time-average was computed. After this, a spatial averaging was calculated and from this the normalized volume fraction for these space-time-averaged values was derived. This normalized volume fraction was utilized for the calibration of the unknown parameters* C_{br} *and* C_{sh} *in the aggregation kernel (2.59). Furthermore, different numerical approaches were studied for discretizing the PSD equation.*

Results for the FWE–UPW–FDM and different values of the parameters C_{br} *and* C_{sh} *are presented in Fig. 3.7. Comparing the experimental data at the outlet with those at the inlet, Fig. 3.3, one can observe that the curve of the normalized volume fraction moves to the right. The increase of the number of larger particles due to aggregation and growth is clearly visible. A rather good*

agreement of the experimental and the numerical data could be obtained with $C_{\mathrm{br}} \simeq 2 \cdot 10^5$ *and* $C_{\mathrm{sh}} \simeq 0.01$.

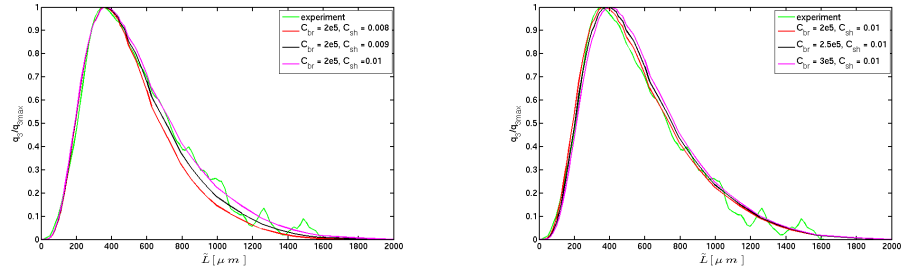

Figure 3.7: Flow rate $\tilde{V}_r = 30$ ml/min; space-time-averaged normalized volume fraction at the outlet for different parameters C_{br} and C_{sh}.

For these parameters, the PSD at the outlet was studied in more detail. Fig. 3.8 presents the time-averaged PSD which left the domain at different nodes in the outlet plane and Fig. 3.9 shows the corresponding normalized volume fractions. Nodes on a line between the wall and the center of the channel which is parallel to the plane $\tilde{x}_3 = 0$ *and nodes on a line between a corner of the outlet and the center of the channel were considered. First, it can be seen that the most particles could be found in the center of the channel, i.e., the bulk of the particles followed the flow very well. The closer the node was to the wall, the fewer the particles could be observed. In particular, the number of particles in the nodes with a distance less than or equal to* 1/6 cm *of one of the walls was negligible (green and cyan curves).*

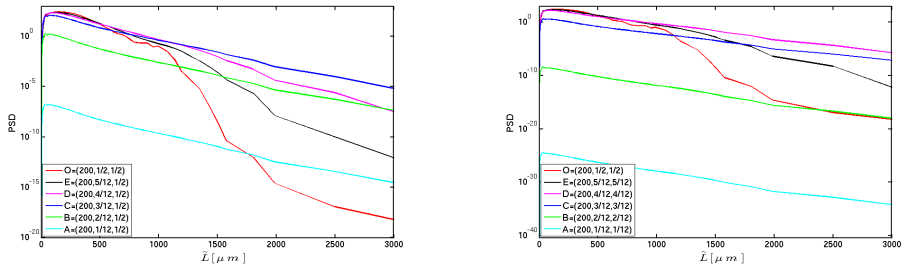

Figure 3.8: Flow rate $\tilde{V}_r = 30$ ml/min; time-averaged PSD at the outlet for different nodes, $C_{\mathrm{br}} = 2 \cdot 10^5$ and $C_{\mathrm{sh}} = 0.01$.

The distribution of the particles with respect to the diameter was very different for different nodes. In the center of the channel, most of the small particles

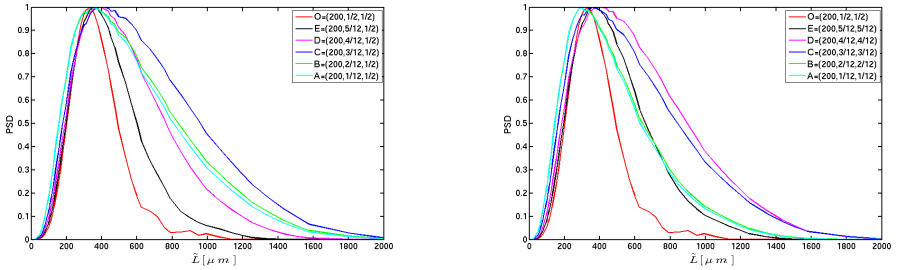

Figure 3.9: Flow rate $\tilde{V}_r = 30$ ml/min; time-averaged normalized volume fraction at the outlet for different nodes, $C_{\mathrm{br}} = 2 \cdot 10^5$ and $C_{\mathrm{sh}} = 0.01$.

were observed but only very few large particles. The majority of the large particles could be found in regions that were $1/4 - 1/3$ cm *away from the center of the channel. This different behavior can also be seen well in the normalized volume fractions in Fig. 3.9. The results for the individual nodes illustrate in a good way the effect of the different parts of the aggregation kernel (2.59). In the center of the channel, the shear of the flow field was comparatively small. For this reason, the second term in (2.59), which is of importance for the aggregation of large particles, did not possess much impact. Away from the center, the shear was larger. Hence, the second term of (2.59) became dominant in the kernel and larger particles were generated by the aggregation.*

The time step was set to be $\Delta t = 0.1$ s. *Because of the somewhat explosive start at the beginning of the simulations, a smaller length of the time step was applied in* $[0, 10]$ s. *It was checked that with smaller time steps the results practically do not change, see Fig 3.10:*

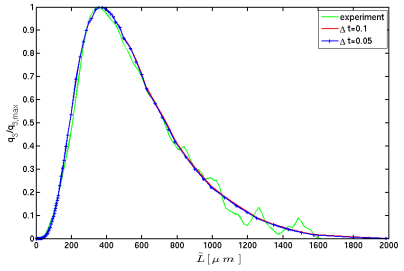

Figure 3.10: Flow rate $\tilde{V}_r = 30$ ml/min; space-time-averaged normalized volume fraction at the outlet with $C_{\mathrm{br}} = 2 \cdot 10^5$ and $C_{\mathrm{sh}} = 0.01$; FWE–UPW–FDM for $\Delta t = 0.1$, respectively $\Delta t = 0.05$.

Results with BWE–UPW–FDM and RK–ENO–FDM schemes are illustrated in Fig. 3.11. The behavior of the normalized volume fraction do not change

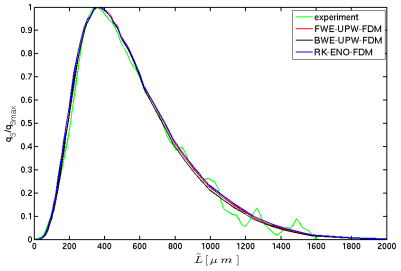

Figure 3.11: Flow rate $\tilde{V}_r = 30$ ml/min; space-time-averaged normalized volume fraction at the outlet for FWE–UPW–FDM, BWE–UPW–FDM ($C_{\mathrm{br}} = 2 \cdot 10^5$, $C_{\mathrm{sh}} = 0.01$) and RKV–ENO–FDM ($C_{\mathrm{br}} = 1 \cdot 10^5$, $C_{\mathrm{sh}} = 0.007$);

either qualitatively nor quantitatively by applying the first order schemes, e.g., FWE–UPW–FDM, BWE–UPW–FDM. Regarding the examined third order scheme, RK–ENO–FDM, a rather good agreement of the experimental and the numerical data could be obtained with the somewhat smaller parameters $C_{\mathrm{br}} \simeq 1 \cdot 10^5$ *and* $C_{\mathrm{sh}} \simeq 0.007$. *With these model parameters this scheme also aligns with the the other two.*

3.4.2 Experiment with flow rate 90ml/min

A second experiment was conducted with the flow rate $\tilde{V}_r = 90$ ml/min. *Also this flow rate led to a stationary flow field, see Fig. 3.12, with* $Re \approx 992$ *based on the same reference values as for the first example.*

Since the flow is considerably faster for $\tilde{V}_r = 90$ ml/min *than in the first experiment, the residence time of the particles is shorter. In particular, there will be less time to build large particles by aggregation and growth compared with the first experiment.*

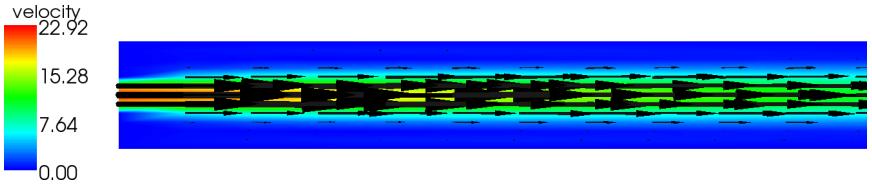

Figure 3.12: Experiment with flow rate $\tilde{V}_r = 90$ ml/min; cut of the stationary velocity field at the inlet of the channel.

Numerical results based on FWE–UPW–FDM for space-time-averaged normalized volume fractions at the outlet are presented in Fig. 3.13. Time-averaging of the PSD was performed in $[60 - 110]$ s. *Again, it was possible to calibrate the parameters in the aggregation kernel in such a way that a good agreement with the experimental data could be obtained. Appropriate parameters are* $C_{\mathrm{br}} \simeq 3 \cdot 10^5$ *and* $C_{\mathrm{sh}} \simeq 0.004$. *These parameters differ somewhat from the parameters obtained for the first example, but they are of the same order of magnitude.*

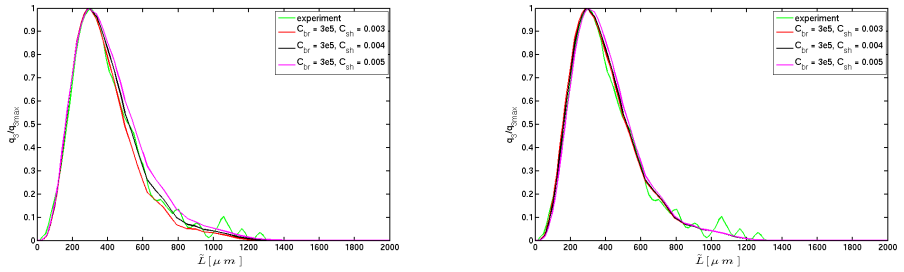

Figure 3.13: Flow rate $\tilde{V}_r = 90$ ml/min; space-time-averaged normalized volume fraction at the outlet for different parameters C_{br} and C_{sh}.

More detailed studies of the PSD at the outlet are presented in Figs. 3.14 and 3.15. The principal behavior is the same as for the first example. Most of the small particles, but almost no large particles, can be observed in the center of the channel. The large particles move away from the center. At the points which are too close to the walls, the amount of particles is negligible. In contrast to the first example, the amount of very large particles is much smaller, compared to the scaling. This is due to the shorter residence time.

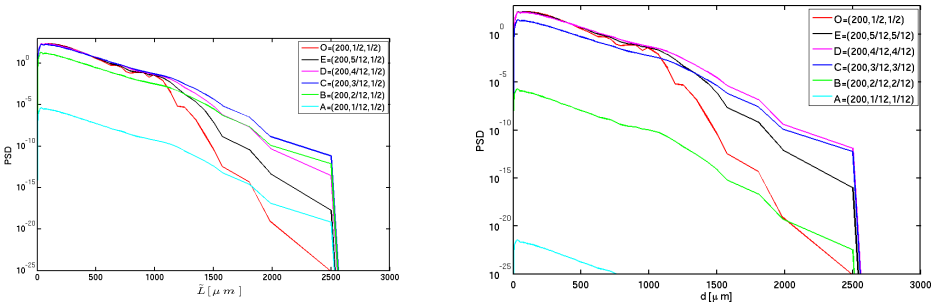

Figure 3.14: Flow rate $\tilde{V}_r = 90$ ml/min; time-averaged PSD at the outlet for different nodes, $C_{\mathrm{br}} = 3 \cdot 10^5$ and $C_{\mathrm{sh}} = 0.004$.

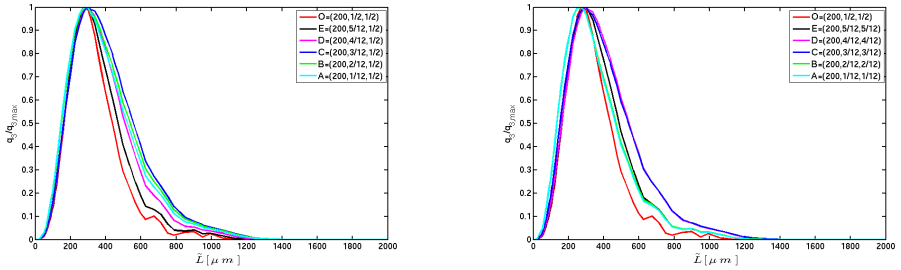

Figure 3.15: Flow rate $\tilde{V}_r = 90$ ml/min; time-averaged normalized volume fraction at the outlet for different nodes, $C_{\rm br} = 3{\cdot}10^5$ and $C_{\rm sh} = 0.004$.

The time step was set to be $\Delta t = 0.05$ s.

The results with BWE–UPW–FDM and RK–ENO–FDM schemes are illustrated in Fig. 3.16.

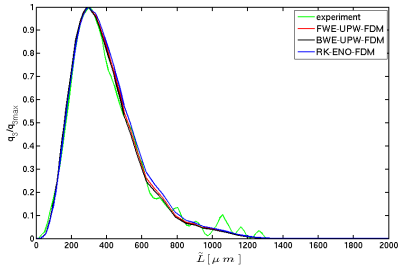

Figure 3.16: Flow rate $\tilde{V}_r = 90$ ml/min; space-time-averaged normalized volume fraction at the outlet for FWE–UPW–FDM, BWE–UPW–FDM ($C_{\rm br} = 3 \cdot 10^5$, $C_{\rm sh} = 0.004$) and RKV–ENO–FDM ($C_{\rm br} = 2 \cdot 10^5$,$C_{\rm sh} = 0.003$);

Also here, for the third order scheme (RK–ENO–FDM) a rather good agreement of the experimental and the numerical data could be obtained with the somewhat smaller parameters $C_{\rm br} \simeq 1 \cdot 10^5$ *and* $C_{\rm sh} \simeq 0.007$ *than in the first order schemes but with the same order of magnitude.*

3.4.3 CPU time

The simulations were performed on HP BL2x220c computers with 2933 MHz Xeon processors. Simulating one time step took around 45 – 60 seconds, including the calculation of all data for evaluating the numerical simulations.

The most expensive part was the computation of the aggregation which needed around 75 % of this time.

3.4.4 Conclusions

For both experimental setups, it was possible to identify model parameters C_{br} *and* C_{sh} *such that a very good agreement with the experimental data (space-time-averaged normalized volume fraction at the outlet) could be obtained. The optimal values for* C_{br} *and* C_{sh} *differ a little but they are of the same order of magnitude. We think that these differences are caused by the following reasons. First, the idealization of spherical particles was used in modeling the equation for the PSD. Second, the observed sizes of the diameters in the measurements were not diameters of three-dimensional particles, but diameters of projections of real particles into a plane. Both issues led, of course, to some errors in the measurements. The calibration of* C_{br} *and* C_{sh} *compensated for these errors quite well for each experiment. But this compensation led to somewhat different values for* C_{br} *and* C_{sh}*. Finally, (2.59) is only a model with an unknown modeling error.*

For the same unknown model parameter, first order schemes act more or less in the same way. Furthermore, the third order scheme align to the first order schemes for somewhat smaller parameters.

The impact of both parts of the aggregation kernel (2.59) could be observed well in detailed studies of the PSD in the nodes at the outlet. The numerical results correspond completely to the expectations.

4 Simulation of a bi-variate population balance systems

This chapter considers the simulation of bi-variate population balance systems based on crystallization of potassium dihydrogen phosphate (KDP). Real particles in crystallization processes are needle-shaped, so they cannot be represented by a single characteristic length. Thus, more geometrical properties of the particles are often needed to characterize the particles for such processes. Crystal shape characterization is rarely considered in modeling. The first characterization of the needle-shaped particles was introduced by [33]. Nowadays, there are only few models in the literature considering the anisotropy of particles [26, 54, 55, 56]. The disregard of shape dependence might be a possible reason of the discrepancy of the model parameters in the numerical studies of urea synthesis, see Sec. 3.4.4.

4.1 The setup

The setup of the simulations was chosen exactly the same as in Sec. 3.1. Potassium dihydrogen phosphate is the solute and water is the solvent. KDP is a popular model substance for bi-variate crystal research. The shape of KDP crystals is a tetragonal prism in combination with tetragonal bipyramids as illustrated in Fig. 4.1 [53]. The length of the crystal is given by $\tilde{L}_2$ and the width and depth are both equal to $\tilde{L}_1$. The volume of the crystal is given by

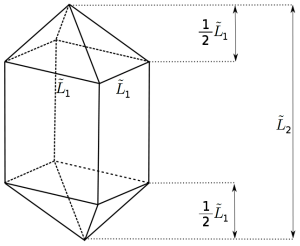

Figure 4.1: Characteristic lengths of KDP crystals.

$$\tilde{V} = \frac{1}{3}\tilde{L}_1{}^3 + \left(\tilde{L}_2 - \tilde{L}_1\right)\tilde{L}_1{}^2. \tag{4.1}$$

The model parameters used in this application are based on experimental data from [4, 5, 27, 75]. For the considered configuration, we do not possess mea-

surement data, neither for an initial nor for a final particles size distribution. Therefore, the considered model setup aims at investigating the differences of the results obtained with different numerical methods. The inlet distribution is taken as the following square pulse, see Fig. 4.2,

$$\tilde{f}_{\text{in}}(\tilde{t}, \tilde{\mathbf{x}}, \tilde{L}_1, \tilde{L}_2) = \begin{cases} 1, & \text{if } \tilde{L}_1 \in (150, 250)\mu\text{m},\ \tilde{L}_2 < (600, 1000)\mu\text{m}, \\ 0, & \text{else}, \end{cases} \tag{4.2}$$

for $\tilde{t} \in [0, \tilde{t}_{\text{inj}}]$ *s with* $\tilde{t}_{\text{inj}} = 10$ *s and* $\tilde{\mathbf{x}} \in \tilde{\Gamma}_{in}$ *defined as in (3.2).*

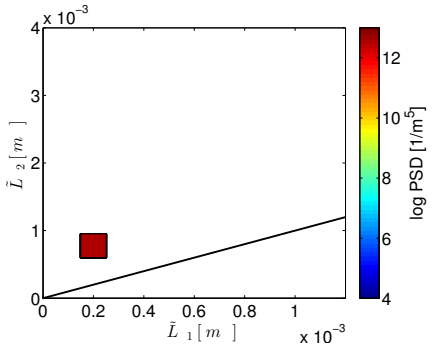

Figure 4.2: Initial distribution for KDP model.

4.2 The model

The population of KDP crystals is modeled similarly to the population balance system of urea synthesis. Secondary nucleation, growth, and transport of the particles are taken into account. For this example, the aggregation phenomena is neglected since there are no predictive models for the aggregation kernel available so far for bi-variate population balance systems.

4.2.1 Modeling the flow field

Assuming the experimental setup from Sec. 3.2, the flow field will be described by the incompressible steady-state Navier–Stokes equations

$$\begin{aligned} -\mu\Delta\tilde{\mathbf{u}} + \rho\left((\tilde{\mathbf{u}} \cdot \nabla)\tilde{\mathbf{u}}\right) + \nabla\tilde{p} &= \rho\tilde{\mathbf{g}} \quad \text{in } \tilde{\Omega}, \\ \nabla \cdot \tilde{\mathbf{u}} &= 0 \quad \text{in } \tilde{\Omega}, \end{aligned} \tag{4.3}$$

with the following model parameters:

- $\rho = 1160\ \left[\text{kg/m}^3\right]$ *density of the overall solution at* $298\ [K]$,

- $\mu = 1.5 \cdot 10^{-3}$ [kg/(m s)] *the dynamic viscosity of the overall solution at* 298 $[K]$.

Also in this case, the model for the flow field neglects the dependence of the temperature field, concentration field, and particle size distribution.

The boundaries are given as in (3.2) and the conditions on the boundaries are imposed as in (3.3), (3.5), and (3.6).

Further, derived similarly to (3.7), the dimensionless form of (4.3) reads

$$\begin{aligned} -\frac{\nu}{l_\infty u_\infty}\Delta\mathbf{u} + (\mathbf{u}\cdot\nabla)\mathbf{u} + \nabla p &= \mathbf{0} \text{ in } \Omega, \\ \nabla\cdot\mathbf{u} &= 0 \text{ in } \Omega, \end{aligned} \tag{4.4}$$

with

- $\nu = \mu/\rho = 1.2931 \cdot 10^{-6}$ [m^2/s] *as the kinematic viscosity of the overall solution.*

The dimensionless boundary conditions are given as in (3.8).

4.2.2 Modeling the mass balance

The mass balance of the KDP system is modeled by

$$\frac{\partial\tilde{c}}{\partial\tilde{t}} - D\Delta\tilde{c} + \tilde{\mathbf{u}}\cdot\nabla\tilde{c} = \frac{\tilde{\sigma}_{\mathrm{gr}}}{m_{\mathrm{mol}}} \text{ in } (0,\tilde{t}_{\mathrm{end}})\times\tilde{\Omega}, \tag{4.5}$$

where

- $\tilde{\sigma}_{\mathrm{gr}}$ $\left[\mathrm{kg}/(\mathrm{m}^3\mathrm{s})\right]$ *is the mass transferred from the fluid to the solid phase due to the growth per unit time and unit space,*
- $m_{\mathrm{mol}} = 136.08 \cdot 10^{-3}$ [kg/mol] *is the molar mass of KDP,*
- $D = 5.5 \cdot 10^{-10}$ $\left[\mathrm{m}^2/\mathrm{s}\right]$ *is diffusion coefficient of KDP in water.*

According to (2.23) and using (4.1), the consumption of mass with respect to the growth rate is modeled by the term on the right-hand side in (4.5),

$$\begin{aligned} \tilde{\sigma}_{\mathrm{gr}} = -\rho^d \int_{\tilde{L}_{2,\min}}^{\tilde{L}_{2,\max}} \int_{\tilde{L}_{1,\min}}^{\min\{\tilde{L}_2,\tilde{L}_{1,\max}\}} & \left(2\tilde{G}_1(\tilde{L}_1\tilde{L}_2 - \tilde{L}_1^2) + \tilde{G}_2\tilde{L}_1^2\right) \\ & \times \tilde{f}(\tilde{t},\tilde{\mathbf{x}},\tilde{L}_1,\tilde{L}_2)\, d\tilde{L}_1 d\tilde{L}_2, \end{aligned} \tag{4.6}$$

with

- $\tilde{L}_{1,\min} = \tilde{L}_{2,\min} = 0$ [m],

- $\tilde{L}_{1,\max} = 1.2 \cdot 10^{-3}$ [m] *and* $\tilde{L}_{2,\max} = 4 \cdot 10^{-3}$ [m].

The growth rates for the individual internal coordinates are given by

$$\tilde{G}_1(\tilde{c}, \tilde{T}) = \begin{cases} k_{g_1} \left(\dfrac{\tilde{c} - \tilde{c}_{\text{sat}}(\tilde{T})}{\tilde{c}_{\text{sat}}(\tilde{T})} \right)^{g_1} & \text{if } \tilde{c} > \tilde{c}_{\text{sat}}(\tilde{T}), \\ 0 & \text{else}, \end{cases} \tag{4.7}$$

and

$$\tilde{G}_2(\tilde{c}, \tilde{T}) = \begin{cases} k_{g_2} \left(\dfrac{\tilde{c} - \tilde{c}_{\text{sat}}(\tilde{T})}{\tilde{c}_{\text{sat}}(\tilde{T})} \right)^{g_2} & \text{if } \tilde{c} > \tilde{c}_{\text{sat}}(\tilde{T}), \\ 0 & \text{else}, \end{cases} \tag{4.8}$$

with the model parameters:

- $\rho^d = 2338$ $\left[\text{kg/m}^3\right]$ *as the density of KDP (dispersed phase),*
- $k_{g_1} = 1.221 \cdot 10^{-5}$ [m/s] *as growth rate constant with respect to* $\tilde{L}_1$,
- $k_{g_2} = 10.075 \cdot 10^{-5}$ [m/s] *as growth rate constant with respect to* $\tilde{L}_2$,
- $g_1 = 1.48$ $[\cdot]$ *as growth rate power with respect to* $\tilde{L}_1$,
- $g_2 = 1.74$ $[\cdot]$ *as growth rate power with respect to* $\tilde{L}_2$.

The saturation concentration is taken as in [56],

$$\frac{\tilde{\rho}^c_{\text{sat}}}{m_{\text{mol}}} = \tilde{c}_{\text{sat}}(\tilde{T}) = \frac{9.3027\ 10^{-5}\tilde{T}^2 - 9.7629\ 10^{-5}\tilde{T} + 0.2087}{m_{\text{mol}}}. \tag{4.9}$$

Considering the boundary conditions defined as in (3.10), equation (4.5) is solved, without the coupling terms to the PSD, until a steady-state is reached.

Derived similarly to (3.13), the dimensionless formulation of (4.5) reads

$$\frac{\partial c}{\partial t} - \frac{D_j}{l_\infty u_\infty} \Delta c + \mathbf{u} \cdot \nabla c = \frac{l_\infty}{u_\infty c_\infty m_{\text{mol}}} \tilde{\sigma}_{\text{gr}} \text{ in } (0, t_{\text{end}}) \times \Omega, \tag{4.10}$$

with

$$\begin{aligned} \tilde{\sigma}_{\text{gr}} \quad &= -\rho^d f_\infty L_{1,\infty}^2 L_{2,\infty} \\ &\int_{\frac{L_{2,\min}}{L_{2,\infty}}}^{\frac{L_{2,\max}}{L_{2,\infty}}} \int_{\frac{L_{1,\min}}{L_{1,\infty}}}^{\frac{\min\{L_2, L_{1,\max}\}}{L_{1,\infty}}} \left(2G_1(L_{2,\infty}L_1L_2 - L_{1,\infty}L_1^2) + L_{1,\infty}G_2L_1^2\right) \times \\ &f(t, \mathbf{x}, L_1, L_2)\ dL_1 dL_2. \end{aligned} \tag{4.11}$$

Further, the growth rates are given by

$$G_1(c,T) = \begin{cases} k_{g_1}\left(\dfrac{c - c_{\mathrm{sat}}(T)}{c_{\mathrm{sat}}(T)}\right)^{g_1} & \text{if } c > c_{\mathrm{sat}}(T), \\ 0 & \text{else}, \end{cases} \tag{4.12}$$

$$G_2(c,T) = \begin{cases} k_{g_2}\left(\dfrac{c - c_{\mathrm{sat}}(T)}{c_{\mathrm{sat}}(T)}\right)^{g_2} & \text{if } c > c_{\mathrm{sat}}(T), \\ 0 & \text{else}. \end{cases} \tag{4.13}$$

The dimensionless saturation concentration is as follows

$$c_{\mathrm{sat}}(T) = \frac{\tilde{c}_{\mathrm{sat}}(T_\infty T)}{c_\infty}.$$

Dimensionless initial and boundary conditions are given as in (3.15) and (3.16).

4.2.3 Modeling the energy balance

The energy balance for the KDP system is modeled by

$$\rho c_p \left(\frac{\partial \tilde{T}}{\partial t} + \mathbf{u}\cdot\nabla\tilde{T}\right) = \lambda\Delta\tilde{T} + \Delta h_{\mathrm{cryst}}\tilde{\sigma}_{\mathrm{gr}} \text{ in } (0,\tilde{t}_{\mathrm{end}})\times\tilde{\Omega}, \tag{4.14}$$

where

- $c_p = 4181.3$ [J/(kg K)] *is the specific heat capacity of water,*
- $\lambda = 0.602$ [J/(K m s)] *is the thermal conductivity of water,*
- $\Delta h_{\mathrm{cryst}} = 119$ [J/kg] *is the heat of solution (enthalpy change of solution).*

The decrease of temperature with respect to the growth of the particles is modeled by the term on the right-hand side of (4.14), $\tilde{\sigma}_{\mathrm{gr}}$, defined as in (4.6). The boundary condition are given as in (3.18) by

- $\tilde{T}_{\mathrm{in}} = 308.15$ [K],
- $\tilde{T}_{\mathrm{wall}} = 291.15$ [K].

As initial condition it was chosen a fully developed temperature field, which is based on the solution of a steady-state equation without coupling terms to PSD. It is given as in (3.19).

Further, similarly to (3.20), the dimensionless formulation of (4.14) takes the form

$$\frac{\partial T}{\partial t} - \frac{\lambda}{l_\infty u_\infty \rho c_p}\Delta T + \mathbf{u}\cdot\nabla T = \frac{l_\infty}{T_\infty u_\infty \rho c_p}\Delta h_{\text{cryst}}\tilde{\sigma}_{\text{gr}} \text{ in } (0,t_{\text{end}})\times\Omega \tag{4.15}$$

Dimensionless initial and boundary conditions are chosen as in (3.21) and (3.22).

4.2.4 Modeling the population balance

The population balance equation for the bi-variate model is given by

$$\begin{aligned}\frac{\partial \tilde{f}}{\partial \tilde{t}} &+ \tilde{G}_1(\tilde{c},\tilde{T})\frac{\partial \tilde{f}}{\partial \tilde{L}_1} + \tilde{G}_2(\tilde{c},\tilde{T})\frac{\partial \tilde{f}}{\partial \tilde{L}_2} + \tilde{\mathbf{u}}\cdot\nabla\tilde{f} \\ &= \tilde{H}_{\text{nuc}} \quad \text{in } (0,\tilde{t}_{\text{end}})\times\tilde{\Omega}\times(\tilde{L}_{1,\min},\tilde{L}_{1,\max})\times(\tilde{L}_{2,\min},\tilde{L}_{2,\max}).\end{aligned} \tag{4.16}$$

The right-hand side in (4.16) accounts for nucleation which is assumed to occur at the smallest particles, see Sec. 2.3.3,

$$\tilde{H}_{\text{nuc}} = \tilde{B}_{\text{nuc}}(\tilde{c},\tilde{T})\tilde{V}_{cryst}\delta(\tilde{L}_1-\tilde{L}_{1,\text{nuc}})\delta(\tilde{L}_2-\tilde{L}_{2,\text{nuc}}), \tag{4.17}$$

with

$$\delta(\tilde{L}_1-\tilde{L}_{1,\text{nuc}}) = \begin{cases}1 & \text{if } \tilde{L}_1 = \tilde{L}_{1,\text{nuc}} = 50\cdot 10^{-6}\text{ m},\\ 0 & \text{else},\end{cases} \tag{4.18}$$

$$\delta(\tilde{L}_2-\tilde{L}_{2,\text{nuc}}) = \begin{cases}1 & \text{if } \tilde{L}_2 = \tilde{L}_{2,\text{nuc}} = 100\cdot 10^{-6}\text{ m},\\ 0 & \text{else.}\end{cases} \tag{4.19}$$

This is a standard model for nucleation as proposed in [5]. The volume for the crystalline phase is given by

$$\begin{aligned}\tilde{V}_{\text{cryst}} &= \int_{\tilde{L}_{2,\min}}^{\tilde{L}_{2,\max}}\int_{\tilde{L}_{1,\min}}^{\min\{\tilde{L}_2,\tilde{L}_{1,\max}\}}\tilde{V}\tilde{f}d\tilde{L}_1 d\tilde{L}_2 \\ &= \int_{\tilde{L}_{2,\min}}^{\tilde{L}_{2,\max}}\int_{\tilde{L}_{1,\min}}^{\min\{\tilde{L}_2,\tilde{L}_{1,\max}\}}\left(\frac{1}{3}{\tilde{L}_1}^3 + \left(\tilde{L}_2-\tilde{L}_1\right)\tilde{L}_1\right)\tilde{f}d\tilde{L}_1 d\tilde{L}_2\end{aligned} \tag{4.20}$$

and the nucleation rate by

$$\tilde{B}_{\mathrm{nuc}}(\tilde{c},\tilde{T}) = \begin{cases} k_b \left(\dfrac{\tilde{c} - \tilde{c}^c_{\mathrm{sat}}(\tilde{T})}{\tilde{c}^c_{\mathrm{sat}}(\tilde{T})} \right)^b & \text{if } \tilde{c} > \tilde{c}^c_{\mathrm{sat}}(\tilde{T}), \\ 0 & \text{else}, \end{cases} \tag{4.21}$$

with the model parameters:

- $k_b = k_{\mathrm{nuc}} \ \left[1/(\mathrm{m}^6\mathrm{s})\right] \cdot V_{\mathrm{overall}} \ \left[\mathrm{m}^3\right] = 3.75 \cdot 10^{13} \ \left[1/(\mathrm{m}^6\mathrm{s})\right] \cdot V_{\mathrm{overall}} = 7.875 \cdot 10^9 \ \left[1/(\mathrm{m}^3\mathrm{s})\right]$ *nucleation rate constant [5] (calculated with respect to overall volume in the tube* $V_{\mathrm{overall}} = 2.1 \cdot 10^{-4} \left[\mathrm{m}^3\right]$*),*
- $b = 2.04 \ [\cdot]$ *nucleation rate power.*

The initial condition is given by

$$\tilde{f}(0,\tilde{\mathbf{x}},\tilde{L}_1,\tilde{L}_2) = 0 \quad \text{in } \tilde{\Omega} \times (\tilde{L}_{1,\min},\tilde{L}_{1,\max}) \times (\tilde{L}_{2,\min},\tilde{L}_{2,\max}). \tag{4.22}$$

Boundary conditions are necessary on closure of inflow boundaries

$$\tilde{f}(\tilde{t},\tilde{\mathbf{x}},\tilde{L}_1,\tilde{L}_2) = \begin{cases} \tilde{f}_{\mathrm{in}}(\tilde{t},\tilde{\mathbf{x}},\tilde{L}_1,\tilde{L}_2), & \tilde{\mathbf{x}} \in \tilde{\Gamma}_{\mathrm{in}}, \tilde{t} \in [0,10] \text{ s} \\ 0, & \text{else}, \end{cases} \tag{4.23}$$

where $\tilde{f}_{\mathrm{in}}$ *is given as a boundary distribution defined as in (4.2).*

Similarly to (3.31), the dimensionless formulation of (4.16) is given by

$$\begin{aligned} \frac{\partial f}{\partial t} \ &+ \ G_1 \frac{l_\infty}{u_\infty L_{1,\infty}} \frac{\partial f}{\partial L_1} + G_2 \frac{l_\infty}{u_\infty L_{2,\infty}} \frac{\partial f}{\partial L_2} + \mathbf{u} \cdot \nabla_x f \\ &= \ \frac{l_\infty}{u_\infty f_\infty} H_{\mathrm{nuc}} \quad \text{in } (0,t_{\mathrm{end}}) \times \Omega \times \left(\frac{L_{1,\min}}{L_{1,\infty}}, \frac{L_{1,\max}}{L_{1,\infty}} \right) \times \left(\frac{L_{2,\min}}{L_{2,\infty}}, \frac{L_{2,\max}}{L_{2,\infty}} \right), \end{aligned} \tag{4.24}$$

where

$$H_{\mathrm{nuc}} = B_{\mathrm{nuc}} V_{\mathrm{cryst}} \delta(\tilde{L}_1 - \tilde{L}_{1,\mathrm{nuc}}) \delta(\tilde{L}_2 - \tilde{L}_{2,\mathrm{nuc}}),$$

with

$$B_{\mathrm{nuc}}(c,T) = \begin{cases} k_b \left(\dfrac{c - c^c_{\mathrm{sat}}(T)}{c^c_{\mathrm{sat}}(T)} \right)^b & \text{if } c > c^c_{\mathrm{sat}}(T), \\ 0 & \text{else}, \end{cases} \tag{4.25}$$

and

$$V_{\mathrm{cryst}} = L^3_{1,\infty} L_{2,\infty} f_\infty \times \tag{4.26}$$

$$\times \int_{\frac{L_{2,\min}}{L_{2,\infty}}}^{\frac{L_{2,\max}}{L_{2,\infty}}} \int_{\frac{L_{1,\min}}{L_{1,\infty}}}^{\frac{\min\{\tilde{L}_2,\tilde{L}_{1,\max}\}}{L_{1,\infty}}} \left(\frac{1}{3}L_{1,\infty}L_1^3 + (L_{2,\infty}L_2 - L_{1,\infty}L_1)\,L_1\right) f d\tilde{L}_1 d\tilde{L}_2.$$

The dimensionless initial and boundary conditions are as following:

$$f(0,\mathbf{x},L_1,L_2) = 0 \quad \textit{in } \Omega \times \left(\frac{L_{1,\min}}{L_{1,\infty}}, \frac{L_{1,\max}}{L_{1,\infty}}\right) \times \left(\frac{L_{2,\min}}{L_{2,\infty}}, \frac{L_{2,\max}}{L_{2,\infty}}\right) \quad (4.27)$$

and

$$f(t,\mathbf{x},L_1,L_2) = \begin{cases} \dfrac{\tilde{f}_{\text{in}}(t_\infty t, l_\infty \mathbf{x}, L_{1,\infty}L_1, L_{2,\infty}L_2)}{f_\infty}, & \mathbf{x} \in \Gamma_{\text{in}}, t \in (0,10)\ \text{s} \\ 0, & \textit{else.} \end{cases} \quad (4.28)$$

In the numerical simulations, the following reference values were used:

- $f_\infty = 10^{13}\ \frac{1}{\text{m}^5}$,
- $l_\infty = 0.01$ m,
- $u_\infty = 0.01\ \frac{\text{m}}{\text{s}}$,
- $T_\infty = 1$ K,
- $c_\infty = 1\ \frac{\text{mol}}{\text{m}^3}$,
- $L_{1,\infty} = 1000 \cdot 10^{-6}$ m,
- $L_{2,\infty} = 1000 \cdot 10^{-6}$ m.

4.3 Numerical results

Since the numerical simulations are based on the same setup as for the urea synthesis, the flow domain is discretized as in Fig. 3.4, by using an a priori adapted anisotropic grid of $132 \times 12 \times 12$ *cells. Further, the internal coordinates' discretization uses* 25 *nodes with respect to the smallest length of the particle,* $\tilde{L}_1$*, and* 81 *nodes with respect to the largest length of the particle,* $\tilde{L}_2$*. The corresponding numbers of degrees of freedom for simulating the KDP process are given in Tab. 4.1.*

Considering the flow rate as in the application of urea synthesis, $\tilde{V}_r = 30$ ml/min*, one obtains a stationary flow field with Reynolds number* $Re \approx 348$*. The flow field at the inlet of the channel is shown in Fig. 4.3.*

Further, the fully developed temperature field at the inlet of the channel is illustrated in Fig. 4.4. At the beginning of the simulation, at $\tilde{t}_{\text{inj}} \in [0,10]$ s,

Simulation quantity	Number of d.o.f.
velocity	496 875
pressure	76 032
temperature	22 477
concentration	22 477
PSD	45 515 925

Table 4.1: D.o.f. for simulating the KDP process.

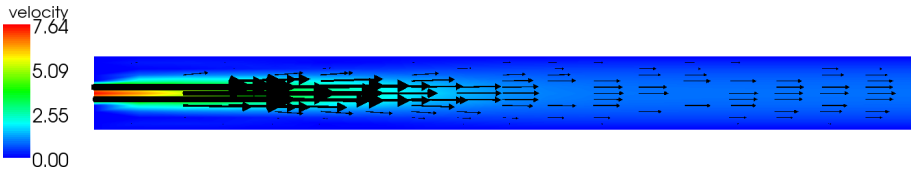

Figure 4.3: Flow rate $\tilde{V}_r = 30$ ml/min; cut of the stationary velocity field at the inlet of the tube, domain not to scale (KDP).

particles were injected into the channel, see Fig 4.2, for the initial PSD.

Two finite difference methods were investigated for solving the bi-variate population balance system, FWE–UPW–FDM and RK–ENO–FDM, in the time interval $[0, 300]$ s. *In order to apply these methods to the bi-variate transport equation, they were combined with a corresponding finite volume method, see Sec. 2.1.7.*

The final concentration distributions computed with these methods seem, at first glance, similar, but they are actually different in details, e.g., in the middle of the tube, at $\tilde{x}_1 \approx 100$ cm, *toward the walls, see Fig. 4.5. Altogether, it can be observed at the end of the channel that the concentration of the dissolved species computed with FWE–UPW–FDM is smaller than the concentration computed with RK-ENO-FDM. The different quantitative behavior in the results at the end of the channel arises from the fact that due to the smearing of the first*

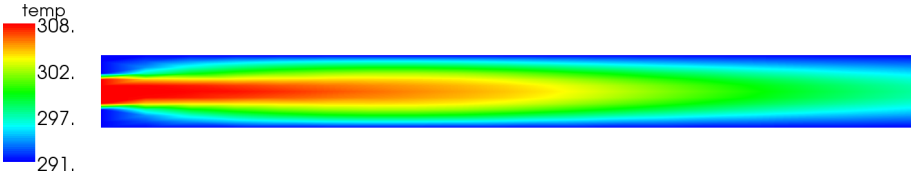

Figure 4.4: Flow rate $\tilde{V}_r = 30$ ml/min; cut of the initial temperature field at the inlet of the tube, domain not to scale (KDP).

order scheme larger particles are produced. This phenomenon will be clearly visible in plots with respect to the PSD in Fig. 4.13 – Fig. 4.24. For creating larger particles, more of the dissolved species has to be consumed, leading finally to smaller values for the concentration.

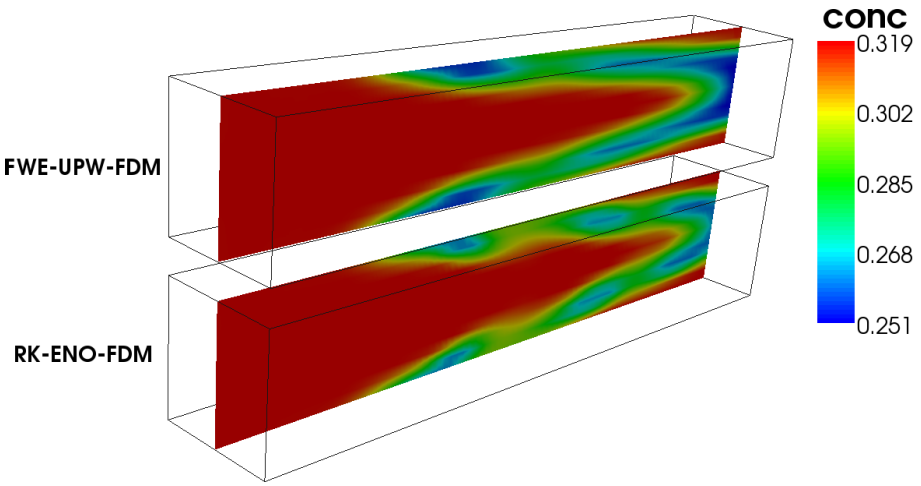

Figure 4.5: Final concentration distribution ($\tilde{t} = 300\,\mathrm{s}$) with FWE–UPW–FDM and RK–ENO–FDM for $\Delta t = 0.1$; concentration domain not to scale (scaled up by factor 40 in y- and z-direction) (KDP).

To highlight the differences of the results obtained with both methods, the PSD was studied at different locations in the tube. To this end, three cut planes were chosen, one close to the inlet at $\tilde{x}_1 = 17.5$ cm, *one more downstream at* $\tilde{x}_1 = 49$ cm, *and the last one also close to the outlet at* $\tilde{x}_1 = 200$ cm, *see Fig. 4.6.*

First, an appropriate time step has to be found. If the time step is too large, instabilities have to be expected because explicit time-stepping schemes were applied. If the time step is too small, then the simulation will become inefficient. In addition, from our experience, we expected that for sufficiently small time steps the discretization error in space dominates, and therefore a further decrease of the time step does not lead to an increase of the accuracy of the results. To find possible instabilities, the PSD in the center of the tube at the plane close to the inlet, at $(\tilde{x}_1, \tilde{x}_2, \tilde{x}_3) = (17.5, 1/2, 1/2)$ cm^3, *was studied, see Fig. 4.7. Up to this point, there was more or less only a transport of the initial PSD. In particular, one does not expect values that are much larger than the value of the initial pulse, which is* 10^{13}. *It can be seen in Fig. 4.7, upper pictures, that such values were computed for* $\Delta t = 0.2$ *(both schemes) and* $\Delta t = 0.15$ *(RK–ENO–FDM). The lower pictures of Fig. 4.7 reveal that*

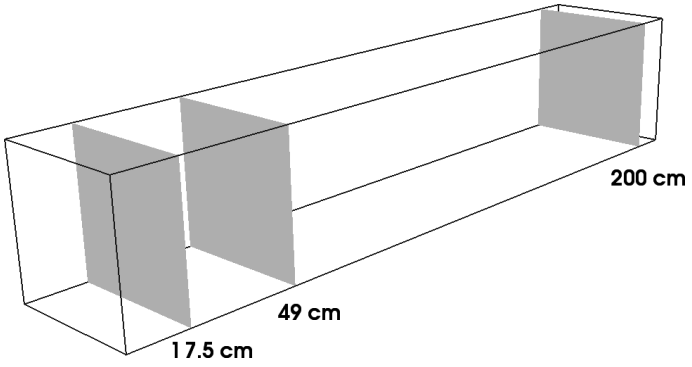

Figure 4.6: Cut planes, parallel to the plane $\tilde{x}_1 = 0$, for comparing the results obtained with the two different schemes.

for both schemes the results for $\Delta t \leqslant 0.1$ *were very similar. From Fig 4.8, it can be observed that this statement holds true also for the other cut planes. In summery,* $\Delta t = 0.1$ *has been proved to be an appropriate time step. Therefore, for all further studies, the time step was set to be* $\Delta t = 0.1$.

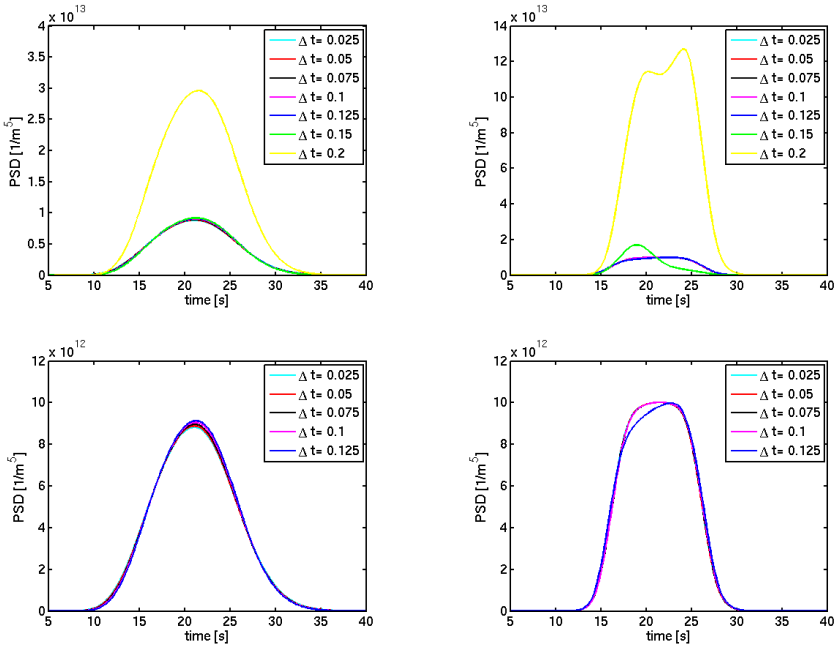

Figure 4.7: Maximal value of the PSD at $(\tilde{x}_1, \tilde{x}_2, \tilde{x}_3) = (17.5, 1/2, 1/2)$ cm^3 for different time steps; FWE–UPW–FDM (left); RK–ENO–FDM (right). Note the different scaling of the y-axis.

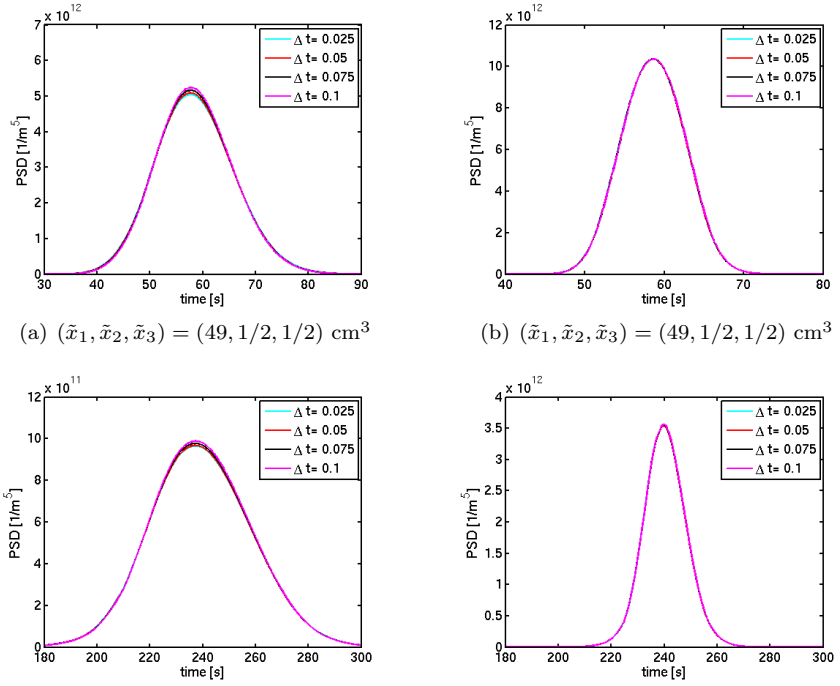

(a) $(\tilde{x}_1, \tilde{x}_2, \tilde{x}_3) = (49, 1/2, 1/2)$ cm^3

(b) $(\tilde{x}_1, \tilde{x}_2, \tilde{x}_3) = (49, 1/2, 1/2)$ cm^3

(c) $(\tilde{x}_1, \tilde{x}_2, \tilde{x}_3) = (200, 1/2, 1/2)$ cm^3

(d) $(\tilde{x}_1, \tilde{x}_2, \tilde{x}_3) = (200, 1/2, 1/2)$ cm^3

Figure 4.8: Maximal value of the PSD for different time steps; FWE–UPW–FDM (left); RK–ENO–FDM (right). Note the different scaling of the y-axis.

The temporal evolution of the PSD was studied not only at the center of the cut planes shown in Fig. 4.6, but also at other points situated in these planes. This points are sketched in Fig. 4.9. There is one set of points reaching from

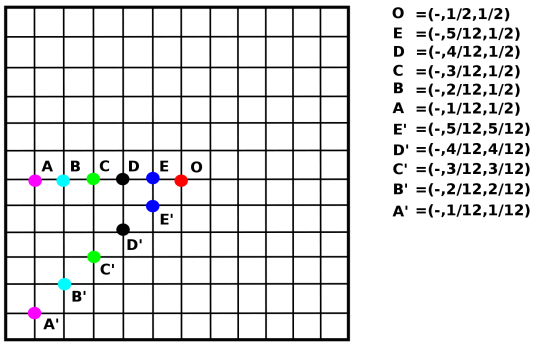

Figure 4.9: Studied nodes for the cut planes parallel to the plane $\tilde{x}_1 = 0$.

the center of the tube to the center of a lateral wall and another set, where the points reach from the center to the corner of two lateral walls. Due to the different velocities in all these points, a different evolution of the PSD can be expected. To keep the presentation of the results concise, we studied only the evolution of the maximal value of the PSD in these points, see Fig. 4.10 – Fig. 4.12. It can be seen that the largest maximal values were predicted in the center of the tube, i.e., the bulk of particles followed the flow very well. The further the point of observation was away from center, the smaller the maximal value of the PSD became. This general qualitative behavior was predicted by both of the studied schemes, FWE–UPW-FDM and RK–ENO–FDM. However, the height of the peaks (highest amount of particles that can be observed at the point at a certain time) and the time interval where the curve is clearly larger than zero (time interval where a notable number of particles can be observed at the point) often differed considerably between both methods. Always, the method FWE–UPW-FDM gave results with smaller peaks and larger time intervals in which particles could be observed. As an example, at the center of the tube close to the outlet $(\tilde{x}_1, \tilde{x}_2, \tilde{x}_3) = (200, 1/2, 1/2)$ cm^3*, the first order method predicted a notable amount of particles in the time interval* $[200, 280]$ s*, whereas the third order method showed this event in* $[220, 260]$ s*. Moreover, the maximal amount of particles predicted by RK–ENO–FDM was almost four times larger than the prediction of FWE–UPW-FDM. One can observe that the differences in the numerical results obtained with both methods were the larger, the further the cut plane was away from the inlet, i.e., the longer the PSD needed to reach the cut plane.*

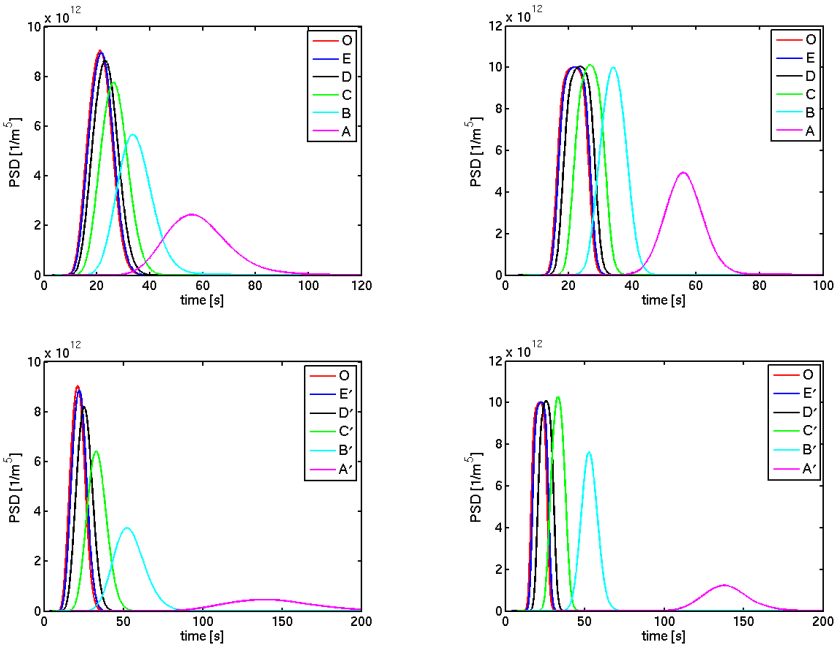

Figure 4.10: Maximal value of PSD at different nodes $(17.5, \tilde{x}_2, \tilde{x}_3)$ cm^3; FWE–UPW–FDM (left); RK–ENO–FDM (right). Note the different scaling of the y-axis.

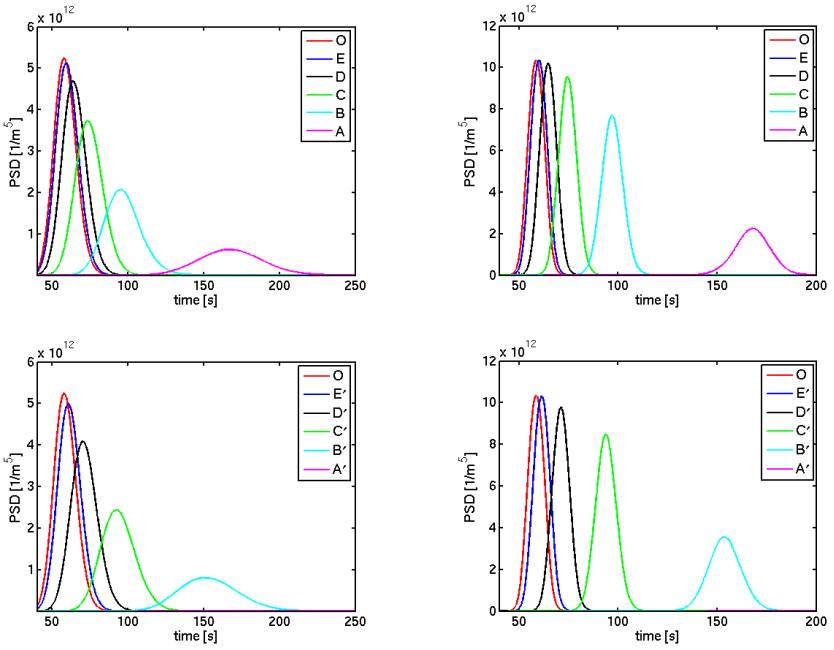

Figure 4.11: Maximal value of PSD at different nodes $(49, \tilde{x}_2, \tilde{x}_3)$ cm^3; FWE–UPW–FDM (left); RK–ENO–FDM (right). Note the different scaling of the y-axis.

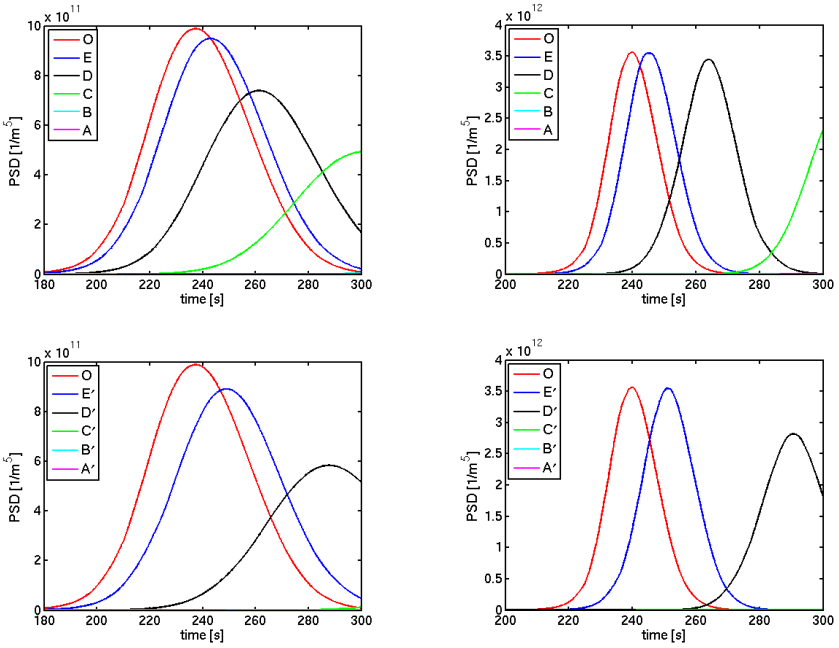

Figure 4.12: Maximal value of PSD at different nodes $(200, \tilde{x}_2, \tilde{x}_3)$ cm^3; FWE–UPW–FDM (left); RK–ENO–FDM (right). Note the different scaling of the y-axis. Maximal values of PSD in the nodes with a distance less or equal to 1/6 cm of one of the walls were negligible (magenta and cyan curves).

Finally, comprehensive illustrations of the PSD in the different points are provided in Fig. 4.13 – Fig. 4.24. In Fig. 4.13 – Fig. 4.18, the PSDs for the points situated on the line between the lateral wall and the center are presented, and in Fig. 4.19 – Fig. 4.24, the PSDs on the line from the corner to the center of the tube. For each picture, the time instance was chosen where the maximal value of the PSD was obtained. It can be clearly observed that results obtained with RK–ENO–FDM were much less smeared than the results computed with FWE-UPW–FDM. In addition, the maximal values of the PSDs were larger for RK–ENO–FDM. The smearing introduced by FWE-UPW–FDM results even to the fact that a notable amount of particles has already left the domain of computation for the internal coordinates at the end of the tube, see Fig. 4.17 and Fig. 4.23. Again, it can be observed that the largest differences between the two methods are near the outlet of the tube. The pictures in Fig. 4.13 – Fig. 4.24 also allow to distinguish between the part of the PSD that originates from the inlet condition and the part which comes from the nucleation. Also for the second part, the smearing introduced by FWE-UPW–FDM is clearly visible.

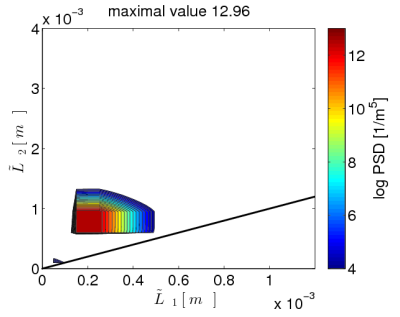

(a) $O = (17.5, 1/2, 1/2)$ cm^3; $\tilde{t}_{\max} = 21$ s

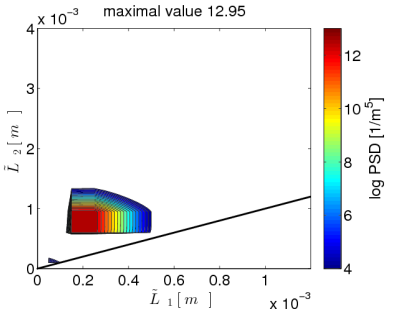

(b) $E = (17.5, 5/12, 1/2)$ cm^3; $\tilde{t}_{\max} = 22$ s

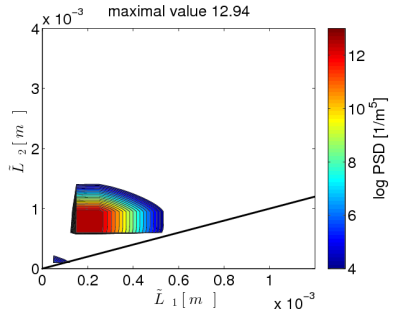

(c) $D = (17.5, 4/12, 1/2)$ cm^3; $\tilde{t}_{\max} = 23$ s

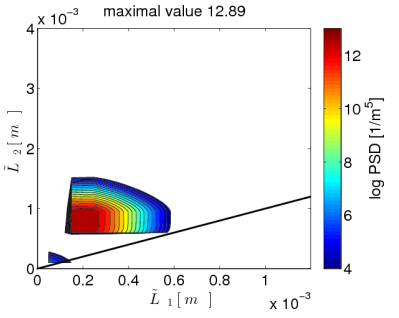

(d) $C = (17.5, 3/12, 1/2)$ cm^3; $\tilde{t}_{\max} = 26$ s

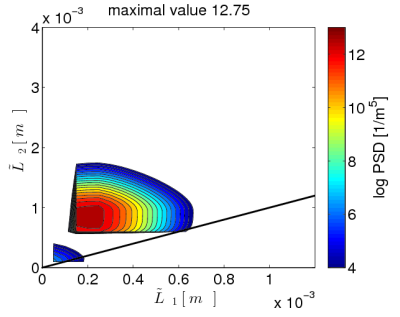

(e) $B = (17.5, 2/12, 1/2)$ cm^3; $\tilde{t}_{\max} = 34$ s

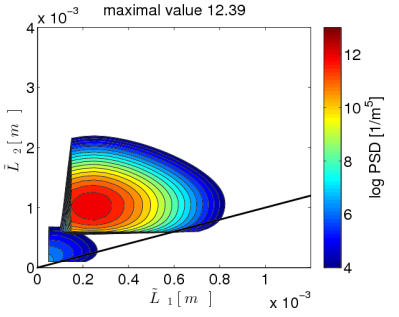

(f) $A = (17.5, 1/12, 1/2)$ cm^3; $\tilde{t}_{\max} = 56$ s

Figure 4.13: (Logarithm of the) PSD at $(17.5, \tilde{x}_2, \tilde{x}_3)$ cm^3; nodes on the line between the wall and the center; FWE–UPW–FDM.

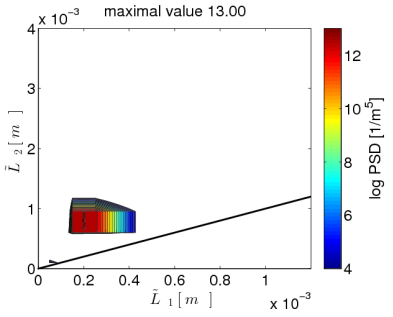

(a) $O = (17.5, 1/2, 1/2)$ cm^3; $\tilde{t}_{\max} = 21$ s

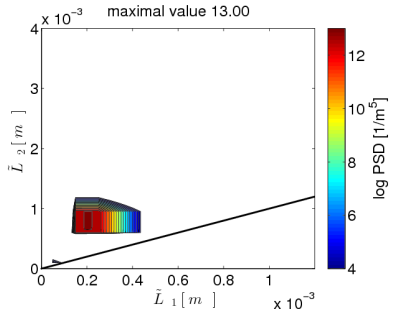

(b) $E = (17.5, 5/12, 1/2)$ cm^3; $\tilde{t}_{\max} = 21$ s

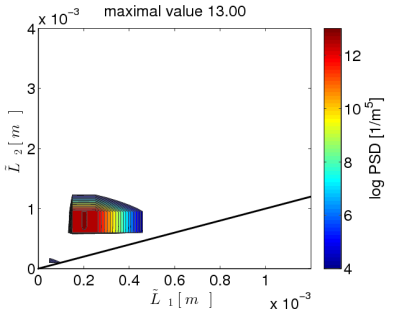

(c) $D = (17.5, 4/12, 1/2)$ cm^3; $\tilde{t}_{\max} = 24$ s

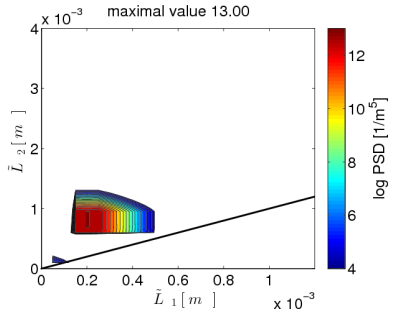

(d) $C = (17.5, 3/12, 1/2)$ cm^3; $\tilde{t}_{\max} = 27$ s

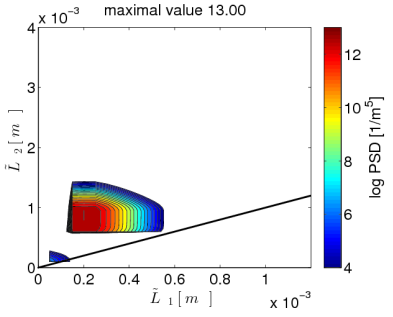

(e) $B = (17.5, 2/12, 1/2)$ cm^3; $\tilde{t}_{\max} = 34$ s

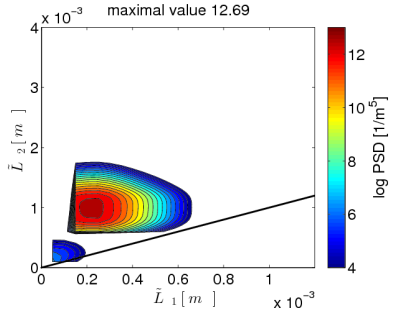

(f) $A = (17.5, 1/12, 1/2)$ cm^3; $\tilde{t}_{\max} = 56$ s

Figure 4.14: (Logarithm of the) PSD at $(17.5, \tilde{x}_2, \tilde{x}_3)$ cm^3; nodes on the line between the wall and the center; RK–ENO–FDM.

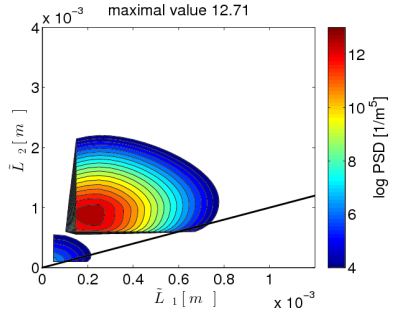

(a) $O = (49, 1/2, 1/2)$ cm^3; $\tilde{t}_{\max} = 59$ s

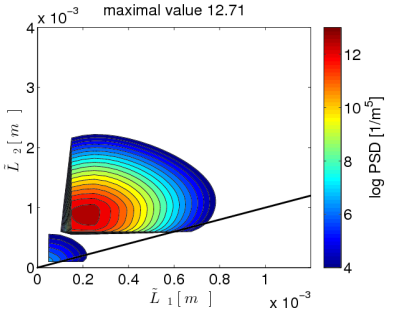

(b) $E = (49, 5/12, 1/2)$ cm^3; $\tilde{t}_{\max} = 60$ s

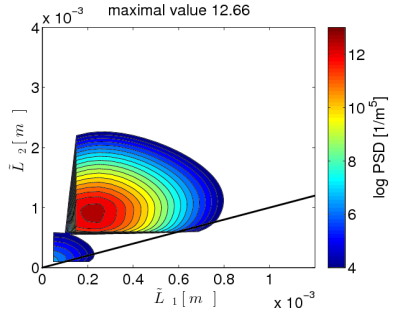

(c) $D = (49, 4/12, 1/2)$ cm^3; $\tilde{t}_{\max} = 65$ s

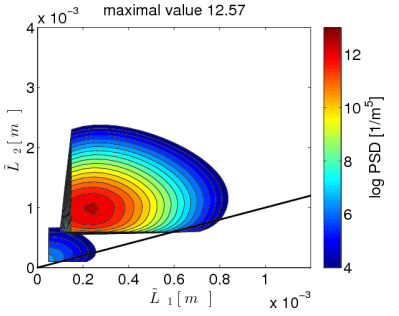

(d) $C = (49, 3/12, 1/2)$ cm^3; $\tilde{t}_{\max} = 74$ s

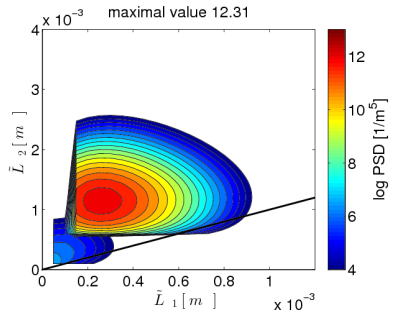

(e) $B = (49, 2/12, 1/2)$ cm^3; $\tilde{t}_{\max} = 96$ s

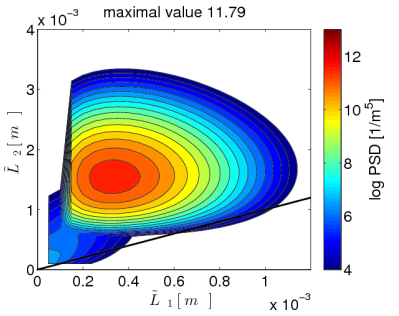

(f) $A = (49, 1/12, 1/2)$ cm^3; $\tilde{t}_{\max} = 167$ s

Figure 4.15: (Logarithm of the) PSD at $(49, \tilde{x}_2, \tilde{x}_3)$ cm^3; nodes on the line between the wall and the center; FWE–UPW–FDM.

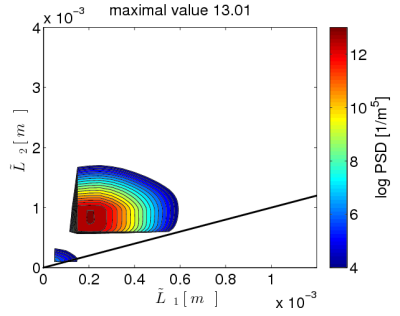

(a) $O = (49, 1/2, 1/2)$ cm^3; $\tilde{t}_{\max} = 59$ s

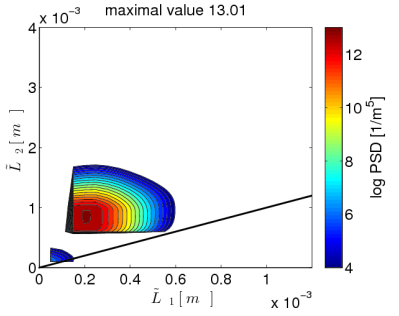

(b) $E = (49, 5/12, 1/2)$ cm^3; $\tilde{t}_{\max} = 60$ s

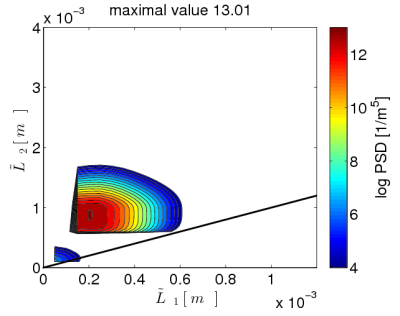

(c) $D = (49, 4/12, 1/2)$ cm^3; $\tilde{t}_{\max} = 65$ s

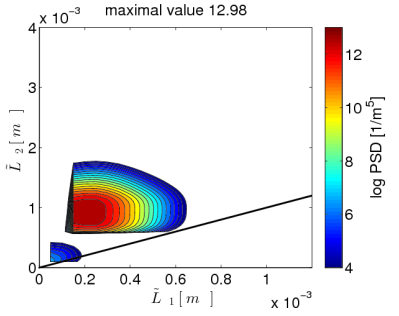

(d) $C = (49, 3/12, 1/2)$ cm^3; $\tilde{t}_{\max} = 74$ s

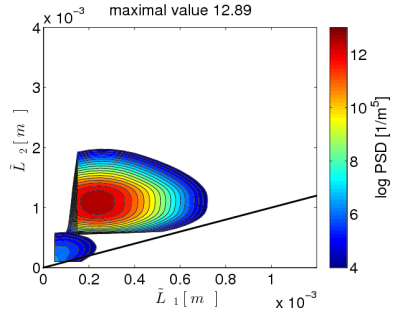

(e) $B = (49, 2/12, 1/2)$ cm^3; $\tilde{t}_{\max} = 96$ s

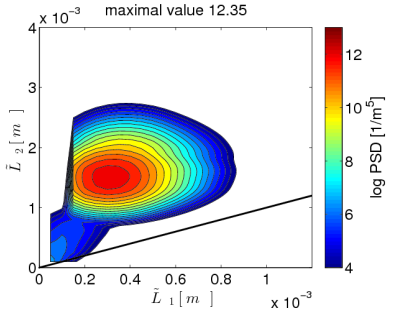

(f) $A = (49, 1/12, 1/2)$ cm^3; $\tilde{t}_{\max} = 167$ s

Figure 4.16: (Logarithm of the) PSD at $(49, \tilde{x}_2, \tilde{x}_3)$ cm^3; nodes on the line between the wall and the center; RK–ENO–FDM.

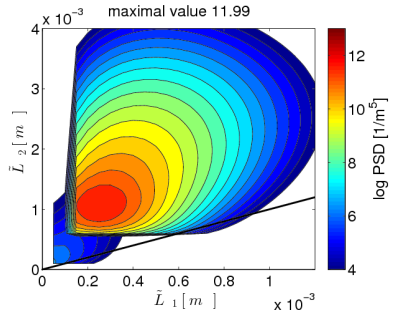

(a) $O = (200, 1/2, 1/2)$ cm^3; $\tilde{t}_{\max} = 240$ s

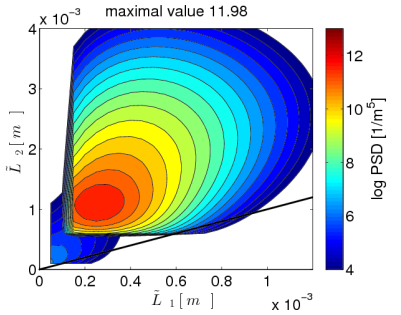

(b) $E = (200, 5/12, 1/2)$ cm^3; $\tilde{t}_{\max} = 245$ s

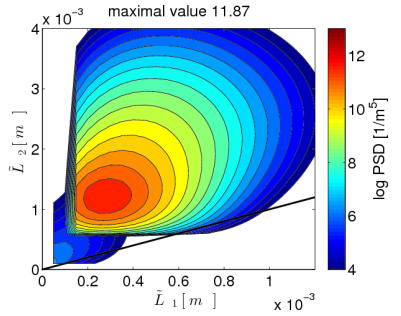

(c) $D = (200, 4/12, 1/2)$ cm^3; $\tilde{t}_{\max} = 264$ s

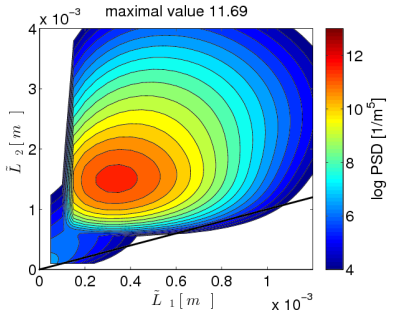

(d) $C = (200, 3/12, 1/2)$ cm^3; $\tilde{t}_{\max} = 300$ s

Figure 4.17: (Logarithm of the) PSD at $(200, \tilde{x}_2, \tilde{x}_3)$ cm^3; nodes on the line between the wall and the center; FWE–UPW–FDM. Note that at $A' = (200, 1/12, 1/2)$ cm^3 and $B' = (200, 2/12, 1/2)$ cm^3 there was no notable amount of particles predicted.

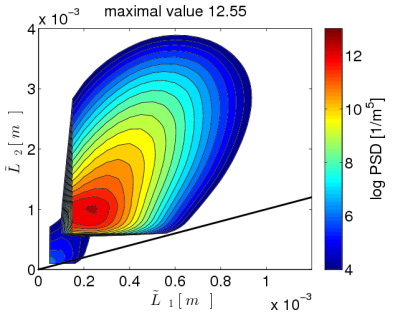

(a) $O = (200, 1/2, 1/2)$ cm^3; $\tilde{t}_{\max} = 240$ s

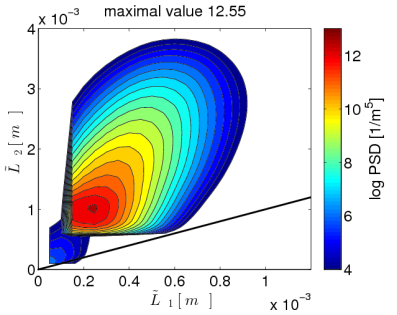

(b) $E = (200, 5/12, 1/2)$ cm^3; $\tilde{t}_{\max} = 245$ s

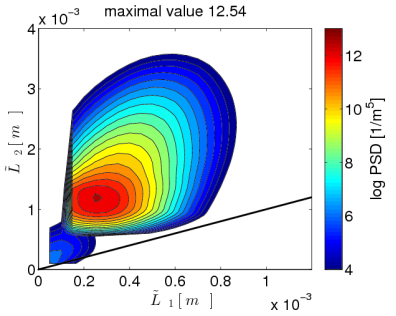

(c) $D = (200, 4/12, 1/2)$ cm^3; $\tilde{t}_{\max} = 264$ s

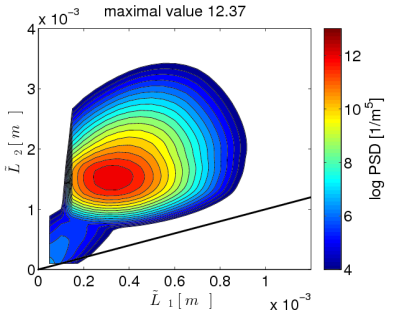

(d) $C = (200, 3/12, 1/2)$ cm^3; $\tilde{t}_{\max} = 300$ s

Figure 4.18: (Logarithm of the) PSD at $(200, \tilde{x}_2, \tilde{x}_3)$ cm^3; nodes on the line between the wall and the center; RK–ENO–FDM. Note that at $A' = (200, 1/12, 1/2)$ cm^3 and $B' = (200, 2/12, 1/2)$ cm^3 there was no notable amount of particles predicted.

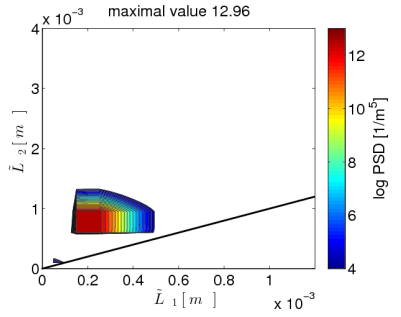

(a) $O = (17.5, 1/2, 1/2)$ cm^3; $\tilde{t}_{\max} = 21$ s

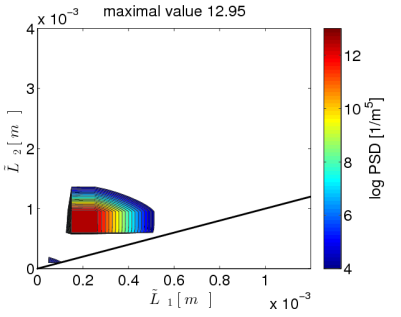

(b) $E' = (17.5, 5/12, 5/12)$ cm^3; $\tilde{t}_{\max} = 22$ s

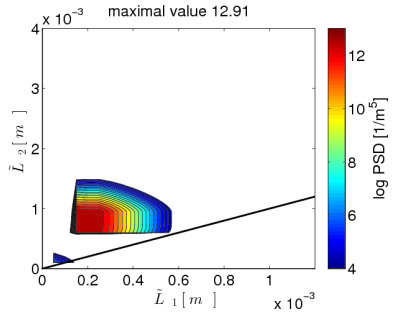

(c) $D' = (17.5, 4/12, 4/12)$ cm^3; $\tilde{t}_{\max} = 26$ s

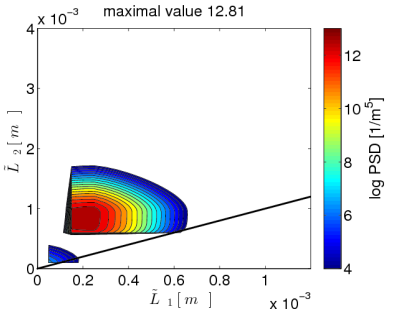

(d) $C' = (17.5, 3/12, 3/12)$ cm^3; $\tilde{t}_{\max} = 33$ s

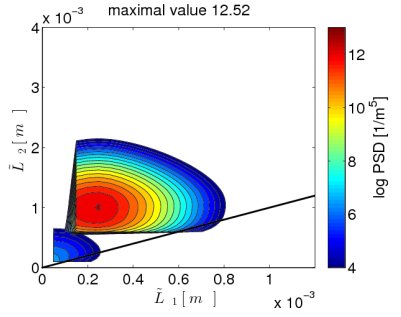

(e) $B' = (17.5, 2/12, 2/12)$ cm^3; $\tilde{t}_{\max} = 52$ s

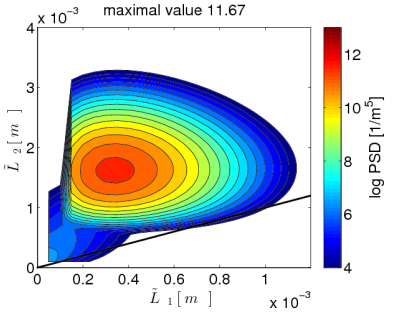

(f) $A' = (17.5, 1/12, 1/12)$ cm^3; $\tilde{t}_{\max} = 137$ s

Figure 4.19: (Logarithm of the) PSD at $(17.5, \tilde{x}_2, \tilde{x}_3)$ cm^3; nodes on the line between the corner and the center; FWE–UPW–FDM.

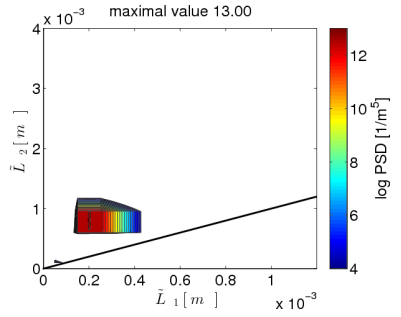

(a) $O = (17.5, 1/2, 1/2)$ cm^3; $\tilde{t}_{\max} = 21$ s

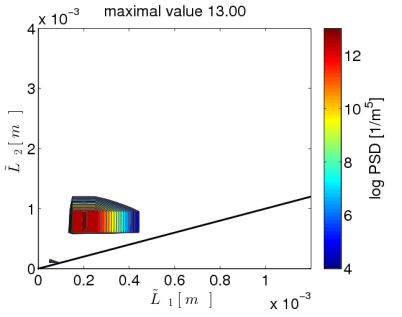

(b) $E' = (17.5, 5/12, 5/12)$ cm^3; $\tilde{t}_{\max} = 22$ s

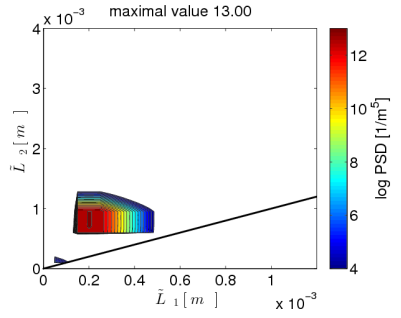

(c) $D' = (17.5, 4/12, 4/12)$ cm^3; $\tilde{t}_{\max} = 26$ s

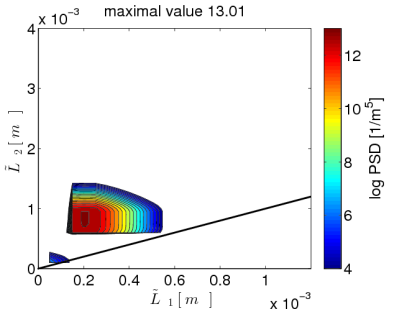

(d) $C' = (17.5, 3/12, 3/12)$ cm^3; $\tilde{t}_{\max} = 33$ s

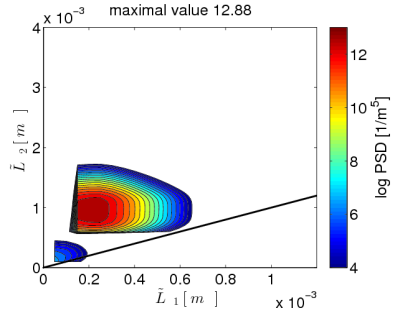

(e) $B' = (17.5, 2/12, 2/12)$ cm^3; $\tilde{t}_{\max} = 52$ s

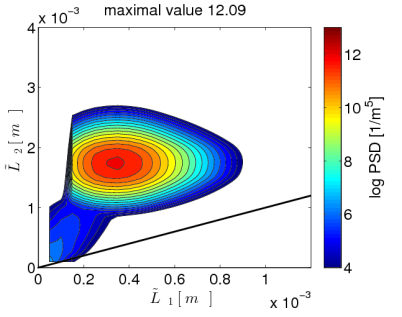

(f) $A' = (17.5, 1/12, 1/12)$ cm^3; $\tilde{t}_{\max} = 137$ s

Figure 4.20: (Logarithm of the) PSD at $(17.5, \tilde{x}_2, \tilde{x}_3)$ cm^3; nodes on the line between the corner and the center; RK–ENO–FDM.

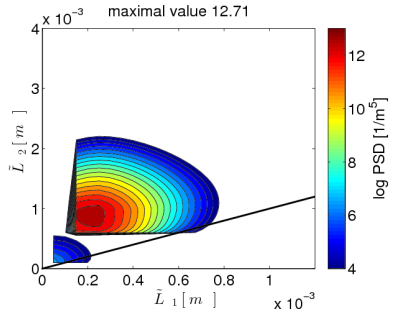

(a) $O = (49, 1/2, 1/2)$ cm^3; $\tilde{t}_{\max} = 59$ s

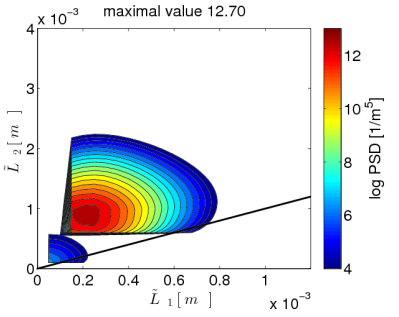

(b) $E' = (49, 5/12, 5/12)$ cm^3; $\tilde{t}_{\max} = 61$ s

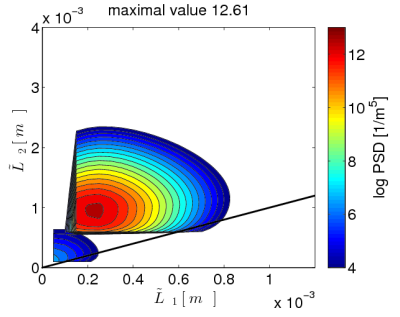

(c) $D' = (49, 4/12, 4/12)$ cm^3; $\tilde{t}_{\max} = 71$ s

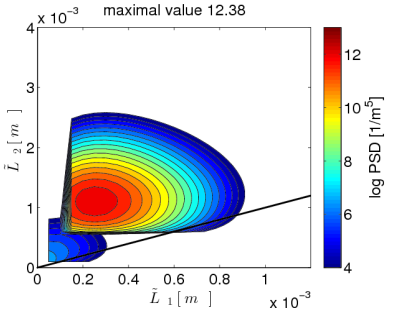

(d) $C' = (49, 3/12, 3/12)$ cm^3; $\tilde{t}_{\max} = 94$ s

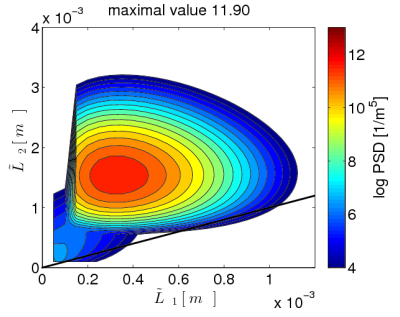

(e) $B' = (49, 2/12, 2/12)$ cm^3; $\tilde{t}_{\max} = 154$ s

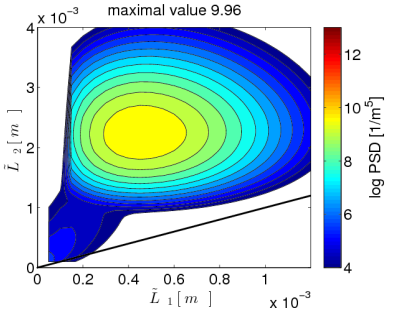

(f) $A' = (49, 1/12, 1/12)$ cm^3; $\tilde{t}_{\max} = 300$ s

Figure 4.21: (Logarithm of the) PSD at $(49, \tilde{x}_2, \tilde{x}_3)$ cm^3; nodes on the line between the corner and the center; FWE–UPW–FDM.

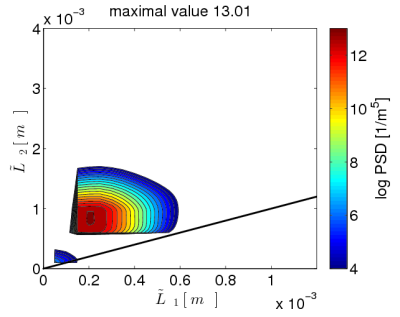

(a) $O = (49, 1/2, 1/2)$ cm^3; $\tilde{t}_{\max} = 59$ s

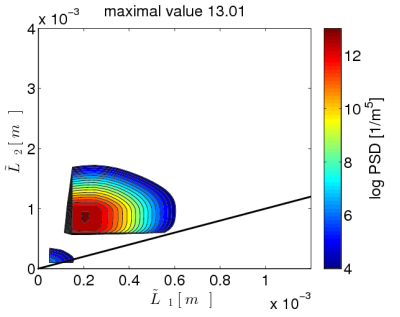

(b) $E' = (49, 5/12, 5/12)$ cm^3; $\tilde{t}_{\max} = 61$ s

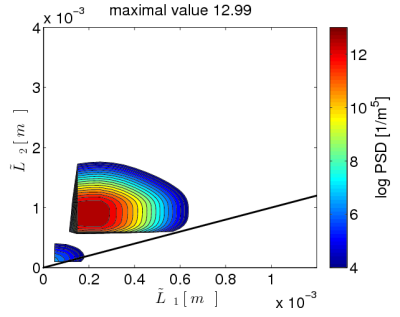

(c) $D' = (49, 4/12, 4/12)$ cm^3; $\tilde{t}_{\max} = 71$ s

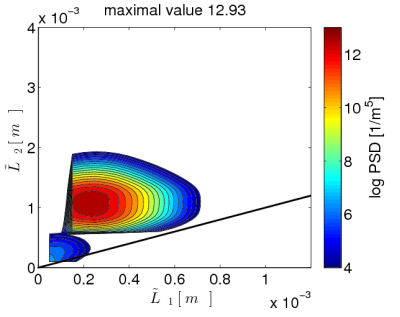

(d) $C' = (49, 3/12, 3/12)$ cm^3; $\tilde{t}_{\max} = 94$ s

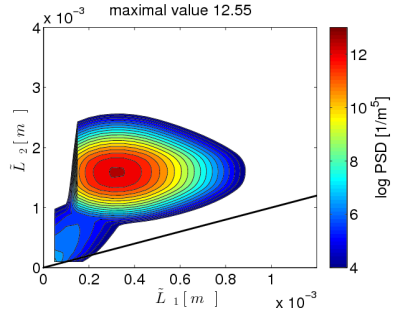

(e) $B' = (49, 2/12, 2/12)$ cm^3; $\tilde{t}_{\max} = 154$ s

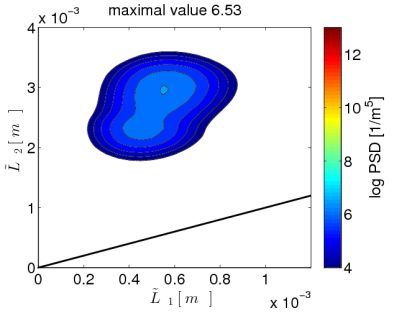

(f) $A' = (49, 1/12, 1/12)$ cm^3; $\tilde{t}_{\max} = 300$ s

Figure 4.22: (Logarithm of the) PSD at $(49, \tilde{x}_2, \tilde{x}_3)$ cm^3; nodes on the line between the corner and the center; RK–ENO–FDM.

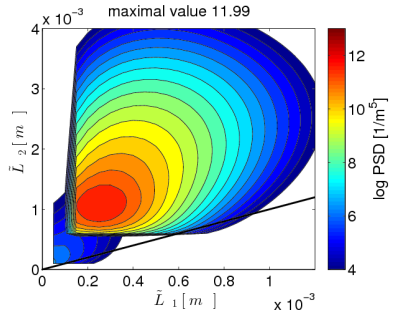

(a) $O = (200, 1/2, 1/2)$ cm^3; $\tilde{t}_{\max} = 240$ s

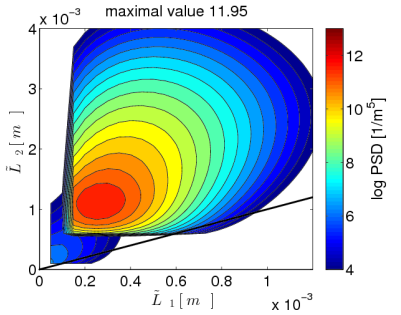

(b) $E' = (200, 5/12, 5/12)$ cm^3; $\tilde{t}_{\max} = 251$ s

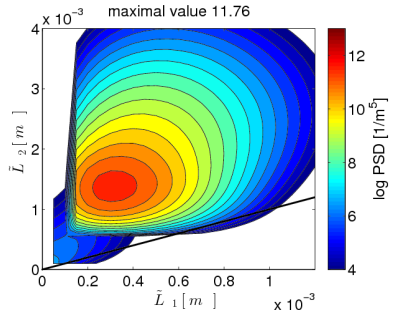

(c) $D' = (200, 4/12, 4/12)$ cm^3; $\tilde{t}_{\max} = 291$ s

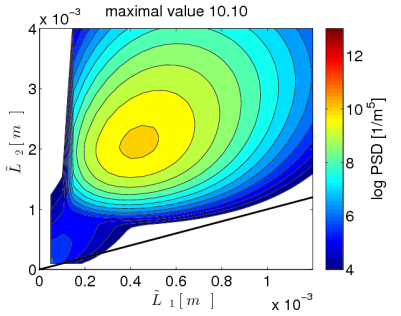

(d) $C' = (200, 3/12, 3/12)$ cm^3; $\tilde{t}_{\max} = 300$ s

Figure 4.23: (Logarithm of the) PSD at $(200, \tilde{x}_2, \tilde{x}_3)$ cm^3; nodes on the line between the corner and the center; FWE–UPW–FDM. Note that at $A' = (200, 1/12, 1/12)$ cm^3 and $B' = (200, 2/12, 2/12)$ cm^3 there was no notable amount of particles predicted.

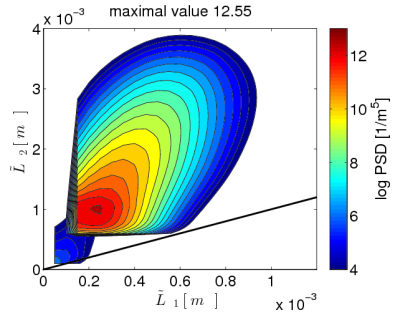

(a) $O = (200, 1/2, 1/2)$ cm^3; $\tilde{t}_{\max} = 240$ s

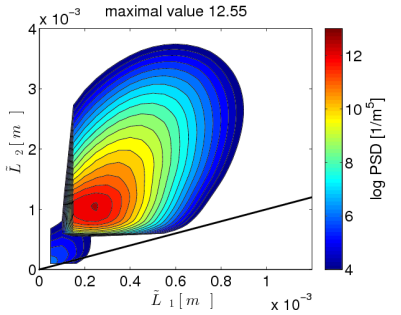

(b) $E' = (200, 5/12, 5/12)$ cm^3; $\tilde{t}_{\max} = 251$ s

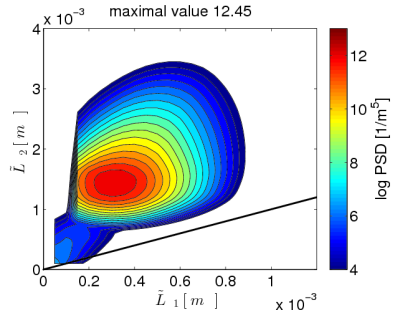

(c) $D' = (200, 4/12, 4/12)$ cm^3; $\tilde{t}_{\max} = 291$ s

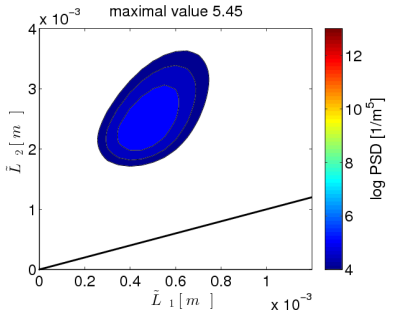

(d) $C' = (200, 3/12, 3/12)$ cm^3; $\tilde{t}_{\max} = 300$ s

Figure 4.24: (Logarithm of the) PSD at $(200, \tilde{x}_2, \tilde{x}_3)$ cm^3; nodes on the line between the corner and the center; RK–ENO–FDM. Note that at $A' = (200, 1/12, 1/12)$ cm^3 and $B' = (200, 2/12, 2/12)$ cm^3 there was no notable amount of particles predicted.

4.3.1 CPU time

The simulations were performed on HP BL2x220c computers with 2933 MHz Xeon processors. Simulating one time step for the first order finite difference scheme took around 29 – 33 seconds, including the calculation of all data for evaluating the numerical simulations. The higher order method had higher computational cost, in our simulations of around a factor of five.

4.3.2 Conclusions

The presented numerical study shows that even in the class of direct discretizations, different numerical methods might lead to qualitatively different numerical solutions. With both methods, the most particles were predicted to occur in the center of the channel and less particles closer to the wall. The bulk of particles followed the flow very well. Also, the spatial separation to the internal coordinates of nucleation from growth phenomena was clearly to distinguish in the numerical results. The method RK–ENO–FDM computed results that were less smeared than the results obtained with using FWE–UPW–FDM. It was shown that predictions, e.g., on the maximal value of the PSD or the length of the time interval with a notable amount of particles at certain points, were qualitatively different. Since RK–ENO–FDM is of the higher order, one can expect to have computed the more accurate results with this method.

5 Summary and outlook

5.1 Summary

This thesis presented a class of numerical methods using direct discretization for simulating population balance systems. Such systems contain equations defined in a three-dimensional domain (Navier–Stokes equations, convection-diffusion equations for mass and energy balances), and an equation for the PSD defined in a higher-dimensional domain, e.g., a four- and five-dimensional domain resulting in uni-variate and bi-variate population balance models. The goal of this thesis consists, on the one hand, in increasing the sensitivity of the population balance community on the possible size of numerical errors and on the other hand, in motivating careful and systematic studies of the properties of numerical methods for solving multivariate particle balance systems in order to obtain guidelines on which method is appropriate for which application.

Firstly, the process of urea synthesis was considered as a uni-variate population balance model. From the experiments, it is known that this process is aggregation-dominated. To our best knowledge, the presented methods are among the few approaches for solving a coupled population balance system with aggregation which is defined in domains with three and four dimensions. Nucleation, growth, aggregation, and transport of the particles were included into the simulations. Two experimental setups were considered. For both, it was possible with the proposed methods to calibrate unknown model parameters in the aggregation kernel in such a way that good agreements to available experimental data were achieved. With the examined methods, the obtained values of the parameters for both experiments were somewhat different but of the same order of magnitude. Several possible reasons for the observed differences were pointed out:

- the idealized assumption of spherical particles in the modeling,
- the observations of projections of particles in the experiments,
- the modeling error of the kernel itself.

Therefore, extensions to multivariate models could achieve more trustful predictive models.

Secondly, the crystallization process of potassium dihydrogen phosphate (KDP) was considered as a bi-variate population balance model. The proposed

methods provide a new contribution to the numerical schemes for solving a coupled population balance systems which are defined in domains with three and five dimensions. In this application, the needle-shaped characterization of the particles was considered. In order to describe needle-shaped particles, two internal coordinates are necessary, e.g., the length and the diameter of the cross-section of the particles. The aggregation was disregarded in this example, since, to date, no aggregation kernels are available in the modeling. Nucleation, growth, and transport of the particles were taken into account. The incorporation of the nucleation was done with a finite volume technique. Since no experimental data were available for this application, the main goal was to demonstrate that even in the class of direct discretizations, by applying different numerical methods, qualitative differences in the solutions might be obtained. In particular, it was shown that, at certain points in the flow domain, the extensive smearing of one of the methods led to wrong predictions of the maximal value of the PSD as well as the time interval where a notable amount of particles are present. However, the higher order finite difference method had higher computational costs.

5.2 Outlook

This thesis presented numerical studies of uni- and bi-variate population balance systems for situations where the PSD is defined in a 4D and 5D tensor-product domain. Therefore, a tensor-product grid could be used and the application of finite difference schemes was straightforward.

- *An extension, which is necessary for applications, consists in modifying the implementation to more complicated physical domains. Then, the application of finite difference approaches to the PSD equation becomes more involved. Since the internal coordinates still span a tensor-product domain, an idea consists in developing hybrid discretizations for this equation which are based on finite element ideas for the external coordinates and finite differences schemes for the internal coordinates.*

- *From the point of view of efficiency, the long computing times, caused by high computational costs of the direct discretizations, can be reduced by parallelizing the algorithms.*

- *An open topic, whose study would be very important for the chemical engineering community, is the comprehensive and competitive study of different approaches for solving population balance systems, in particular of direct discretizations, momentum-based methods, and operator splitting schemes. To our best knowledge, this topic is almost completely open.*

- *For the calibration of model parameters, at is was necessary for the univariate PSD in Sec. 3, an algorithmic improvement would be the use of an optimization algorithm. Since such an algorithm usually requires many numerical solutions pf the problem, new questions arise, like the use of reduced order methods.*

Bibliography

[1] V. Alopaeus, J. Koskinen, and K. I. Keskinen. Simulation of the population balances for liquid-liquid systems in a nonideal stirred tank. part 1:description and qualitative validation of the model. Chem. Engrg. Sci.*, 54:5887–5899, 1999.*

[2] K.A. Berglund. Analysis and Measurement of Crystallization Utilizing the Population Balance. In A. Myerson, editor, Handbook of Industrial Crystallization. *Butterworth-Heinemann, second edition, 2002.*

[3] F. J. Blom. A monolithical fuid-structure interaction algorithm applied to the piston problem. Comp. Meth. Appl. Mech. Eng.*, 167:369 – 391, 1998.*

[4] C. Borchert. Kdp model parameters. personal communication, Otto–von–Guericke–Universität Magdeburg, 2012.

[5] C. Borchert. Topics in Crystal Shape Dynamics. *PhD thesis, Otto–von–Guericke–Universität Magdeburg, 2012.*

[6] C. Borchert and K. Sundmacher. Crystal aggregation in a flow tube: image-based observation. Chem. Eng. Technol.*, 34:545 – 556, 2011.*

[7] R. Bordas, V. John, E. Schmeyer, and D.Thévenin. Measurement and Simulation of a Droplet Population in a Turbulent Flow Field. Computers and Fluids*, 66:52–62, 2012.*

[8] S.C. Brenner and L.R. Scott. The Mathematical Theory of Finite Element Methods, volume 15 of Texts in Applied Mathematics. *Springer–Verlag New York, 1975.*

[9] F. Brezzi and M. Fortin. Mixed and Hybrid Finite Element Methods. *Springer-Verlag, New York, 1991.*

[10] H. Briesen. Modeling of suspension crystallization processes with complex particle characterization. Habilitation thesis, Universität Achen, 2008.

[11] P.G. Ciarlet. The finite element method for elliptic problems. *North–Holland, Amsterdam, New York, Oxford, 1978.*

[12] J. Crank and E. Nicolson. A practical method for numerical evaluation of solution of partial differential equations of heat-conduction type. Proc. Camb. Phil. Soc.*, 43:50–67, 1947.*

[13] M. Crouzeix and P.-A. Raviart. Conforming and nonconforming finite element methods for solving the stationary Stokes equations 1. R.A.I.R.O. Anal. Numér.*, 7:33–76, 1973.*

[14] L.G.M. de Souza, G. Janiga, V. John, and D. Thévenin. Reconstruction of a distribution from a finite number of moments with an adaptive spline-based algorithm. Chem. Engrg. Sci.*, 65:2741 – 2750, 2010.*

[15] C.A. Felippa and K.C. Park. Staggered transient analysis procedures for coupled mechanical systems: formulation. Comp. Meth. Appl. Mech. Eng.*, 24:61 – 111, 1980.*

[16] C.A. Felippa and K.C. Park. Partitioned analysis of coupled systems. In T.J.R. Huges T. Belytschko, editor, Computational Methods in Transient Analysis*. North–Holland, Amsterdam, second edition, 1983.*

[17] J. Ferziger and M. Peric. Computational Methods for Fluid Dynamics*. Springer–Verlag Berlin, 2 edn., 1999.*

[18] S. Ganesan. An operator-splitting heterogeneous finite element method for population balance equations: stability and convergence. Preprint 1531, WIAS, Berlin, 2010.

[19] S. Ganesan and L. Tobiska. An operator-splitting finite element method for efficient parallel solution of multidimensional population balance systems. Chem. Engrg. Sci.*, 69:59–68, 2012.*

[20] S. Ganesan and L. Tobiska. Implementation of an operator-splitting finite element method for high-dimensional parabolic problems. Chem. Engrg. Sci.*, 219:6182–6196, 2013.*

[21] A. Gerstlauer. Herleitung und Reduktion populationsdynamischer Modelle am Beispiel der Flüssig-Flüssig-Extraktion*, volume 3 of* Verfahrenstechnik*. VDI Verlag, Düsseldorf, 1999.*

[22] V. Girault and P.-A. Raviart. Finite Elemente Methods for Navier–Stokes equations*. Springer-Verlag, Berlin and New–York, 1986.*

[23] H. Goertler. Dimensionsanalyse*. Springer–Verlag, 1975.*

[24] J. Gradl, H.-C. Schwarzer, F. Schwertfirm, M. Manhart, H.-J. Schmid, and W. Peukert. Precipitation of nanoparticles in a T–mixer: Coupling the particle population dynamics with hydrodynamics through direct numerical simulation. Chem. Engrg. Proc.*, 45:908 – 916, 2006.*

[25] P.M. Gresho and R.L. Sani. Incompressible Flow and the Finite Element Method. *Wiley, Chichester, 2000.*

[26] R. Gunawan, I. Fusman, and R. D. Braatz. High resolution algorithms for multidimensional population balance equations. AIChE J*, 50:2738–2749, 2004.*

[27] R. Gunawan, D.L. Ma, M. Fujiwara, and R. D. Braatz. Identification of Kinetic Parameters in a Multidimensional Crystallization Process. Int. J. Mod. Phys. B*, 16:367–374, 2002.*

[28] W. Hackbusch. On the efficient evaluation of coalescence integrals in population balance models. Numer. Math.*, 78:145 – 159, 2006.*

[29] W. Hackbusch. Approximation of coalescence integrals in population balance models with local mass conservation. Numer. Math.*, 106:627 – 657, 2007.*

[30] W. Hackbusch. Convolution of hp-functions on locally refined grids. IMA Journal of Numerical Analysis*, 29:960 – 985, 2009.*

[31] W. Hackbusch, V. John, A. Kachatryan, and C. Suciu. A Numerical Method for the Simulation of Aggregation-Driven Population Balance System. Int. J. Numer. Meth. Fluids*, 69:1646 – 1660, 2012.*

[32] C. Hirsch. Numerical Computation of Internal and External Flows*, volume 1 of* Fundamentals of Computational Fluid Dynamics*. John Wiley and Sons, Chichester, 1988.*

[33] H. Hulburt and S. Katz. Some problems in particle technology: A statistical mechanical formulation. Chem. Engrg. Sci.*, 19:555 – 574, 1964.*

[34] V. John. Higher order finite element methods and multigrid solvers in a benchmark problem for the 3D Navier–Stokes equations. Int. J. Num. Meth. Fluids*, 40:775 – 798, 2002.*

[35] V. John. On the Efficiency of Linearization Schemes and Coupled Multigrid Methods in the Simulation of a 3d Flow Around a Cylinder. Int. J. Num. Meth. Fluids*, 50:845 – 862, 2006.*

[36] V. John, I. Angelov, A. Öncül, and D. Thévenin. Techniques for the Reconstruction of a Distribution from a Finite Number of its Moments. Chem. Engrg. Sci.*, 62:2890 – 2904, 2007.*

[37] V. John and G. Matthies. Higher Order Finite Element Discretizations in a Benchmark Problem for Incompressible Flows. Int. J. Num. Meth. Fluids*, 37:885 – 903, 2001.*

[38] V. John and G. Matthies. MooNMD - a program package based on mapped finite element methods. Comput. Visual. Sci.*, 6:163 – 170, 2004.*

[39] V. John and J. Novo. On (Essentially) Non-Oscillatory Discretization of Evolutionary Convection-Diffusion Equations. J. Comput. Phys.*, 231:1570–1586, 2012.*

[40] V. John and M. Roland. Simulation of 3D/4D Precipitation Process in a Turbulent Flow Field*. in Numerical Mathematics and Advanced Applications 2009, G. Kreiss et al. (eds.) Springer, 479 – 487, 2010.*

[41] V. John and E. Schmeyer. Finite element methods for time-dependent convection-diffusion-reaction equations with small diffusion. Comput. Methods Appl. Mech. Engrg.*, 198:475 – 494, 2008.*

[42] V. John and E. Schmeyer. On finite element methods for 3D time-dependent convection-diffusion-reaction equations with small diffusion. In BAIL 2008 – Boundary and Interior Layers*, volume 69 of* Lecture Notes in Computational Science and Engineering*, pages 173 – 182. Springer, 2009.*

[43] A. Kachatryan. Library for computing the aggregation integrals. personal communication, MPI Leipzig, 2011.

[44] V. Kulikov, H. Briesen, R. Grosch, L. von Wedel, A. Yang, and W. Marquardt. Modular dynamic simulation for integrated particulate processes by means of tool integration. Chem. Engrg. Sci.*, 60:2069 – 2083, 2005.*

[45] V. Kulikov, H. Briesen, and W. Marquardt. A framework for the simulation of mass crystallization considering the effect of fluid dynamics. Chem. Engrg. Proc.*, 60:886 – 899, 2007.*

[46] D. Kuzmin. Explicit and implicit FEM–FCT algorithms with flux linearization. J. Comput. Phys.*, 228:2517 – 2534, 2009.*

[47] D. Kuzmin and M. Moeller. Algebraic flux correction I. Scalar conservation laws In R. Loehner, D. Kuzmin und S. Turek (Hg.), Flux–Corrected Transport: Principles, Algorithms and Applications*. Springer–Verlag, 2005.*

[48] D. Kuzmin, M. Moeller, and S. Turek. High-resolution FEM–FCT schemes for multidimensional conservation laws. Comput. Methods Appl. Mech. Engrg.*, 193:4915–4946, 2004.*

[49] D. Kuzmin and S. Turek. Flux correction tools for finite elements. J. Comput. Phys.*, 175:525 – 558, 2002.*

[50] L.D. Landau and E.M. Lifschitz. Fluid mechanics, vol. 6 Course of Theoretical physic. *Pergamon Press, 1987.*

[51] R. LeVeque. Numerical methods for conservation laws. *ETH Zürich, 1992.*

[52] C. Lindenberg, J. Schöll, M. Vicum, and J. Brozio. L–glutamic acid precipitation: Agglomeration effects. Crystal Growth and Design, *8:224 – 234, 2008.*

[53] D.L. Ma and R.D. Braaz. Worst-Case Analysis of Finite-Time Control Policies. IEEE Trans. on Control Syst. Tech, *9:766–774, 2001.*

[54] D.L. Ma, D.K. Tafti, and R.D. Braaz. High–resolution simulation of multidimensional crystal growth. Industrial and Engineering Chemistry Research, *41:6217–6223, 2002.*

[55] D.L. Ma, D.K. Tafti, and R.D. Braaz. Optimal control and simulation of multidimensional crystallization processes. Computers and Chemical Engineering, *26:1103–1116, 2002.*

[56] A. Majumder, V. Kariwala, S. Ansumali, and A. Rajendran. Lattice boltzmann method for multi-dimensional population balance models in crystallization. Chem. Engrg. Sci., *70:121–134, 2012.*

[57] D.L. Marchisio and R.O. Fox. Solution of population balance equations using the direct quadrature method of moments. Journal of Aerosol Science, *36(1):43–73, 2005.*

[58] R. McGraw. Description of Aerosol Dynamics by the Quadrature Method of Moments. Aerosol Science and Technology, *27:255 – 265, 1997.*

[59] A. Mersmann. Crystallization Technology Handbook. *Dekker New York, 2001.*

[60] J.W. Mullin. Crystallisation. *Butterworth-Heinemann, 4 edn., 2001.*

[61] D. Potts. Schnelle Fourier–Transformationen für nichtächidistanten Daten und Andwendungen. *PhD thesis, Universität zu Lübeck, 2003.*

[62] D. Ramkrishna. The status of population balances. Chem. Engrg. Sci., *3:49–95, 1985.*

[63] D. Ramkrishna. Population balances. *Academic Press, 2000.*

[64] A. Randolph and M. Larson. Theory of particulate processes: Analysis and Techniques of Continuous Crystallization. *Academic Press, Inc., 1988.*

[65] A. Randolph and E. White. Modeling size dispersion in the prediction of crystal-size distribution. Chem. Engrg. Sci.*, 32:1067–1076, 1977.*

[66] R. Rannacher and S. Turek. Simple nonconforming quadrilateral stokes element. Numer. Meth. Diff. Part. Equ.*, 8:97–111, 1992.*

[67] M. Roland. Numerische Simulation von Fällungsprozessen mittels Populationsbilanzen*. PhD thesis, Universität des Saarlandes, 2010.*

[68] H. Roos, M. Stynes, and L. Tobiska. Robust Numerical Methods for Singularly Perturbed Differential Equations*. Springer–Verlag, 2008.*

[69] S. Rugonyi and K.-J. Bathe. On the analysis of fully-coupled fluid flows with structural interaction – a coupling and condensation procedure. In. J. of Comp. Civil and Struct. Eng*, 1:29 – 41, 2000.*

[70] Y. Saad. A flexible inner-outer preconditioned GMRES algorithm. SIAM Journal on Scientific Computing*, 14:461–469, 1993.*

[71] H.-C. Schwarzer, F. Schwertfirm, M. Manhart, H.-J. Schmid, and W. Peukert. Predictive simulation of nanoparticle precipitation based on the population balance equation. Chem. Engrg. Sci.*, 61:167 – 181, 2006.*

[72] C.W. Shu. High order weighted essentially non-oscillatory schemes for convection dominated problems. SIAM Rev.*, 51:82–126, 2009.*

[73] C.W. Shu and S. Osher. Efficient implementation of essentially non-oscillatory shock capturing schemes. J. Comput. Phys.*, 77:439–471, 1988.*

[74] M. Smoluchowski. Versuch einer mathematischen Theorie der Koagulationskinetik kolloider Lösungen. Z. Phys. Chem*, 92:29 – 168, 1917.*

[75] T. Togkalidou, M. Fujiwara, S. Patel, and R. D. Braatz. Solute Concentration Prediction Using Chemometrics and ATR–FTIR Spectroscopy. J. Cryst. Growth*, 231:534–543, 2001.*

[76] F.M. White. Fluid Mechanics*. McGraw-Hill, 4 edn., 2002.*

[77] S. Zalesak. Fully multi-dimensional flux corrected transport algorithms for fluid flow. J. Comput. Phys.*, 31:335 – 362, 1979.*

[78] O.C. Zienkiewicz. Coupled problems and their numerical solution. In: R.W. Lewis, P. Bettes, E. Hinton (eds.) Numerical Methods in Coupled Systems*. Wiley, Chichester, 35 – 58, 1984.*

[79] O.C. Zienkiewicz and A.H.C. Chan. Coupled problems and their numerical solution. In: I. S. Doltsinis (ed.) Advances in Computational Non-linear Mechanics*. Springer, Berlin, 109 – 176, 1988.*

Subject index

Symbol index

Eidesstattliche Erklärung.

Ich erkläre hiermit an Eides statt, dass ich die vorliegende Dissertation selbstständig verfasst habe und alle benutzten Hilfsmittel und Quellen vollständig angegeben habe. Die Zusammenarbeit mit anderen Wissenschaftlern habe ich kenntlich gemacht. Diese Personen haben alle bereits ihr Promotionsverfahren abgeschlossen. Eine Anmeldung der Promotionsabsicht habe ich an keiner anderen Fakultät oder Hochschule beantragt.

Berlin, 8 Mai 2012

Oana Carina Suciu